DYNAMIC INITIATION AND PROPAGATION OF CRACKS IN UNIDIRECTIONAL COMPOSITE PLATES

Thesis by

Demirkan Coker

In Partial Fulfillment of the Requirements

for the Degree of

Doctor of Philosophy

Graduate Aeronautical Laboratories

California Institute of Technology

Pasadena, California

2001

(Defended May 23, 2001)

This thesis is dedicated to

my parents, Ferhunde and Huseyin Nazim,

my sisters, Berna and Esra,

and my brother, Ahmet Ali.

ACKNOWLEDGMENTS

During my very enjoyable stay at Caltech, I have always felt lucky and privileged to have the opportunity to work in this very stimulating research environment and to have met people who make Caltech such a unique place. The acknowledgments section is usually the only place where one can clearly state his appreciation for the people he has worked and interacted with and who have irreversibly shaped his way of thinking. I looked forward to writing this section for a long time. However, consistent with my overall behavior, it is the last part that I wrote, just one scant hour before turning in the final copy of my thesis.

First and foremost, I would like to sincerely thank my advisor, Professor Ares J. Rosakis for his support, guidance and positive reinforcement during my Ph.D. studies. I am very grateful to him for directing me in this most fruitful study, and giving me the space to pursue the topics and ideas in my thesis at my pace. His enthusiasm was very contagious, and during the course of most of my research I caught this excitement and the drive to study dynamic fracture mechanics, mostly at the expense of marginalizing other aspects of my life. ***Indeed***, the most important component of scientific research is this feeling of excitement, which I was lucky to have experienced. Other professors that I looked up to and that also contributed to my enjoyment and appreciation of research were Professors Wolfgang G. Knauss, Michael Ortiz, Guruswami Ravichandran with their distinct personal approaches to research that are drastically different from each other. I would like to specifically thank Professor Ravichandran for sharing his wisdom and experience in our long conversations, and also his guidance and advice beyond the lab. I will fondly remember our running sessions up Henninger flats and adventurous hikes in

state parks. I would also like to thank Professors Hiroo Kanamori and Tom Heaton for introducing me to the subject of earthquakes and for serving in my defense committee.

Special thanks to Petros Arakelian who was always there for me when I needed technical help. I would also like to thank Joe Haggarty, Ali Kiani, Larry Frazier and Bradley St. John for their help in the machine shop and helping me meet deadlines on a short notice.

I am grateful to all my fellow graduate students who made all these years of my stay at Caltech very stimulating, pleasant and enjoyable. I would like to mention first Dr. Pradeep Guduru and Dr. Omprakash Samudrala who were my comrades from the beginning to the end doing research in the area of dynamic fracture mechanics. I would like to acknowledge my officemates and friends (at one time or another since I was the only stationary object in the office): Dr. Ying Huang, Dr. Sangwook Lee, Dr. Sandeep Sane, Dr. Luoyu Roy Xu, Javier Gonzales and Bibhuti Patel, and my post-doc friends: Dr. Hansuk Lee, Dr. Raman Singh and Dr. Sairam Sundaram. I would like to thank Rusi for scanning and formatting a bulk of my experimental pictures which was a tremendous help to me. I am indebted to Professor John Lambros, who is an excellent teacher, for introducing me to dynamic fracture experimentation.

I would like to thank Dr. David M. Owen for all his help in my experiments, his help in using the SEM, sharing of his wisdom, mostly accurate and occasionally useful advice. I would like to especially thank him and Ms. Denise Thobe for their positive support in the last one month of the writing of my dissertation which was a major psychological boost for me. I am proud to consider Ms. Denise Thobe a close friend, and would like to thank her for all her help in making

life easier for me. I would like to thank my friend David Anderson for his help in many aspects of my research, especially Matlab programming and comic relief. Finally, I would like to express my appreciation to my friends and present and former roommates Marco Casari and Dr. Claudine Chen for their help and support.

I was very fortunate to have met Tina Pavlin who has made all aspects of life more joyful and meaningful. She is one person that I can share my passion for sciences and arts with. I would like to thank her for her generous support and staying up several nights reviewing, correcting and editing my thesis. Finally, I would like to thank my family for their unconditional support and sacrifices they consistently made on my behalf. My parents have taught me the importance of truth and the sanctity of work. My sisters and brother made many sacrifices so I could continue on my path. To my family I dedicate this thesis.

Financial support for this work was provided by the Office of Naval Research (Dr. Y.D.S. Rajapakse, Scientific Officer)

ABSTRACT

Dynamic crack growth along weak planes is a significant mode of failure in composites and other layered/sandwiched structures and is also the principal mechanism of shallow crustal earthquakes. In order to shed light on this phenomenon dynamic crack initiation and propagation characteristics of a model fiber-reinforced unidirectional graphite/epoxy composite plate was investigated experimentally. Dynamic fracture experiments were conducted by subjecting the composite plates to in-plane, symmetric and asymmetric, impact loading. The lateral shearing interferometric technique of coherent gradient sensing (CGS) in conjunction with high-speed photography was used to visualize the failure process in real time. It was found that mode-I cracks propagated subsonically with crack speeds increasing to the neighborhood of the Rayleigh wave speed of the composite. Also in mode-I, the dependence of the dynamic initiation fracture toughness on the loading rate was determined and was found to be constant for low loading rates and to increase rapidly above $\dot{K}_I^d > 10^5$. The dynamic crack propagation toughness, K_{ID}, was observed to decrease with crack tip speed up to the Rayleigh wave speed of the composite.

For asymmetric, mode-II, types of loading the results revealed highly unstable and intersonic shear-dominated crack growth along the fibers. These cracks propagated with unprecedented speeds reaching 7400 m/s which is the dilatational wave speed of the composite along the fibers. For intersonic crack growth, the interferograms featured a shock wave structure typical of disturbances traveling with speeds higher than one of the characteristic wave speeds in the solid. In addition high speed thermographic measurements are conducted that show concentrated hot spots behind the crack tip indicating non-uniform crack face frictional contact.

In addition, shear dominated dynamic crack growth is investigated along composite/Homalite interfaces subjected to impact loading. The crack growth phenomenon was observed using dynamic photoelasticity in conjunction with high-speed photography. Three quantized intersonic and supersonic crack tip speed regimes were identified. First conclusive evidence of crack growth at supersonic speeds with respect to lower speed material and sonic speeds with respect to the unidirectional composite was obtained. Furthermore, this investigation documents the first experimental observation of a mother/daughter crack mechanism allowing a subsonic crack to evolve into an intersonic crack.

TABLE OF CONTENTS

INTRODUCTORY REMARKS

This doctoral dissertation consists of three independent chapters, each with its own abstract, introduction and conclusions. The overall theme of the work is the dynamic fracture of unidirectional composite materials with cracks growing along the fibers. The composite material is viewed as an ideal model material to investigate fracture behavior of materials under dynamic loading conditions and mixed mode conditions. It presents a unified approach to the mode-I and mode-II fracture in materials by allowing us to propagate a crack in either of these modes in the same material without inducing artificially weak planes for mode-II crack growth. We show that the composite material can be treated as a *homogeneous*, orthotropic material with a line of prescribed crack path (heterogeneous fracture toughness) see figure 1. This preferable crack path traps the crack and suppresses branching or kinking by preventing the creation of distributed

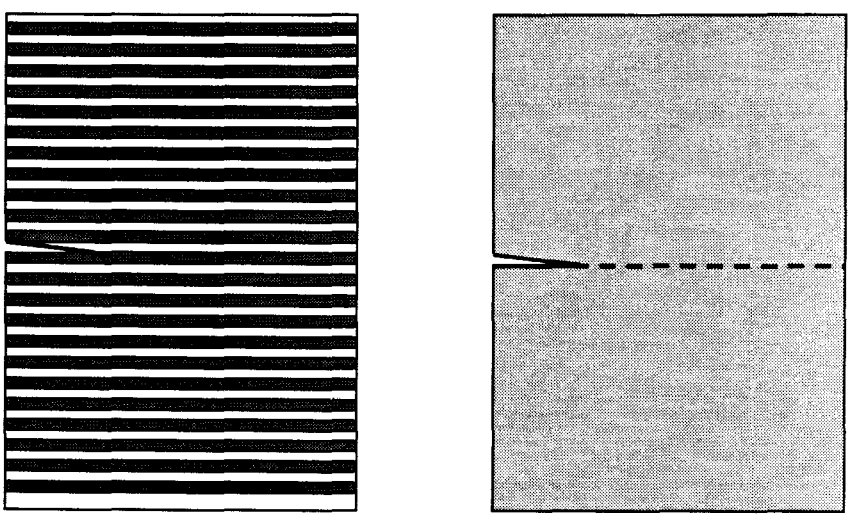

Figure 1 (a) Composite material with fiber and matrix constituents, (b) orthotropic material with homogenized properties and prescribed crack path.

damage. Thus, the results of these experiments are applicable to failures in a wide class of modern engineering components involving heterogeneous bonded solids such as failure along interfaces or welds in structures. It is also conceptually applicable to the modeling of earthquake source dynamics where the source process is modeled as a shear rupture trapped to propagate along a preexisting, often layered, weak fault plane.

In Chapter 1 we examine the crack tip speed regimes for mode-I and mode-II cracks subjected to impact loading. The specimens were 48 ply thick unidirectional graphite/epoxy composite plates which were either loaded symmetrically (mode-I) or asymmetrically (mode-II) by impact in a one-point bend configuration with an edge pre-notch machined in the fiber direction. Moderate impact speeds of up to 57 m/s were used. The lateral shearing interferometric technique of coherent gradient sensing (CGS) in conjunction with high-speed photography was used to visualize the failure process in real time. Mode-I cracks propagated subsonically with crack speeds increasing to the neighborhood of the Rayleigh wave speed. For asymmetric, mode-II, types of loading the results revealed highly unstable and intersonic shear-dominated crack growth along the fibers. These cracks propagated with unprecedented speeds reaching 7400 m/s, a speed which is more than three times the shear wave speed of the composite and almost equal to the dilatational wave speed of the composite along the fibers. For intersonic crack growth, the interferograms featured a shock wave structure typical of disturbances travelling with speeds higher than one of the characteristic wave speeds in the solid. In addition high speed thermographic measurements are conducted that show concentrated hot spots behind the crack tip indicating non-uniform crack face frictional contact.

In chapter 2, subsonic mode-I dynamic crack initiation and propagation in fiber-reinforced unidirectional graphite/epoxy composite plates are analyzed. Single-edge notched specimens were dynamically loaded in mode-I by impacting them with a steel projectile opposite the machined notch at moderate impact speeds of up to 57 m/s. The crack tip location and the dynamic stress intensity factor were obtained from full-field measurements in real-time using a high-speed camera in conjunction with coherent gradient sensing (CGS) optical interferometry. The dependence of the dynamic initiation fracture toughness on the local, near tip, loading rate was determined and was found to be constant for low loading rates and to increase rapidly above $\dot{K}_I^d > 10^5$, consistent with observed trends in homogeneous isotropic materials. Subsequently, cracks propagated along the fibers either in the matrix or the fiber/matrix interface, and accelerated to various steady state speeds which were always less than the Rayleigh wave speed of the composite depending on the initial loading. The dynamic crack propagation toughness, K_{ID}, was measured as a function of crack tip speed and was observed to decrease with crack tip speed up to the Rayleigh wave speed of the composite.

In chapter 3, dynamic crack growth is investigated along composite/Homalite interfaces subjected to impact loading. The unidirectional composite is oriented so that the direction of growth of the fastest dilatational waves is parallel to the bond line. This is intentionally done to maximize crack speeds in the bimaterial system and to explore the extreme possibility of supersonic crack growth along the bond. The specimens are loaded in different configurations by impacting them with a projectile. This dynamic loading causes the cracks to initiate and subsequently grow along the interface at very high speeds. The crack growth phenomenon was observed using dynamic photoelasticity in conjunction with high-speed photography. Varying

the impact configuration resulted in different crack propagation speed regimes. On the basis of crack tip speeds three crack growth regimes are identified: crack growth at the dilatational wave speed of the composite, at the dilatational wave speed of the Homalite and at $\sqrt{2}$ times the shear wave speed of the Homalite. First conclusive evidence of crack growth at supersonic speeds with respect to lower speed material and sonic speeds with respect to the unidirectional composite was obtained. In addition, this investigation documents the first experimental observation of a mother/daughter crack mechanism allowing a subsonic crack to evolve into an intersonic crack.

Chapter 1

Experimental Observations of Intersonic Crack Growth in Asymmetrically Loaded Unidirectional Composite Plates

ABSTRACT

Some recent experimental observations of highly dynamic crack growth events in thick unidirectional composites are presented. The specimens used in this study were 48-ply thick unidirectional graphite/epoxy composite plates which were either symmetrically (mode-I) or asymmetrically (mode-II) loaded by impact in a one-point bend configuration with an edge pre-notch machined in the fiber direction. Moderate impact speeds of up to 57 m/s were used. The lateral shearing interferometric technique of coherent gradient sensing (CGS) in conjunction with high-speed photography was used to visualize the failure process in real time. Mode-I cracks propagated subsonically with crack speeds increasing to the neighborhood of the Rayleigh wave speed. For asymmetric, mode-II, types of loading the results revealed highly unstable and intersonic shear-dominated crack growth along the fibers. These cracks propagated with unprecedented speeds reaching 7400 m/s, a speed which is more than three times the shear wave speed of the composite and almost equal to the dilatational wave speed of the composite along the fibers. For intersonic crack growth, the interferograms featured a shock wave structure typical of disturbances travelling with speeds higher than one of the characteristic wave speeds in the solid. In addition, high speed thermographic measurements are conducted

that show concentrated hot spots behind the crack tip indicating crack face frictional contact.

1 INTRODUCTION

Dynamic crack growth along weak planes is a predominant mode of failure in composites and other layered material systems. In the past years, bimaterial fracture specimens, fabricated by bonding a stiff material to a compliant material (featuring a mismatch in wave speeds), have been used to demonstrate the importance of highly transient and dynamic crack growth in heterogeneous solids. It was observed that interfacial crack tip speeds rapidly approach and exceed the shear wave speed of the more compliant material (Lambros and Rosakis, 1995; Liu, Huang and Rosakis, 1995; Singh and Shukla, 1996; Singh et al., 1997; Rosakis et al., 1998) thus reaching intersonic speeds with respect to this material. The term intersonic crack tip speed is defined here to denote the crack tip speed which lies between the shear wave speed and the longitudinal wave speed. For crack tip speeds above the shear wave speed, a ray emanating from the crack tip across which there is a jump in shear tractions (shear shock wave) was predicted theoretically and was also observed experimentally and numerically (Liu, Huang and Rosakis, 1995, Singh and Shukla, 1996, Needleman and Rosakis, 1999). These high crack tip speeds were obtained under loading conditions that promoted locally shear dominated deformations at the crack tip which were further enhanced by the stress wave mismatch due to the mismatch of elastic properties across the interface. Also, the loading and the bond strength were such as to promote crack growth along the interface between the two solids (Lambros and Rosakis, 1995).

It has been observed that in homogeneous materials in the absence of a preferable crack growth path, mode-II crack propagation is not likely because the crack naturally kinks and propagates in a direction that causes a local mode-I stress state around the crack tip. This is not necessarily true in solids that may be homogeneous with respect to their constitutive properties but may involve preferable crack paths in the form of weak planes of lower fracture toughness (inhomogeneous in terms of their fracture toughness). Unidirectional composites indeed fit this description if viewed from the "macroscopic" point of view of a homogenized anisotropic theory. However, from the "microscopic" viewpoint, unidirectional composite materials are locally inhomogeneous and are related to bimaterials. Both material systems involve preferred crack growth directions, and are also composed of a stiffer material (the fiber) bonded together with a more compliant material (the matrix). From a macroscopic point of view such solids can be viewed as homogeneous anisotropic as far as their elastic properties are concerned. However, they are still inhomogeneous regarding their fracture toughness properties. Indeed, from both the macroscopic or microscopic view points the common characteristic between unidirectional composites and bimaterials is the existence of a weak straight line crack path which may accommodate growing cracks of both opening and shear modes. Because of the above observations and previous observations of intersonic crack growth in bimaterials, unidirectional composites seem to be natural candidates for studying maximum permissible speeds of cracks of both modes in a system that is, at least macroscopically, homogeneous.

While purely elastodynamic crack growth theory excludes intersonic growth of mode-I cracks, it does not exclude the possibility of intersonic mode-II crack growth in isotropic or anisotropic homogeneous elastic solids in cases of self similar cracks growing into their own planes (Broberg, 1989). By forcing the shear cracks to grow along a straight line path, several researchers (Freund, 1979, Georgiadis, 1986, Broberg, 1989, Huang *et al.*, 1999) theoretically calculated the critical speed in isotropic materials at which intersonic crack growth is possible to be $\sqrt{2}\, c_s$. For steady-state intersonic crack growth and in the absence of a cohesive crack tip structure, this is the only speed at which the energy release rate is non-zero and finite. Singular asymptotic analyses of intersonic crack growth in anisotropic materials were developed by Piva and Hasan (1996) and Huang *et al.* (1999). Shear cracks and dislocations moving intersonically in anisotropic solids were also discussed simultaneously by Gao et al. (1999). They predicted that, just as in isotropic materials, intersonic shear crack growth involving a finite energy release rate is possible at a specific critical speed, v_c, which lies within the intersonic interval. However, in the case of anisotropic materials, this speed is the product of a complex function of the anisotropic material properties and the shear wave speed. More recently, Broberg (1999) developed a cohesive zone analysis to investigate the same phenomenon in orthotropic materials. The advantage of using a cohesive zone is that the pathology of predicting zero energy release rates through most of the intersonic regime is eliminated. Broberg's work showed that the crack tip solution furnishes a finite and positive energy release rate throughout the intersonic regime, which has a distinct maximum at values close, but not equal, to the critical speed v_c predicted by the singular theories. Moreover, the proximity of that maximum to the critical speed v_c depends on the details of the

cohesive model and coincides with v_c as the cohesive zone size shrinks to zero. In isotropic materials, Burridge *et al.* (1979) using a slip weakening cohesive zone model concluded that shear cracks propagating only at speeds between the critical speed $\sqrt{2}c_s$ and the longitudinal wave speed, c_l, were stable in the intersonic regime.

To our knowledge, very few detailed experimental studies of either quasi-static or dynamic crack propagation in fiber-reinforced composites have been performed. Liu et al. (1998) investigated quasi-static fracture of polymer composites using the optical technique of CGS. Khanna and Shukla (1994) extended the theoretical model of Piva and Viola (1988) and used it to analyze measurements from strain gages and to determine mode-I dynamic stress intensity factors for cracks propagating subsonically in unidirectional glass-epoxy composite laminates at constant speed. Lambros and Rosakis (1997), using CGS shearing interferometry in conjunction with high-speed photography, looked at the initiation and growth in thick unidirectional graphite-epoxy composite plates under symmetric one point impact loading. They observed crack tip speeds for mode-I loading which approached $0.5c_R$, where c_R is the speed of the Rayleigh surface waves travelling in the direction of the fibers of a half space (one major direction of anisotropy). Finally, Liu et al. (1997), also used CGS and high speed photography to investigate the dependence of the mode-I dynamic fracture toughness on crack tip speed. In this study, the cracks were observed to propagate along the fibers as fast as $0.8\ c_R$.

The first experimental observations of intersonic crack tip speeds in unidirectional composite plates were made by Rosakis et al. (1997). Their experiments were

subsequently numerically analyzed by Haberman et al. (1997) and by Stout et al. (1998). Both experimental and numerical studies showed cracks growing at an average speed of 5000 m/s from the edges of a hole in a fiber reinforced unidirectional composite plate after this plate was impacted in the direction of the fibers (figure 1). Two intersonic shear cracks propagating parallel to the fibers from the boundary of the hole towards the impact face can be observed in this figure. A distinctive shock wave structure emanating from the crack tip is also visible. These experiments, together with prior experience in bimaterials, pointed to the possibility of intersonic crack growth under suitable shear dominated loading conditions and paved the way for the present detailed investigation of this phenomenon.

In this paper, we present the first extensive experimental results pertaining to highly dynamic crack propagation in unidirectional graphite-epoxy composite plates under both mode-I and mode-II loading. The optical technique of CGS was used in conjunction with high-speed photography to scrutinize the crack growth process. Crack tip speed histories were then computed from the interferograms and the limiting crack tip speeds were thus determined. We show that intersonic crack growth takes place along the fibers in specimens loaded in such a way as to create predominately mode-II conditions at the crack tip. These intersonic shear cracks accelerate to very high speeds, both with respect to the maximum dilatational speed, which was very closely approached, and in absolute measure, up to 7400 m/s, which is the highest crack speed ever recorded. For cases in which the loading results in pure mode-I opening, only sub-Rayleigh crack growth is observed.

2 MATERIAL AND SPECIMEN GEOMETRY

2.1 Material and homogenized material properties

A cross section of the composite material is shown in figure 2. The fiber-reinforced unidirectional graphite/epoxy composite plates were manufactured by Composite Mirror Applications, Arizona, from 48 layers of graphite fiber and epoxy matrix pre-pregs laid up in the thickness direction to form a 6.3-mm thick plate. The fiber diameter was 7.3 μm and the volume fraction of the fiber in the pre-preg was 60-65%. The surface on one side of the composite plate was made optically flat by adding a thin layer of epoxy on one surface and then curing the composite specimen upon an optically flat glass plate. This surface was then made specularly reflective by coating with a thin layer of aluminum of 1-2 μm thickness in a vacuum deposition chamber. The glass transition temperature of epoxy matrix was 132 C (270° F). The Poisson's ratio for matrix was 0.3 and for the fiber was 0.2.

The orientation of an orthonormal coordinate set with respect to the composite plate is shown in figure 2. The x_1-axis is defined to lie along the fibers, the x_3-axis is perpendicular to the plane of the composite surface (with an outward pointing unit vector), while the x_2-axis is perpendicular to the x_1-x_3 plane. If we assume the fibers are randomly distributed in the epoxy matrix, then the x_2-x_3 plane can be taken as a plane of isotropy and, macroscopically, the material may then be considered a transversely

isotropic material. The stresses are then related to the strains by the stiffness matrix as (Christensen, 1979):

$$\begin{bmatrix} \sigma_1 = \sigma_{11} \\ \sigma_2 = \sigma_{22} \\ \sigma_3 = \sigma_{33} \\ \sigma_4 = \sigma_{23} \\ \sigma_5 = \sigma_{13} \\ \sigma_6 = \sigma_{12} \end{bmatrix} = \begin{bmatrix} c_{11} & c_{12} & c_{12} & 0 & 0 & 0 \\ c_{12} & c_{22} & c_{23} & 0 & 0 & 0 \\ c_{12} & c_{23} & c_{22} & 0 & 0 & 0 \\ 0 & 0 & 0 & c_{44} & 0 & 0 \\ 0 & 0 & 0 & 0 & c_{66} & 0 \\ 0 & 0 & 0 & 0 & 0 & c_{66} \end{bmatrix} \begin{bmatrix} \varepsilon_1 = \varepsilon_{11} \\ \varepsilon_2 = \varepsilon_{22} \\ \varepsilon_3 = \varepsilon_{33} \\ \varepsilon_4 = 2\varepsilon_{23} \\ \varepsilon_5 = 2\varepsilon_{13} \\ \varepsilon_6 = 2\varepsilon_{12} \end{bmatrix}, \tag{1}$$

where $c_{44} = \dfrac{c_{22} - c_{23}}{2}$.

The stiffness matrix for a transversely isotropic matrix consists of five independent parameters: c_{11}, c_{22}, c_{12}, c_{23}, and c_{66}. These parameters are related to the easily measurable mechanical moduli E_1, E_2, μ_{23}, μ_{12}, and ν_{12}. These moduli can be expressed in terms of the original stiffness matrix components by

$$\begin{aligned} E_1 &= c_{11} - \frac{2c_{12}^2}{c_{22} + c_{23}}, \\ E_2 &= \frac{(c_{22} - c_{23})(c_{11}c_{22} + c_{23}c_{11} - 2c_{12}^2)}{c_{11}c_{22} - c_{12}^2}, \end{aligned} \tag{2}$$

$$\begin{aligned} \nu_{12} &= \frac{c_{12}}{c_{22} + c_{23}}, \\ \nu_{23} &= \frac{c_{23}c_{11} - c_{12}^2}{c_{11}c_{22} - c_{12}^2}, \\ \mu_{12} &= c_{66}, \end{aligned}$$

$$\nu_{21} = \frac{c_{12}(c_{22} - c_{23})}{c_{11}c_{22} - c_{12}^2} \text{ or } \frac{\nu_{12}}{E_1} = \frac{\nu_{21}}{E_2}, \tag{3}$$

and $\mu_{23} = \frac{c_{22} - c_{23}}{2} = \frac{E_2}{2(1+\nu_{23})}$.

The transversely isotropic elastic constants and the stiffness matrix for our graphite/epoxy unidirectional composite material are given in table 1. The reduced stiffness matrix for plane stress cases is also shown in table 1. This reduced stiffness matrix can be obtained from the mechanical properties through the following relations:

$$\begin{aligned} c'_{11} &= \frac{E_1}{1-\upsilon_{12}\upsilon_{21}} = c_{11} - \frac{c_{12}^2}{c_{22}}, \\ c'_{22} &= \frac{E_2}{1-\upsilon_{12}\upsilon_{21}} = c_{22} - \frac{c_{23}^2}{c_{22}}, \\ c'_{12} &= \frac{\upsilon_{21}E_1}{1-\upsilon_{12}\upsilon_{21}} = c_{12} - \frac{c_{12}c_{23}}{c_{22}}, \\ c'_{66} &= \mu_{12} = c_{66}. \end{aligned} \tag{4}$$

The shear modulus, μ_{12}, was determined by quasi-static Iosipescu shear tests while uniaxial compression tests were conducted on an MTS hydraulic testing machine to determine Young's moduli, E_{11}, E_{22} and the Poisson's ratio, υ_{12}. The calculated values for the stiffness components c_{11}, c_{22}, and c_{66} were also verified with those obtained from the plane strain longitudinal and shear wave speeds in the direction of the major axes through the following relations:

$$c_l^{\parallel} = \sqrt{\frac{c_{11}}{\rho}}, c_l^{\perp} = \sqrt{\frac{c_{22}}{\rho}}, \text{ and } c_s = \sqrt{\frac{c_{66}}{\rho}}, \tag{5}$$

where $c_l^{\parallel}$ denotes the dilatational wave speed parallel to the fibers while $c_l^{\perp}$ denotes the dilatational wave speed perpendicular to the fibers, and c_s is the shear wave speed. The mass density of the composite plate was 1478 kg/m^3. The longitudinal wave speeds perpendicular and parallel to the fibers and the shear wave speed were obtained using ultrasonic pressure and shear transducers operating at a frequency of 5 MHz. These wave speeds are shown in table 2. It was noticed that significant deterioration in material properties of the composite material took place within a one-year period. The wave speed measurements carried out on virgin specimens a year before the experiments were conducted resulted in 30% higher wave speeds than the wave speeds obtained a year later. This change is attributed to humidity and temperature effects on the composite degrading the fiber/matrix interface during the time the specimens were left sitting on the shelf. The wave speeds reported in table 2 are the ones measured just before the fracture experiments were conducted. Also shown are the plane stress longitudinal wave speeds obtained by replacing c_{ij} by the plane stress stiffness matrix c_{ij}' given in table 1. The bar wave speed in the graphite fiber was 11230 m/s and the dilatational wave speed in epoxy was 2500 m/s. The final row of table 2 shows the speed, $c_R^{\parallel}$, of Rayleigh waves propagating along the x_1 direction (parallel to the fibers) on the surface of an anisotropic half space and is obtained as the real root, $v = c_R^{\parallel}$, of the equation (Ting, 1996):

$$\left(\frac{c'_{11}c'_{22}-c'^{2}_{12}}{c'_{22}c'_{66}}-\frac{\rho v^2}{c'_{66}}\right)\sqrt{\frac{c'_{22}}{c'_{11}}\left(1-\frac{\rho v^2}{c'_{66}}\right)}-\frac{\rho v^2}{c'_{66}}\sqrt{1-\frac{\rho v^2}{c'_{11}}}=0 \qquad (6)$$

For the properties of our material, $c_R^{II} = 0.99\,c_s$.

2.2 Specimen geometry

Two geometries of specimens were used in the experiments reported in this paper. The first geometry consisted of single edge notch specimens of 127 mm in width and 203 mm in height (figure 3a). The fibers were parallel to the shorter edge of the specimen. A notch of 25 mm in length and 1.5 mm in width was machined parallel to the fibers using a diamond saw. During the experiments, cracks initiated from this blunt notch. The blunted initial notch allows more strain energy to be stored prior to the generation of the dynamically growing crack and thus this bluntness controls (to a certain degree) the initiation crack tip speed. A sharp crack was used in one case in order to obtain a less abrupt start start of crack propagation. As shown in the figure, these specimens were either loaded symmetrically or asymmetrically by impacting them with a steel projectile propelled by a gas gun. Very moderate impact speeds of up to 57 m/s were used. The second type of specimen, used only for mode-II crack growth, was a 75 mm by 150 mm rectangular specimen with a 25 mm by 75 mm rectangular area removed from the center of one edge as shown in figure 3b. After impact with a projectile, shear cracks initiated from the slightly rounded corners of the rectangular cut-out and propagated towards the impact area. This specimen configuration is an adaption of the circular hole geometry described by Rosakis et al., (1997).

3 EXPERIMENTAL TECHNIQUE

3.1 Coherent gradient sensing technique with high-speed photography

A schematic of the experimental setup and of the optical technique of coherent gradient sensing, CGS, is shown in figure 4. The specimen was subjected to impact loading through a projectile fired from a gas gun. The projectile was 75 mm long, 50 mm in diameter and was made of hardened steel. A steel piece was bonded to the specimen at the impact site to prevent crushing of the composite plate during impact and to induce a planar loading wave front. The projectile speed was varied between 20 and 30 m/s for asymmetric loading and from 10 to 57 m/s for symmetric loading.

The dynamic stress field produced by the impact loading wave leads to a time varying out-of-plane displacement field on the surface of the composite plate. The optical technique of CGS by reflection was used in conjunction with high-speed photography to record in real time the slopes of this out-of-plane deformation field. CGS is a full-field, lateral-shearing interferometer. The details of CGS can be found in several articles (Tippur *et al.*, 1991, Rosakis, 1993) and its application to crack initiation and subsonic growth in composite materials has been demonstrated before (Lambros and Rosakis, 1997, Rosakis *et al.*, 1997, Liu *et al.*, 1998).

The experimental setup used a coherent, monochromatic, collimated laser beam of 50 mm diameter which was incident on the specimen and was reflected from the initially optically flat and specularly reflective surface. Subsequently the reflected beam acquired

an optical path difference due to the nonuniform specimen surface deformations generated near the crack tip after impact. The reflected beam passed through two high-density line diffraction gratings G_1 and G_2 of pitch p = 0.0254 mm (40 lines/mm). The lines of the gratings were parallel to the x_2 direction. The separation distance between these gratings is denoted by Δ and is typically 40 to 60 mm. The gratings diffracted the reflected beam and recombined it with itself to form an interferogram. The light from the gratings was collected by a filtering lens L and a diffraction spot pattern was obtained on the filtering plane, which was located at the back focal plane of the lens L. By using a filtering aperture, all but either of the ±1 diffraction orders were blocked. One of those two remaining diffraction spots was imaged to produce an interference pattern on the image plane of a camera.

CGS, when used in reflective mode, measures the in-plane gradients of out-of-plane displacements;

$$\frac{\partial u_3}{\partial x_1} = \frac{mp}{2\Delta}, \quad m = 0, \pm 1, \pm 2, \ldots, \tag{7}$$

where $u_3(x_1, x_2)$ is the out-of-plane displacement field of the reflective surface of the specimen, p and Δ are the pitch and separation of the two high-density gratings, and m is the fringe order for the x_1 gradient contours. According to the above equation, which holds when the lines of the gratings are parallel to the x_2 direction, each CGS fringe is a locus of points that have the same slope in the x_1-direction. Under conditions of plane stress, $u_3(x_1, x_2)$ is related to the thickness averages of the stresses as follows (see Lambros and Rosakis, 1997 and Liu et al., 1998.):

$$u_3 = \frac{h}{2}\left\{b_{31}\sigma_{11} + b_{32}\sigma_{22}\right\}, \tag{8}$$

where h is the specimen thickness and b_{ij} are components of the compliance matrix $\underline{b}$, inverse to the stiffness matrix $\underline{c}$ in equation (1), for the particular case of plane stress state.

The interference pattern was captured by a rotating mirror type high-speed camera (Cordin model 330A). The camera is capable of recording 80 frames at framing rates of up to 2 million frames per second. In the current experiments, the interframe time in the experiments varied from 0.69 - 1.39 μs and the image was recorded on 35 mm black and white film (Kodak TMAX-400). The laser used was an argon-ion laser operating at a wavelength of 514.5 nm in a pulsed mode of 8ns pulse width. The recording process of the event commenced with the impact of the projectile on a strain-gage mounted on the steel plate, leading to a sharp voltage jump, thus triggering the pulsing of the laser.

3.2 High-speed infrared thermography

On some shear dominated crack growth experiments, infrared thermography was also used to observe crack face frictional contact. While on one side of the specimen (reflective side) the optical technique of CGS in reflection was used on the other side, simultaneously, a full-field, high-speed infrared imaging system was employed to measure the evolving, two-dimensional temperature field.

Since the events we are trying to observe occur over a few microseconds, a thermal camera designed to capture images at a rate of 10^6 /s with a system rise time of 750 ns is used (Zehnder et al., 2000). At the heart of the system is an 8 x 8 focal plane array of HgCdTe IR detector elements. Each detector element is 100 μm x 100 μm, with center to center spacing of 130 μm. The detectors are housed in a liquid nitrogen dewar and are operated at a temperature of 77 K to maximize the signal to noise ratio. The camera is focused on 1.1 mm by 1.1 mm area ahead of the notch tip. Radiation emitted from the object as it deforms and heats up is focused onto the IR focal plane array. In order to convert the voltage signals from the detectors to corresponding temperatures on the specimen, an output signal vs. temperature calibration curve was obtained for our graphite/epoxy composite.

4 EXPERIMENTAL OBSERVATIONS

4.1 Symmetric crack-tip loading

Symmetric Mode-I crack tip deformations were attained by impacting the specimen symmetrically along the notch line by a steel projectile with projectile speeds varying from 10 m/s to 57 m/s (see figure 3(a)). A selected sequence of experimental CGS interferograms corresponding to mode-I crack initiation and propagation are shown in figure 5 for the highest impact speed of 57 m/s. Only four out of the eighty interferograms are presented here. The two frames show the CGS interference fringe patterns that has developed around the notch tip 2.1 μs before crack initiation and the fringe pattern corresponding to crack growth at 12.5 μs after initiation. Using the entire

sequence of pictures obtained from such an experiment, the crack tip history is recorded as a function of time in figure 6(a) for Mode-I symmetric loading. The crack length speed history is then obtained by differentiation by using a sectional, quadratic 3-point fit to the crack length history and is shown in figure 6(b). The crack is found to grow subsonically at 1350 m/s and accelerated to the Rayleigh wave speed $c_R^{\parallel}$ of the composite in the direction of the fibers ($c_R^{\parallel}$ = 1548 m/s). If one regards the small oscillations in the calculated crack tip speeds as experimental error, the crack tip speed does not exceed the Rayleigh wave speed.

4.2 Shear dominated crack-tip loading

Asymmetric one point bend impact experiments were conducted at a variety of impact speeds by impacting the specimen below the notch as shown in figure 3(a). In these experiments, projectile speed varied from 21 m/s to 30 m/s. For an impact speed of 21 m/s a sequence of four frames, selected from a sequence of 80 frames, taken with the high speed camera at an interframe time of 1.39 μs is shown in figure 78. The first three photographs show the CGS interference fringe patterns in a 50-mm diameter area around the notch tip at various times before crack initiation. The last frame corresponds to a time of 1.4 μs after crack initiation. The notch tip, as well as the stress concentration surrounding it, are both clearly visible in the first frame. The impact wave (compression) has propagated from one end of the plate to the other, has reflected as a tensile wave below the notch and has loaded the notch tip in a predominantly shear mode. A shadow of a marker for scaling appears at the top left side. The vertical line in the center is a streak line and is an artifact of the high-speed camera.

The notch-tip stress concentration is seen to increase as the CGS fringes increase in size and number. The nature of the fringe pattern shows that the near tip conditions are primarily mode-II. Indeed, they feature one fringe lobe in the back and two fringe lobes in the front which is a distinctive characteristic of asymmetric, mode-II CGS crack tip fringes (Rosakis, 1993; Liu et al., 1998). These pictures show the fringe patterns around the notch tip just before (8(c)) and just after crack initiation (7(d)). However, in the last frame, a significant change takes place in which the fringe loops are squeezed backwards indicating very high crack tip speeds and accelerations. Indeed, the average crack tip speed between these two frames is 2100 m/s, which is above the shear wave speed, c_s = 1560 m/s, for this material. Also, the initial acceleration is of the order of 10^9 m/s^2. This dramatic change in shape is not observed in the mode-I crack growth experiments described above. The notch tip is loaded by the arrival of the loading wave initially at 11 μs after impact and is fully loaded by the reflected wave at 15 μs. The crack initiates from the notch tip at approximately 32 μs.

A sequence of six CGS interferograms obtained at later times during the same experiment are shown in figure 8. These interferograms correspond to shear dominated dynamic crack growth along the fibers. As the crack propagates, it accelerates and further dramatic changes can be observed in the shapes of the crack-tip fringe patterns. The fringes are pushed further back and are elongated. The rear loop shape changes from rounded to a triangular wedge bounded by a line of highly concentrated fringes emerging from the crack tip at a well-defined angle. This line is caused by a steep change in the

stress gradients in a localized area, which later (as the crack exceeds the shear wave speed) forms a discontinuity in the stresses, i.e., a shear shock wave (for discussions of analytical and numerical models predicting such stress discontinuities during intersonic crack growth in bimaterials and composites see Liu et al., 1995, Rosakis et al., 1998, Huang et al., 1999, and Needleman and Rosakis, 1999).* Finally, this line broadens into two parallel lines (a double shock wave) which intercept the crack surfaces over a finite area of approximately 4-5 mm behind the crack tip. As will be discussed later, one possible reason for the observed double shock wave structure may be the existence of a finite size contact region behind the crack tip. A similar phenomenon of large scale contact during intersonic crack growth in bimaterials was initially reported in the experiments by Lambros and Rosakis (1995) and numerically confirmed by Needleman and Rosakis (1999). In addition, the existence of a double shock wave structure resulting from contact in bimaterials was discussed by Singh and Shukla (1996) and Rosakis et al., (1998) and was analytically modeled by Huang et al., (1998). The slope of the shear shock wave changes as you move away from the crack tip which may be due to unsteady

---

* In homogeneous, isotropic materials the out-of-plane surface displacement field, and thus CGS, is sensitive to the sum of the normal stresses. For such solids, this sum does not suffer a jump and as a result CGS cannot be used to detect such discontinuities. In anisotropic solids, however, normal and shear deformations are coupled, the out-of-plane displacements are related to σ_{11} and σ_{22} directly and not only through their sum. As discussed by Huang et al. (1999), each of these stress components indeed suffers a jump, in the intersonic regime which now causes a jump in out-of-plane displacements and their gradients. It is this phenomenon which allows us to indirectly observe discontinuities in stresses in our experiments (for an expression relating the out-of-plane displacement and its gradients to the stress in orthotropic solids see Liu et al., 1988).

crack growth. Furthermore, as the crack begins to move intersonically, the front fringe loops are pushed back by yet another line which is not as dramatic as the shock wave described above. Information regarding the crack tip deformation field cannot travel outside this outer line. The normal speed at which this outer line propagates is roughly 2500 m/s, which corresponds to the dilatational wave speed of epoxy, one of the two constituents of the composite plate. Thus, this second line of discontinuity seems to represent the dilatational shock wave in the additional epoxy layer on the surface due to a moving source (the crack tip) disturbance. The epoxy layer, which is added on the composite surface to make it optically flat, does not effect the homogenized composite properties. Although the speed of propagation of the outer line also seems to be consistent with $c_l^{\perp}$, a shock wave cannot form with respect to $c_l^{\perp}$ since the crack is moving intersonically parrallel to the fibers. Thus, the existence of this line would not be predicted by models of intersonic crack growth based on homogenized theories of composites of the type performed by Huang et al. (1999).

The instantaneous location of the crack tip is known from each frame which together with the interframe time is used to determine the crack length history as well as the crack tip speed history. These are shown in Figs. 10(a) and (b), respectively. The crack tip speeds were calculated using a three-point polynomial fit to the crack tip length history. The crack-tip speed approaches 6000 m/s, a speed which is 3.3 times higher than the shear wave speed and which is clearly intersonic. In this experiment the crack tip jumps immediately from rest to 2100 m/s becoming intersonic in the first frame after initiation, thus never crossing through the subsonic regime. Indeed, subsonic crack tip speed was

not observed at least within the time resolution of this experiment. The initial crack tip acceleration was also very high and was of the order of 10^9 m/s^2.

From figure 9(b) it can be seen that crack propagation had not reached steady state within our window of observation. A separate experiment was conducted under similar conditions with the field of view further downstream of the notch in order to investigate whether the crack tip speed eventually attains steady state conditions following the initial acceleration stage. In this experiment, the impact velocity was 28 m/s and the interframe time was 0.83 μs. A selected sequence of CGS fringe patterns are shown in figure 10. The crack tip position and speed history are plotted in figure 11(a) and (b), respectively. As already observed from the previous case, a shear shock wave and an outer dilatational shock wave, corresponding to the dilatational wave speed of the epoxy, are observed. However, in contrast to the previous experiment, a single dark line radiates from the crack tip. The first recorded crack tip speed is 4000 m/s as the crack appears within our field of view. The crack tip speed then climbs up and oscillates around and an average speed of 6500 m/s. The maximum crack tip speed is 7,400 m/s which is within experimental error, equal to the dilatational wave speed c_l along the x_1 direction (parallel to the fibers). This is the highest absolute crack tip speed ever observed in a laboratory setting or ever recorded in the open literature. However, it is inconclusive whether strict steady state has been reached as the slope of the shock wave away from the crack tip is still varying.

In another experiment, a crack was initiated from an artificially sharpened initial notch, a condition imitating a preexisting natural crack. A razor was used to extend the notch to a sharp crack and to promote initiation of crack growth at a lower level of far field shear stress. Indeed, the interferograms at crack initiation featured only a few fringes indicating that crack initiation took place before there was significant stress concentration at the crack tip. Thus we were able to initiate mode-II crack growth at a low impact speed and driving force. A selected sequence of CGS interferograms are shown in figure 12. The crack length history and the calculated crack tip speed history are given in figures 13(a) and 13(b), respectively. Since there was not enough energy stored before the crack initiated, the crack tip started subsonically at 1100 m/s and then entered the intersonic regime leveling off at around 6000 m/s. Thus, when a sharp starter crack was used, the subsonic shear crack growth regime was found to be accessible and to occur at substantially lesser impact speeds or far field stress levels. Moreover, the subsonically moving shear crack was then able to easily enter the intersonic regime and to eventually reach speeds that are of the order of 90% $c_l^{\parallel}$. Indeed, as is clearly visible in figure 13, a fully developed double shock structure is observed emanating from a 5 mm region behind the crack tip.

Yet another geometry that was tested was the plate with a rectangular cut-out in which we observed intersonic crack growth with a crack originating from the cut-out corner (figure 3b). In this case the specimen is impacted by a steel projectile at 21 to 28 m/s and a plane wave propagates towards the cut-out. The wave reflects off the edge of the cut-out in the center of the specimen whereas it continues moving along the two arms. This

imposes a differential particle velocity to the center beam which loads both corners of the cut-out in shear mode. A selected sequence of CGS interferograms are shown in figure 14. The loading phase of this experiment can be seen in the first frame. After initiation, the crack propagated to the right (towards the impact area) intersonically, featuring a characteristic shear shock wave structure similar to our previously described experiments. Typical crack tip speed history is shown in figure 15. The crack initiated within the intersonic interval at 3000 m/s and accelerated rapidly to just less than 6000 m/s.

4.3 Observations of frictional contact in shear-dominated crack growth

The general features of the CGS fringe patterns surrounding a shear-dominated crack propagating intersonically are summarized in figure 16. This figure shows a close-up area of 30 mm by 10 mm in size around the propagating crack. A distinct common feature that can be observed in all photographs shown in this figure is the existence of lines, or sets of lines, separating regions of varying fringe density. These lines radiate from the neighborhood of the crack tip at different angles. The first, inner, set of lines bounds a relatively dark strip radiating from behind the crack tip at a shallow angle to the crack faces. These inner lines first appear as the crack begins to move intersonically. The dark strip between these lines could be a shadow spot (reflected light does not reach the film within the camera) or is the result of caustic formation (when the camera is not focused accurately on to the specimen surface). Both of these possibilities are due to intense gradients of the out-of-plane displacements (see Rosakis 1983). These lines arise

when the crack tip speed is higher than the shear wave speed (c_s = 1560 m/s) and correspond to shear shock waves.

The second, outer, line radiates from the crack tip at a steeper angle to the crack faces. Indeed, as the crack begins to move intersonically, an outer envelope forms around the fringe pattern (bounded by this outer line) outside which information regarding the approaching crack tip has not been received. The normal speed at which this outer line propagates is roughly 2500 m/s which corresponds to the dilatational wave speed of epoxy, one of the two constituents of the composite plate. Thus, this second line of discontinuity seems to represent the dilatational shock wave in the epoxy layer due to a moving source, i.e., the crack tip (note that the crack tip is purely supersonic compared to the dilatational wave speed of the epoxy matrix). The existence of this, outer, line cannot be predicted by theoretical derivations based on homogenized anisotropic models which are incapable of differentiating between the various individual phases of the composite.

A significant feature of the fringe patterns shown in figures 16(a) and (b) is the radiation of double lines or shear shock waves from behind the crack tip. The crack tip speeds of these two cases are 5800 m/s and 5100 m/s, respectively. However, in figures 16(c) and 17(d) we can only see one distinct shear shock wave emanating from the crack tip at the higher speeds of 7020 m/s and 7360 m/s, respectively. We suggest here that the existence of the double shock wave structure indicates the presence of a contact region behind the crack tip of the type that has been earlier observed during intersonic crack growth in bimaterials (Lambros and Rosakis, 1995 and Singh and Shukla, 1996). At

higher speeds, the two distinct shock waves combine to one shock wave radiating from the crack tip and the contact zone seems to vanish. This behavior is reminiscent of the theoretical predictions of crack tip contact in bimaterials (Liu et al, 1995). In this work, intersonic cracks were found to feature contact zones at the crack tip speeds below a characteristic speed ($v \cong \sqrt{2}c_s$) which disappeared at higher speeds.

4.4 Temperature images

High-speed infrared images were taken of shear cracks, simultaneously, with high speed pictures in some of the crack growth experiments. We did not see appreciable temperature increase in a mode-I crack, within the constraints of the experimental setup and the sensitivity of the camera, in contrast to a shear crack. Figure 17 shows infrared thermal image results from one of the shear crack growth experiment. The camera is focused on 1.1 mm by 1.1 mm area ahead of the notch tip as shown in Fig. 17a. Figs. 17(b)-(f) show contours of constant temperature lines. In Fig. 17(b), the crack tip can be seen to be approaching from the left hand side. In Fig. 17(c), the crack has already left our field of view at 50μs after impact. Behind the crack tip we can observe local hot spots forming behind the crack tip due to crack surface sliding. These local hot spots of high temperature frequently jump around. The temperature increase is due to frictional sliding of the crack surfaces and later becomes a band of high temperature region enveloping several layers of fibers. This band grows in width and finally saturates the infrared detectors. The area where frictional sliding is taking place is of the order of 10μs. However, the temperatures measured are being averaged over a 100 μm ×100μm area for each detector so that the recorded temperatures are upper lower bounds for the

actual temperatures due to sliding. The hot spots indicate local contact points as also evidenced from finite element calculations (Yu et al., 2001).

4.5 Fracture surface morphology

The distinction between the mode-I and mode-II dynamic fracture processes for composites are clearly seen in post-mortem fractography with a scanning electron microscope. Figure 18 shows the fracture surface of a mode-I crack at two magnifications. Crack propagation has happened mostly in one plane. It can be seen that the fracture surface is mostly smooth and straight with the crack either going along the fibers or between them in the epoxy matrix. In some cases long fiber are drawn out.

For mode-II cracks, a more rough surface is observed with the crack grazing along the fibers (figure 19). Also we can observe 'zipper'-looking facets called hackles, that are microcrack formations in front of the crack that propagate into the specimen at an angle from the main crack. This is typically observed for composites with brittle resins (Bradley, 1991). We also have significantly more debris, as compared to mode-I crack, which can be attributed to extensive rubbing due to frictional contact of the crack face surfaces as pointed in the previous sections.

5 DISCUSSION

A view of the general trends in crack tip position history which are characteristic of many different experiments corresponding to very similar impact conditions can be observed in

figure 20. This figure simultaneously displays results from many different experiments, shows the reproducibility of the observed experimental trends (within the same geometry and loading conditions) and allows us to obtain an average sense of the trends in the time history of crack tip position for both the mode-I and the mode-II cases. The corresponding crack tip speed histories plotted as a function of crack tip location are shown in figure 21. Mode-I cracks initiate around 1300 m/s and subsequently the crack speed increases to the neighborhood of the Rayleigh wave speed. However, mode-II cracks initiate around 2000 m/s (intersonic) and rapidly accelerate to above 7000 m/s. Eventually these cracks asymptotically approach a steady state speed of approximately 6500 m/s.

In order to interpret the observed phenomena, theoretical analyses were developed Huang, *et al.* (1999) and Gao *et al.* (1999). They obtained the asymptotic stress and displacement fields near a steady state, intersonically propagating crack tip in an orthotropic material. In this analysis, the composite was modeled as an elastic, orthotropic, homogeneous solid. For both the mode-I and the mode-II cases, a prescribed straight line crack path was assumed. This models the experimental fact that both mode-I and mode-II cracks are confined to grow along the fibers of the unidirectional composite which correspond to the prescribed crack path of the analysis. The powers of the stress singularity for mode-I and mode-II cracks, denoted here by q_I and q_{II}, respectively, were found to vary with the material properties and crack tip speed and are shown in figure 22. The power of the stress singularity in mode-I, q_I, was found to be always larger than one half in the entire intersonic crack growth range resulting in an unbounded energy release

rate. In addition, close examination of the intersonic mode-I asymptotic field reveals that this unbounded energy release rate has a negative sign (negative infinity). This situation clearly indicates a physical impossibility since a propagating crack-tip needs a finite amount of positive energy to break the material bonds and cannot radiate out energy. Thus, it was concluded that within the assumptions of the singular crack tip model, a mode-I crack tip cannot propagate intersonically (for an equivalent argument for isotropic solids, see Broberg, 1989). This conclusion is also supported by our experiments in which the crack tip speed never exceeded the shear wave speed within experimental error, regardless of how large the impact velocity of the projectile was (see figure 21). For mode-II, intersonic crack growth the power of the stress singularity, q_{II}, varies from 0 to ½. It reaches ½ only at a single critical crack tip speed, v_c, where the energy release rate supplied by the elastic asymptotic field is finite and positive. Other intersonic crack tip speeds yielded a vanishing energy release rate. This critical crack tip speed, where $q_{II} = ½$, is given by

$$v_c = \sqrt{\frac{c'_{11}c'_{22} - c'^2_{12}}{\rho(c'_{12} + c'_{22})}} = \sqrt{\frac{E_1}{\rho(1+\nu_{12})}} = \sqrt{\frac{E_1}{\mu_{12}(1+\nu_{12})}}c_s. \qquad (9)$$

At $v = v_c$ the energy release rate is finite and positive. Since a positive and finite energy supply is required to break the material bonds in front of the crack tip, this speed corresponds to the only possible *steady state* intersonic crack growth speed according to the above asymptotic and singular steady state theory. Using the material properties given in table 1, this critical crack tip speed is approximately 6600 m/s. In our experiments, the mode-II crack tips seem to eventually reach this value sometimes from

below and sometimes from above. If there is not enough energy (e.g., at low impact speeds), then the crack tip asymptotically approaches this critical crack tip speed from below. If sufficient energy is imparted on the specimen, the crack tip unstably overshoots v_c. It eventually approaches this crack tip speed from above as the motion becomes increasingly steady.

The asymptotic analysis for mode-II also predicts a shear shock wave emanating from the intersonically propagating crack tip. This would correspond to the "inner" discontinuity line observed in the experiments to radiate from the crack tip at a shallow angle (see figures 16(c) and (d)). The outer discontinuity line is not predicted since the theory does not account for the heterogeneous nature of the composite. The equation for the ray of singularity propagating with the crack tip is given by the expression $\xi_1 + \mu_1 \xi_2 = 0$, where ξ_1 and ξ_2 are coordinate values with respect to a system of axes translating with the crack tip at an intersonic speed v and

$$\mu_1 = \sqrt{\frac{\sqrt{B^2 + 4AC} - B}{2A}}, \tag{10}$$

where

$$A = c'_{22} c'_{66},$$
$$B = c'_{11} c'_{22} - (c'_{22} + c'_{66}) \rho v^2 - c'^2_{12} - 2c'_{12} c'_{66}.$$
$$C = (c'_{11} - \rho v^2)(\rho v^2 - c'_{66})$$

Using the material properties given in table 1 and a crack tip speed of 7000 m/s, the angle between the shear shock wave and the crack faces, calculated from this expression is 18°

and that obtained from the experiments is 15°. The small discrepancy can be attributed to errors in the experimental determination of the crack tip speed, as well as to the possible variation of material properties with strain rate, especially near the crack tip where the strain rates are expected to be very high.

6 CONCLUDING REMARKS

Dynamic fracture experiments conducted in real time on pre-notched unidirectional fiber reinforced graphite/epoxy plates indicate that Mode-I (opening cracks) may only propagate subsonically along the fibers with respect to the homogenized anisotropic material properties with an upper bound of the Rayleigh wave speed. Mode-II (shear) cracks are, however, found to be capable of intersonic crack growth parallel to the fibers, typically accelerating from the vicinity of the shear wave speed to the dilatational wave speed along the fiber direction, c_L^{II}, and eventually approaching a particular critical intersonic speed, v_c, determined by the homogenized anisotropic material properties. Under particular circumstances, limited amount of unstable subsonic crack growth is also observed. Dual shock waves, which might imply a region of crack face contact, are formed at intersonic speeds less than v_c while a single shock wave becomes visible at higher speeds. The existence of frictional contact is supported further by high speed thermographic pictures showing concentrated hot spots behind the crack tip in addition to post-mortem SEM pictures of fracture surfaces. In absolute terms, unprecedented maximum crack tip speeds as high as 7,400 m/s are observed.

7 REFERENCES

Bradley, W. L., 1991, *Thermoplastic Composite Materials*, Ed. L. A. Carlsson, 295, (New York: Elsevier).

Broberg, K. B., 1989, *Int. J. Fract.*, 39, 1.

Broberg, K. B., 1999, *Int. J. Fract.*, 99,1.

Burridge, R., Conn, G., and Freund, L. B., 1979, J. Geophys. Res., 85, 706.

Christensen, R. M., 1979, *Mechanics of Composite Materials* (New York: Wiley).

Freund, L. B., 1979, *J. of Geophysical Research,* 84(B5), 2199.

Gao, H., Huang, Y., Gumbsch, P. and Rosakis, A.J., 1999, *J. Mech. Phys. Solids,* 47, 1941.

Georgiadis, H. G., 1986, *Int. J. Fract.*, 30, 175.

Haberman, K. S., Bennet, J. G., Liu, C., Stout, M. G. and Rosakis, A. J., 1997, *The dynamic inelastic behavior in fiber reinforced composite materials*, Los Alamos Technical Report, LA-13272-MS (Los Alamos).

Huang, Y., Wang, W., Liu, C. and Rosakis, A.J., 1998, *J. Mech. Phys. Solids*, 46, 2233.

Huang, Y., Wang, W., Liu, C. and Rosakis, A. J., 1999, *J. Mech. Phys. Solids*, 47, 1893.

Khanna, S. K. and Shukla, A., 1994, *Eng. Fract. Mech.* 47, 345.

Lambros, J. and Rosakis, A. J., 1995, *J. Mech. Phys. Solids*, 43, 169.

Lambros, J. and Rosakis, A. J., 1995, *Proc. Roy. Soc. A*, 451, 711.

Lambros, J. and Rosakis, A. J., 1997, *Comp. Sci. and Tech.*, 57, 55.

Liu, C., Y. Huang and Rosakis, A. J., 1995, *J. Mech. Phys. Solids*, 43, 189.

Liu, C., Rosakis, A.J., Ellis, R.W., Stout, M.G., 1997, *On the dynamic fracture of fiber reinforced composites using high speed photography and CGS interferometry*, GALCIT SM Report #97-10, (Pasadena: California Institute of Technology).

Liu, C., Rosakis, A. J., Ellis, R. W. and Stout, M. G., 1998, *Int. J. Fract.*, 90, 355.

Needleman, A. and Rosakis, A.J., 1999, *J. Mech. Phys. Solids*, 47, 2411.

Piva, A. and Viola, E., 1988, *Eng. Fract. Mech.*, 29, 535.

Piva, A. and Hasan, W., 1996, *J. Appl. Mech.*, 63, 933.

Rosakis, A. J., 1993, *Experimental Techniques in Fracture*, edited by J. S. Epstein (New York: VCH), pp. 327-425.

Rosakis, A. J., Liu, C., Stout, M. G. and Coker, D., 1997, *Observations of transonic shear and opening cracks in unidirectional composites containing cut-outs and holes*, GALCIT SM Report # 97-8, (Pasadena: California Institute of Technology).

Rosakis, A. J., Samudrala, O., Singh, R. P. and Shukla, A., 1998, *J. Mech. Phys. Solids*, 46, 1789.

Singh, R. P., J. Lambros, Shukla, A. and Rosakis, A. J., 1997, *Proc. Roy. Soc. A*, 453, 2649.

Singh, R. P. and Shukla, A., 1996, *J. Appl. Mech.*, 63, 919.

Stout, M.G., Liu, C., Ellis, R.W., Haberman, K.S., Bennett, J.G., Williams, P.O., Adessio, F.L. and Rosakis, A.J., 1998, *Proceedings of the 11th International Conference on Experimental Mechanics*, Oxford, United Kingdom, August 24-28, edited by I. M. Allison. In the special volume entitled, *Advances in Design Testing and Analysis* (A.A. Balkema/Rotterdam/Brookfield publishers), pp.187-192.

Ting, T. C. T., 1996, *Anisotropic Elasticity, Theory and Applications*, (New York: Oxford Univ. Press).

Tippur, H. V., Krishnaswamy, S. and Rosakis, A. J., 1991, *Int. J. Fracture*, 48, 193.

Yu, C., Ortiz, M., Coker, D. and Rosakis, A. J., 2001, in preparation.

Zehnder, A. T., Guduru, P. R., Rosakis, A. J., and Ravichandran, G., 2000, *Rev Scientific Instruments*, 71, 3762.

LIST OF TABLES

LIST OF FIGURES

Figure 9. Crack tip position (a) and crack tip speed (b) histories for a shear dominated crack propagating under asymmetric loading in an SEN specimen. Same experiment as in Figure 7.

Figure 10. A selected sequence of CGS interferograms for an intersonically propagating crack tip. Field of view is a 50 mm diameter circle ahead of the notch tip. (Mode-II, SEN geometry, blunted crack, impact velocity = 28 m/s).

Figure 11. Crack tip position (a) and crack tip speed (b) histories for a shear dominated crack propagating under asymmetric loading in an SEN specimen. Same experiment as in Figure 10.

Figure 12. A selected sequence of CGS interferograms for an intersonically propagating crack tip for a crack initiating from a sharp pre-crack. Field of view is around the initial crack tip. (Mode-II, SEN geometry, sharp crack, impact velocity = 28 m/s).

Figure 13. Crack tip position (a) and crack tip speed (b) histories for a shear dominated crack propagating under asymmetric loading in an SEN specimen. Same experiment as in Figure 12.

Figure 14. A selected sequence of CGS interferograms for an intersonically propagating crack tip that has initiated from a corner in a rectangular cut-out specimen. (Mode-II, rectangular cut geometry, impact velocity = 27 m/s).

Figure 15. Crack tip speed history for a shear dominated crack propagating in a rectangular cut-out specimen. Same experiment as in Figure 14.

Figure 16. Close-up view of the crack tip in intersonically growing cracks at different speeds showing the shock wave structure.

Figure 17. Specimen configuration (a) and high-speed infrared images of hot spot formation due to contact behind an intersonically moving shear crack (b-f).

Figure 18. Fracture surface morphology for a dynamically growing mode-I crack.

Table 1: In-plane material properties of the Graphite/Epoxy unidirectional composite.

3-D Stiffness Matrix (GPa)

c_{11}	c_{22}	c_{12}	c_{23}	c_{66}	c_{44}
82	11.1	4.0	4.9	3.6	3.1

Plane Stress Stiffness Matrix (GPa)

c'_{11}	c'_{22}	c'_{12}	$c'_{66} = c_{66}$
80.5	9.0	2.2	3.6

Elastic Material Properties

E_1	$E_2 = E_3$	$\nu_{12} = \nu_{13}$	ν_{23}	$\mu_{12} = \mu_{13}$	μ_{23}
80 GPa	8.9 GPa	0.25	0.43	3.6 GPa	3.1 GPa

Table 2: Characteristic plane-strain and plane-stress wave speeds.

	5 MHz Ultrasonic transducer (Plane strain)	Plane stress
	m/s	m/s
$c_l^{\parallel}$	7450 ±100	7380
$c_l^{\perp}$	2740 ± 100	2470
c_s	1560 ± 50	1560
$c_R^{\parallel}$	1548	1548

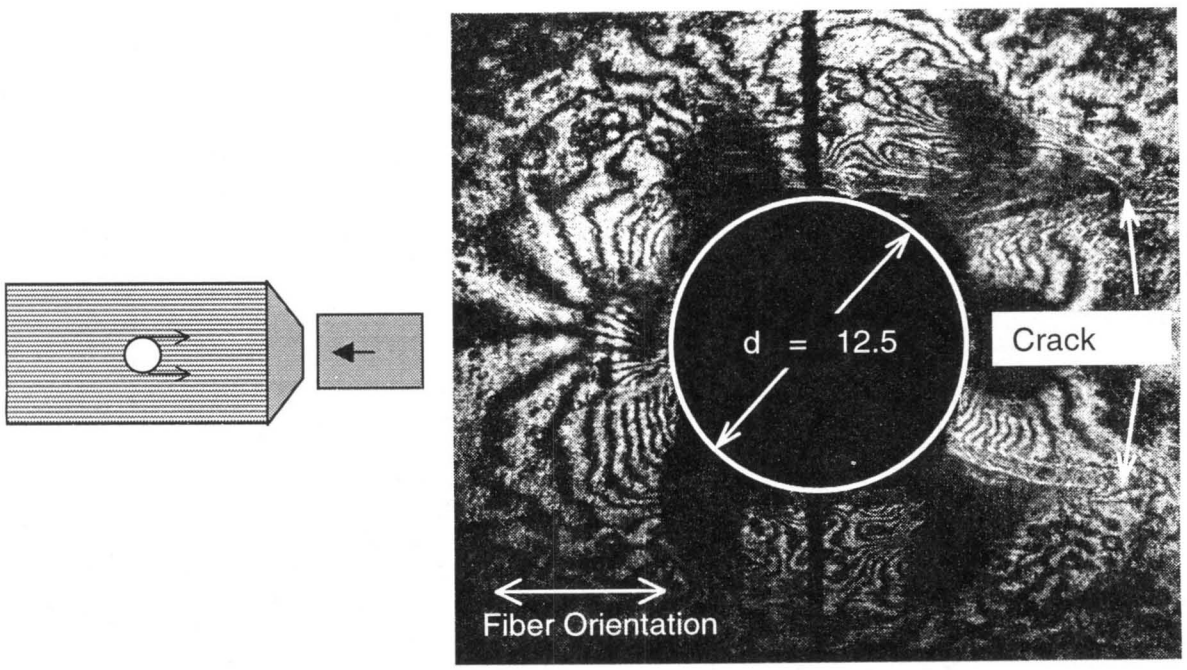

Figure 1

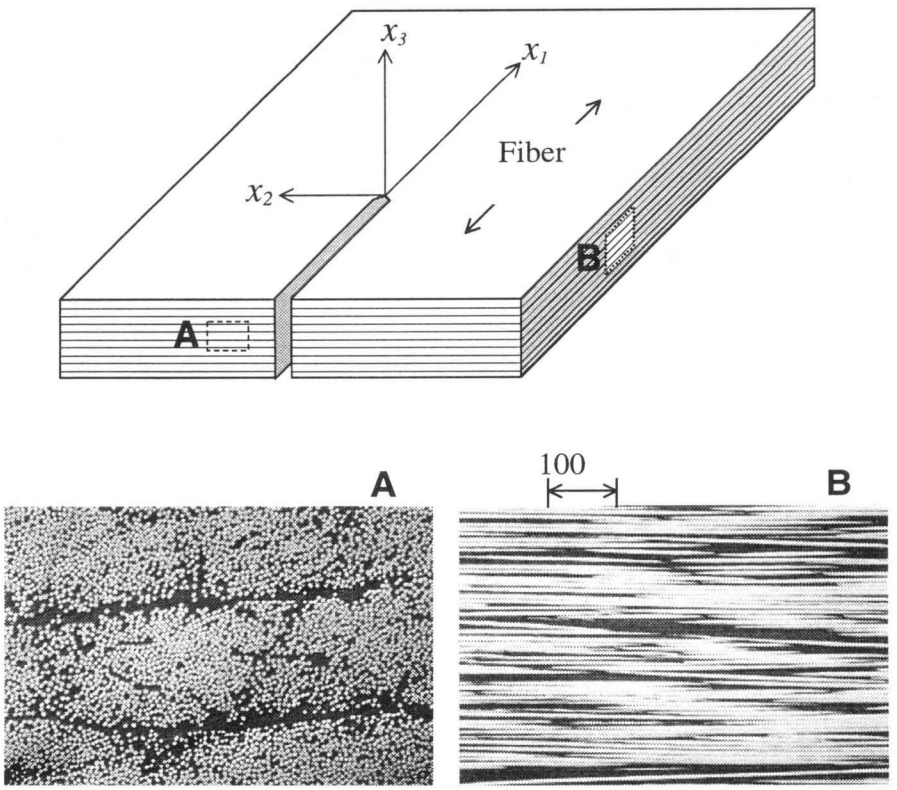

Figure 2

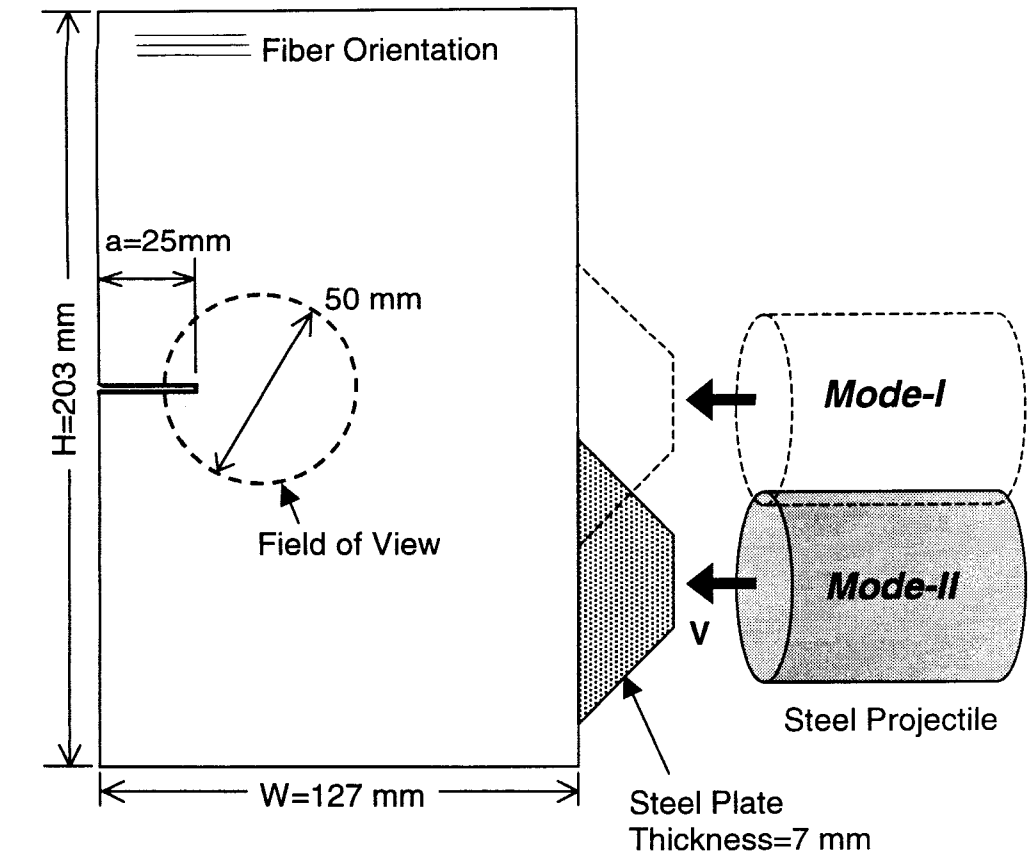
Fiber Orientation
a=25mm
50 mm
H=203 mm
Field of View
Mode-I
Mode-II
V
Steel Projectile
W=127 mm
Steel Plate
Thickness=7 mm

(a)

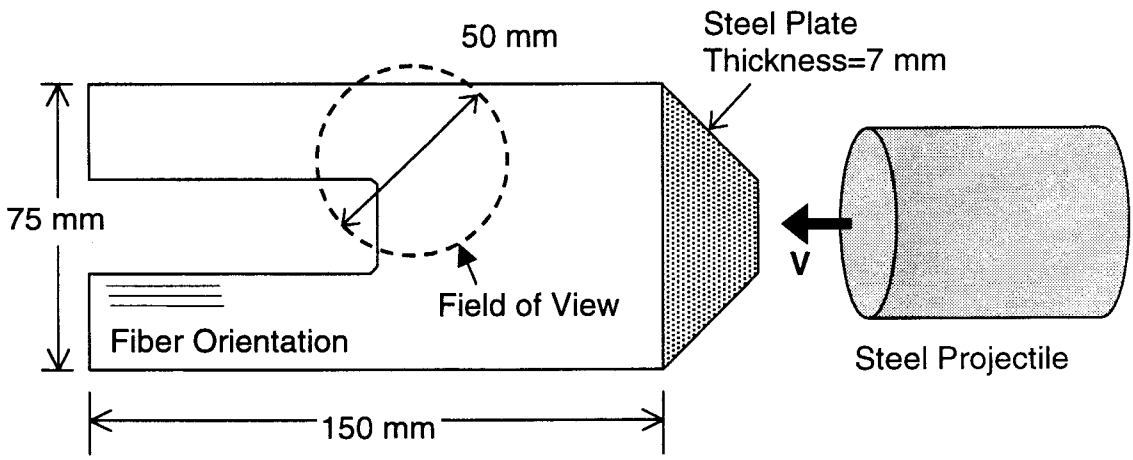
50 mm
Steel Plate
Thickness=7 mm
75 mm
Field of View
Fiber Orientation
V
Steel Projectile
150 mm

(b)

Figure 3

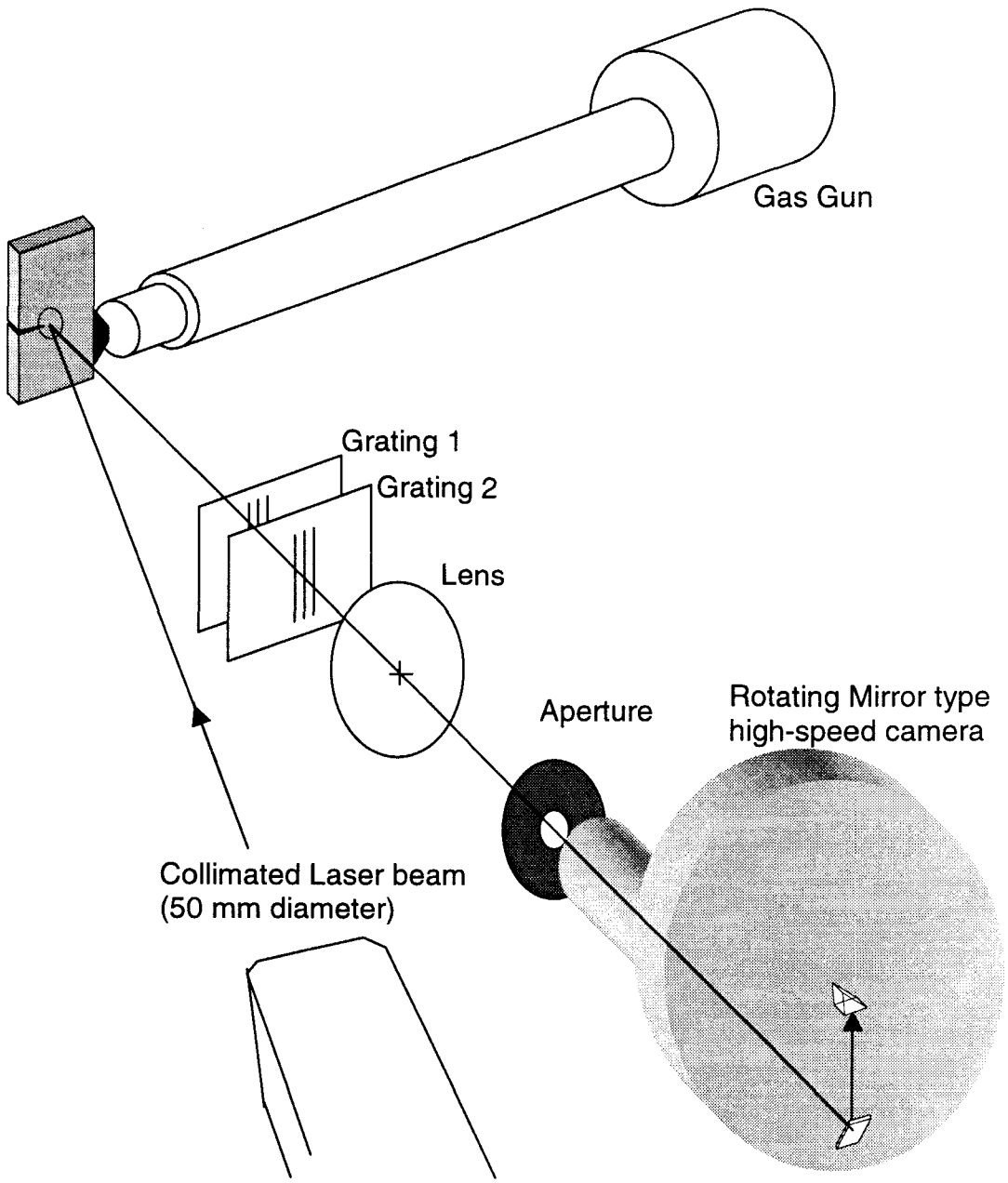
Gas Gun
Grating 1
Grating 2
Lens
Aperture
Rotating Mirror type
high-speed camera
Collimated Laser beam
(50 mm diameter)

Figure 4

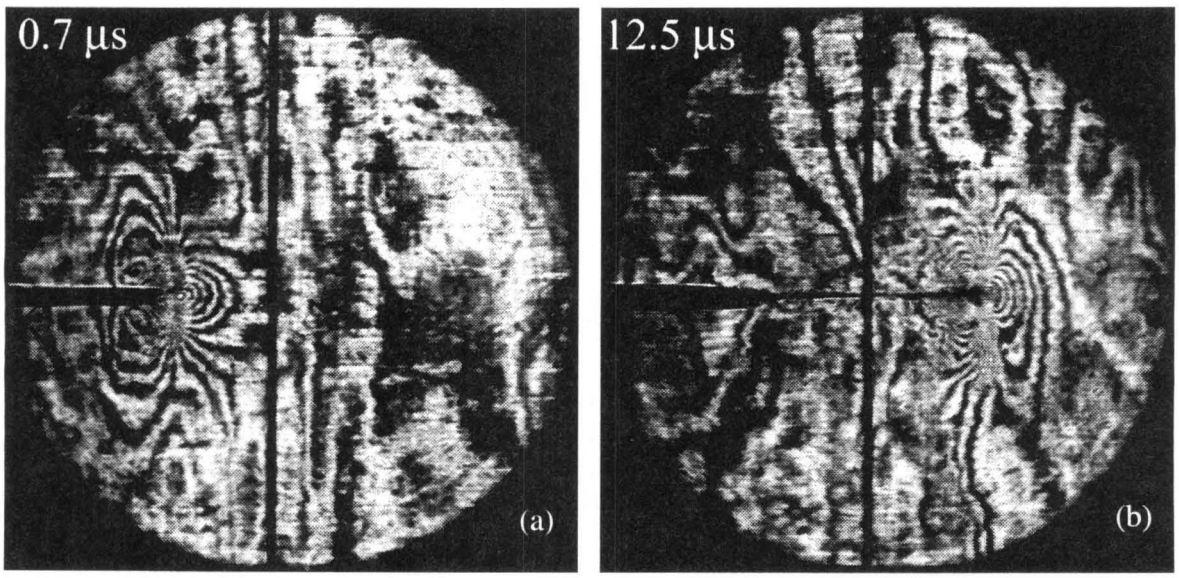

Figure 5

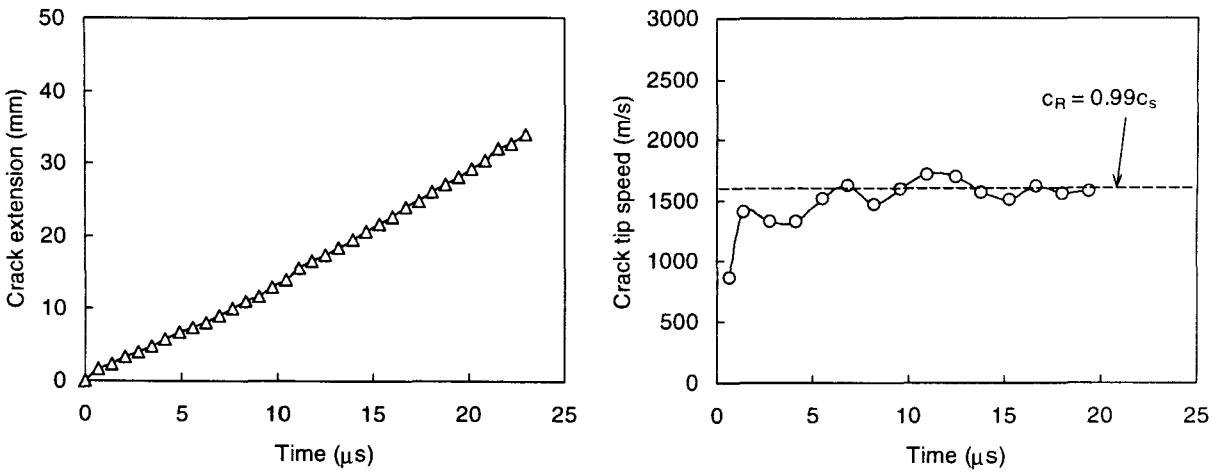
Crack extension (mm)
50
40
30
20
10
0
0
5
10
15
20
25
Time (μs)
Crack tip speed (m/s)
3000
2500
2000
1500
1000
500
0
$c_R = 0.99c_s$
0
5
10
15
20
25
Time (μs)

(a) (b)

Figure 6

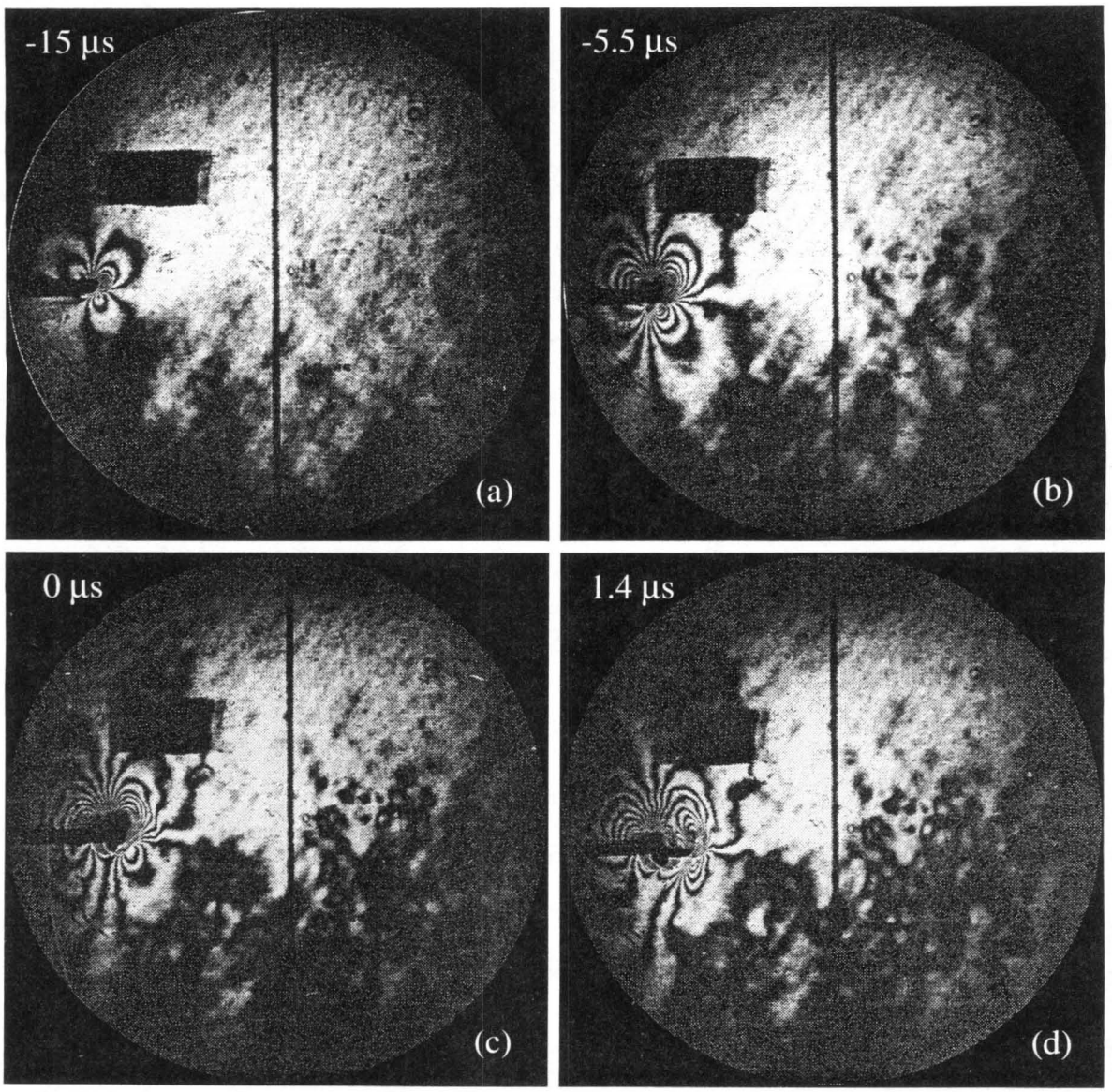

Figure 7

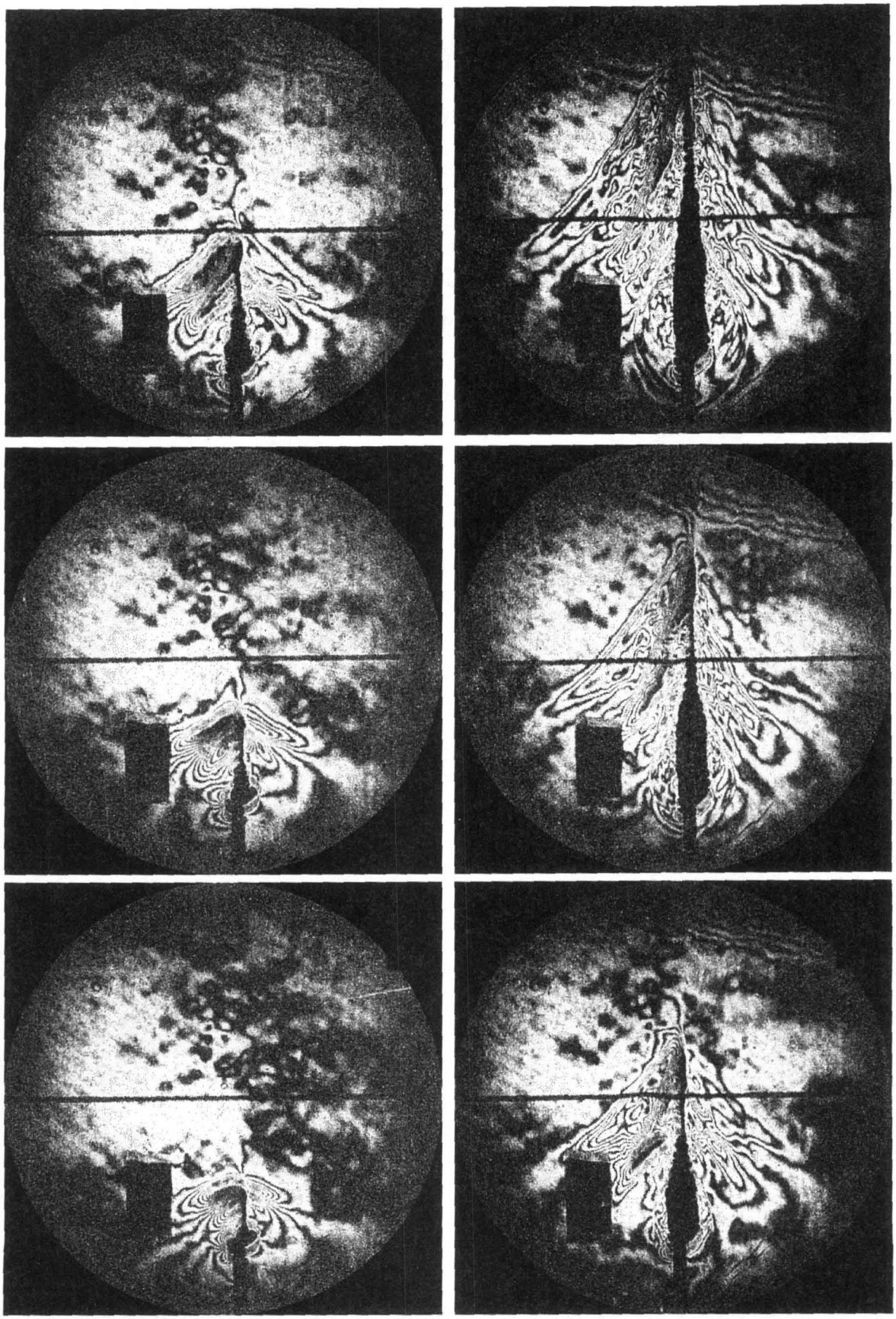

Figure 8

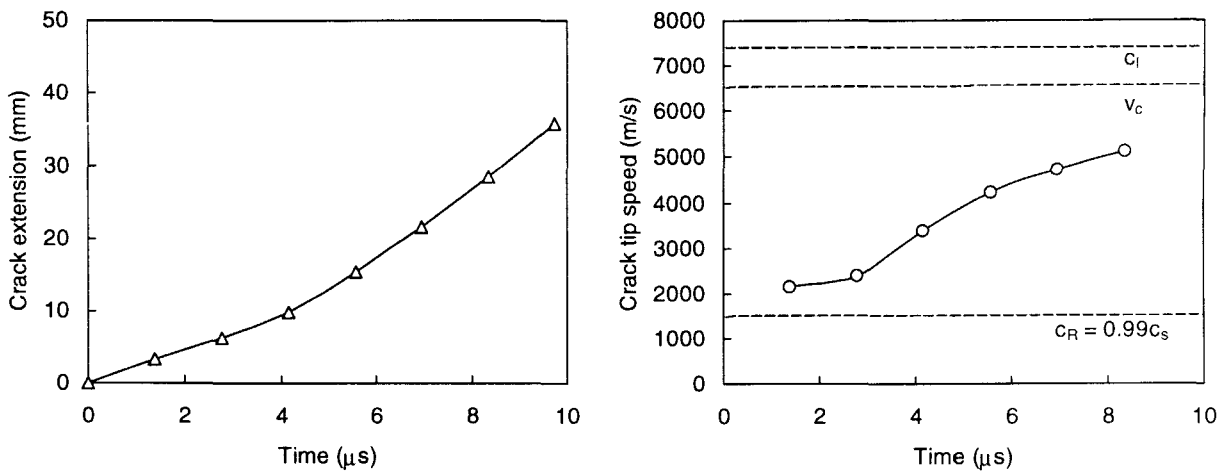
Crack extension (mm)
Time (μs)
(a)
Crack tip speed (m/s)
Time (μs)
c_l
v_c
$c_R = 0.99c_s$
(b)

Figure 9

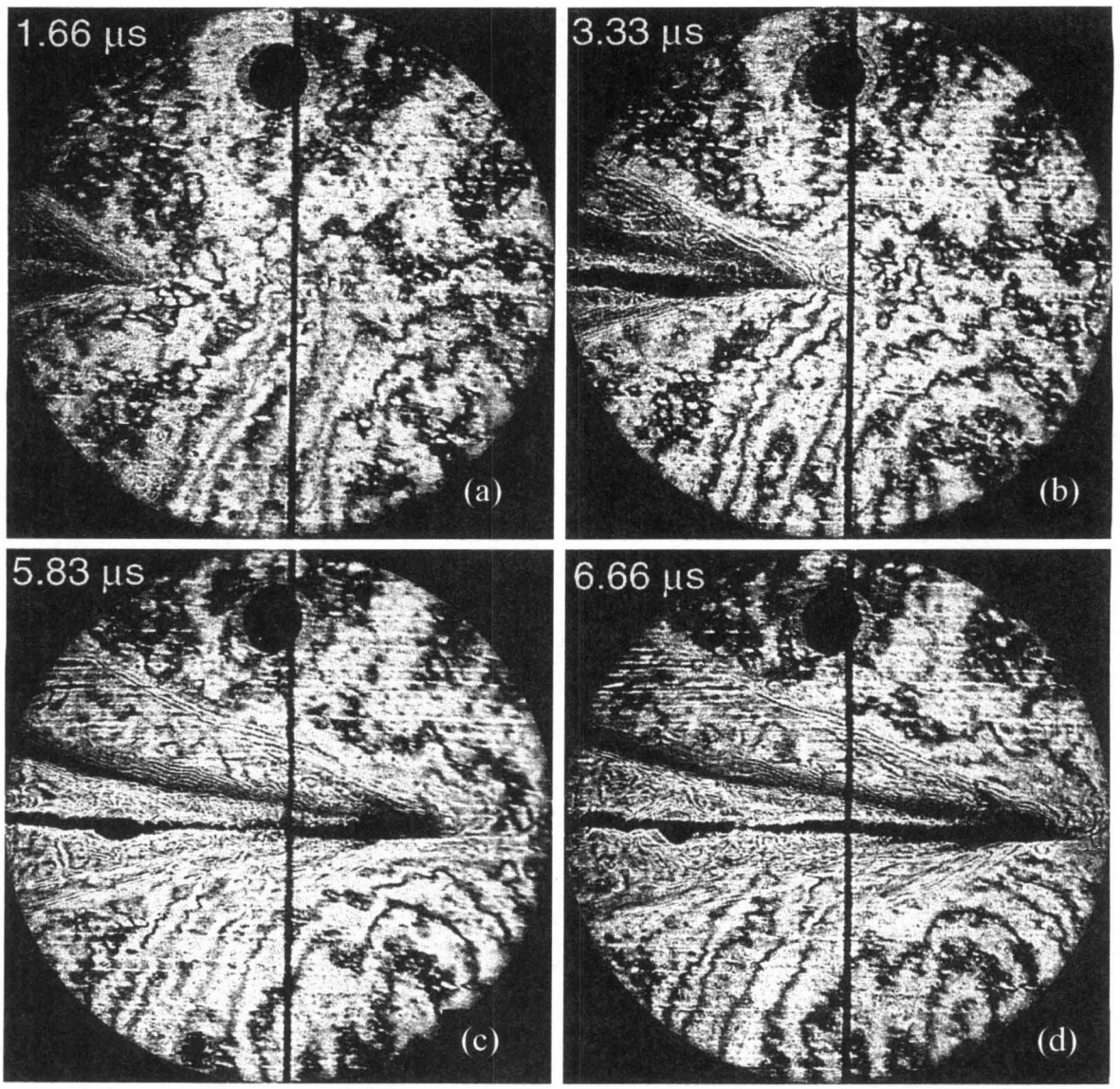

Figure 10

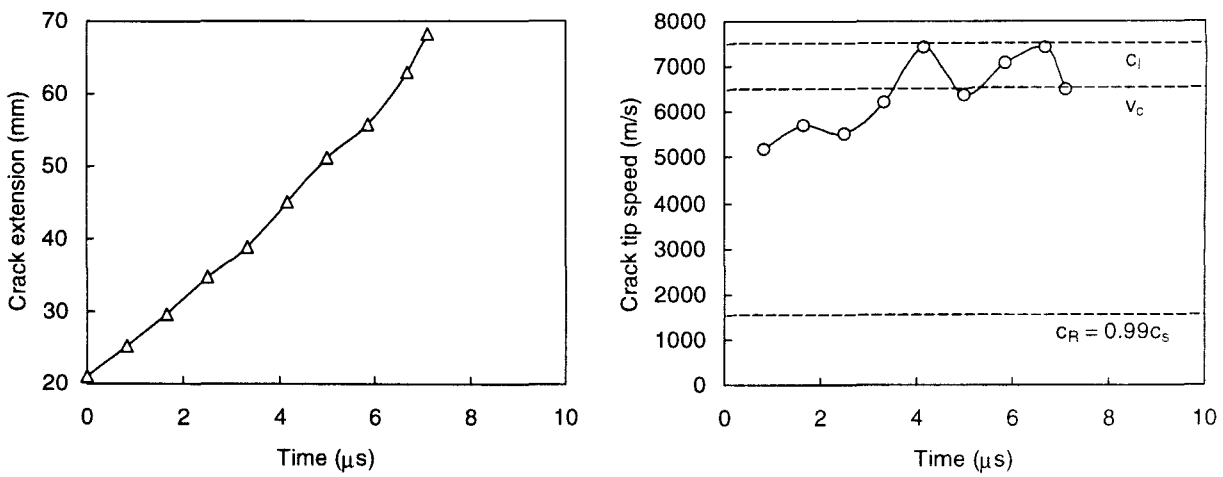
Crack extension (mm)
70
60
50
40
30
20
0
2
4
6
8
10
Time (μs)
Crack tip speed (m/s)
8000
7000
6000
5000
4000
3000
2000
1000
0
c_I
v_c
$c_R = 0.99c_S$
0
2
4
6
8
10
Time (μs)

(a) (b)

Figure 11

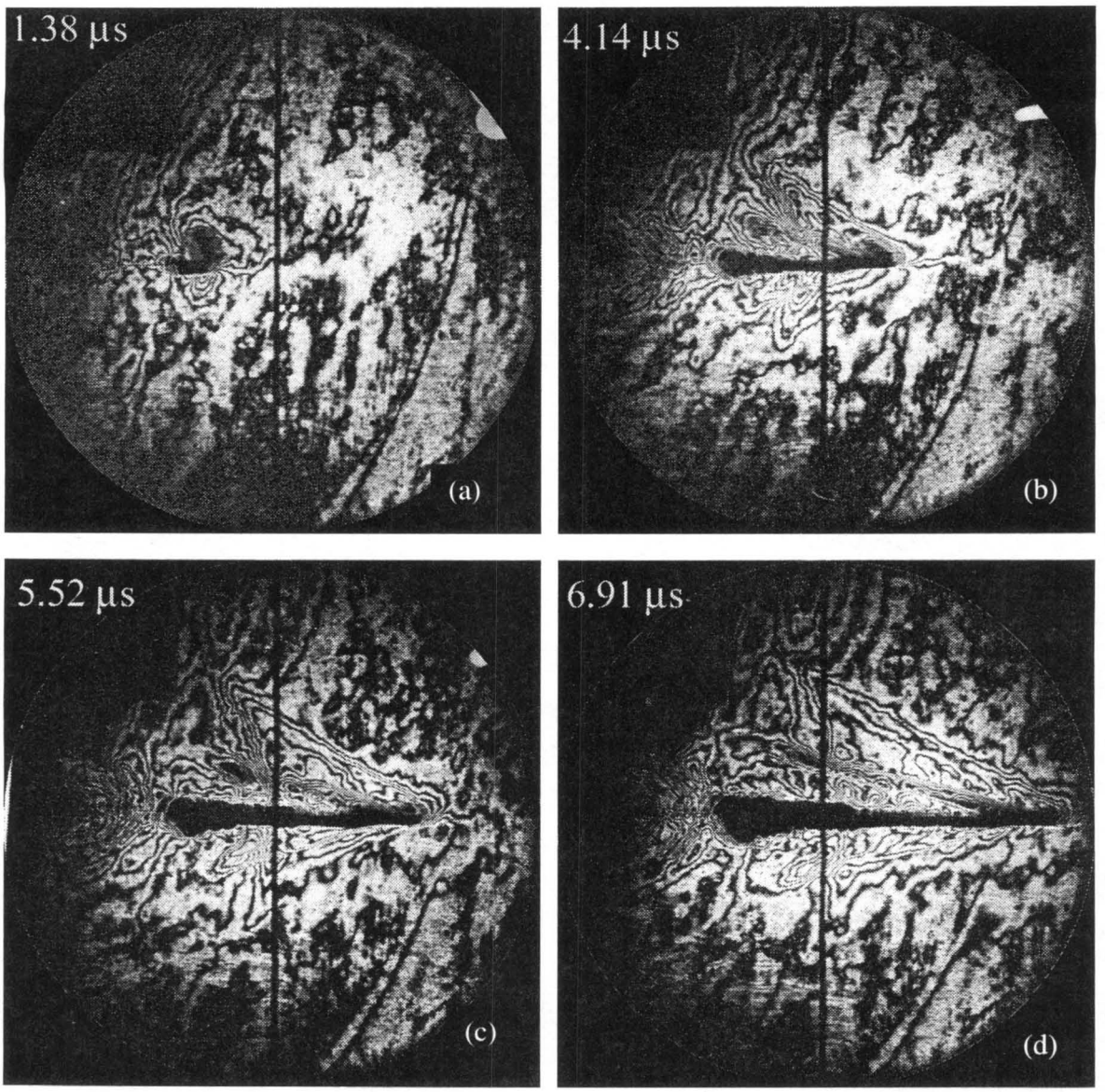

Figure 12

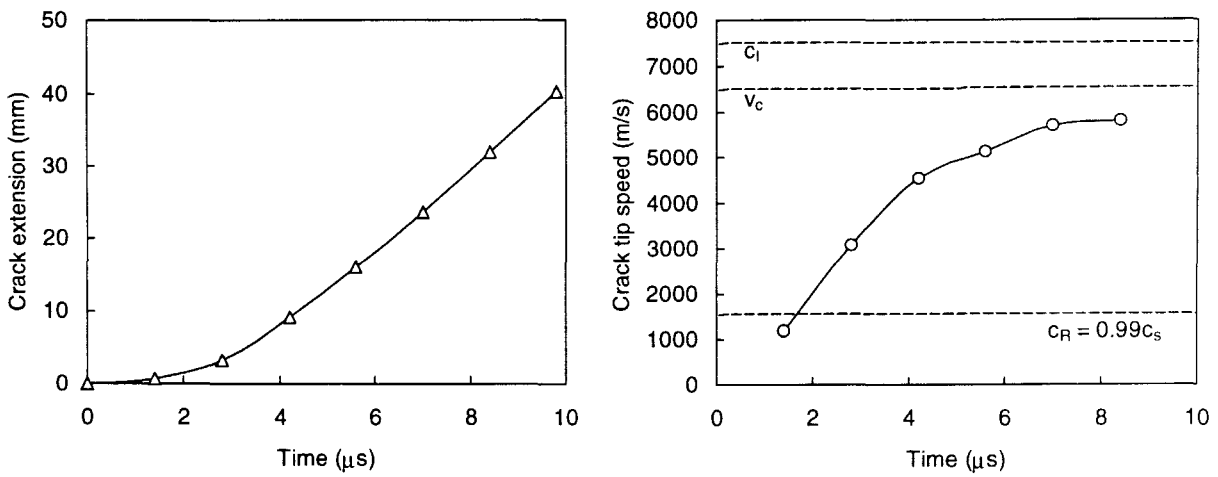
Crack extension (mm)
50
40
30
20
10
0
0
2
4
6
8
10
Time (μs)
Crack tip speed (m/s)
8000
7000
6000
5000
4000
3000
2000
1000
0
c_l
v_c
$c_R = 0.99c_s$
0
2
4
6
8
10
Time (μs)

(a) (b)

Figure 13

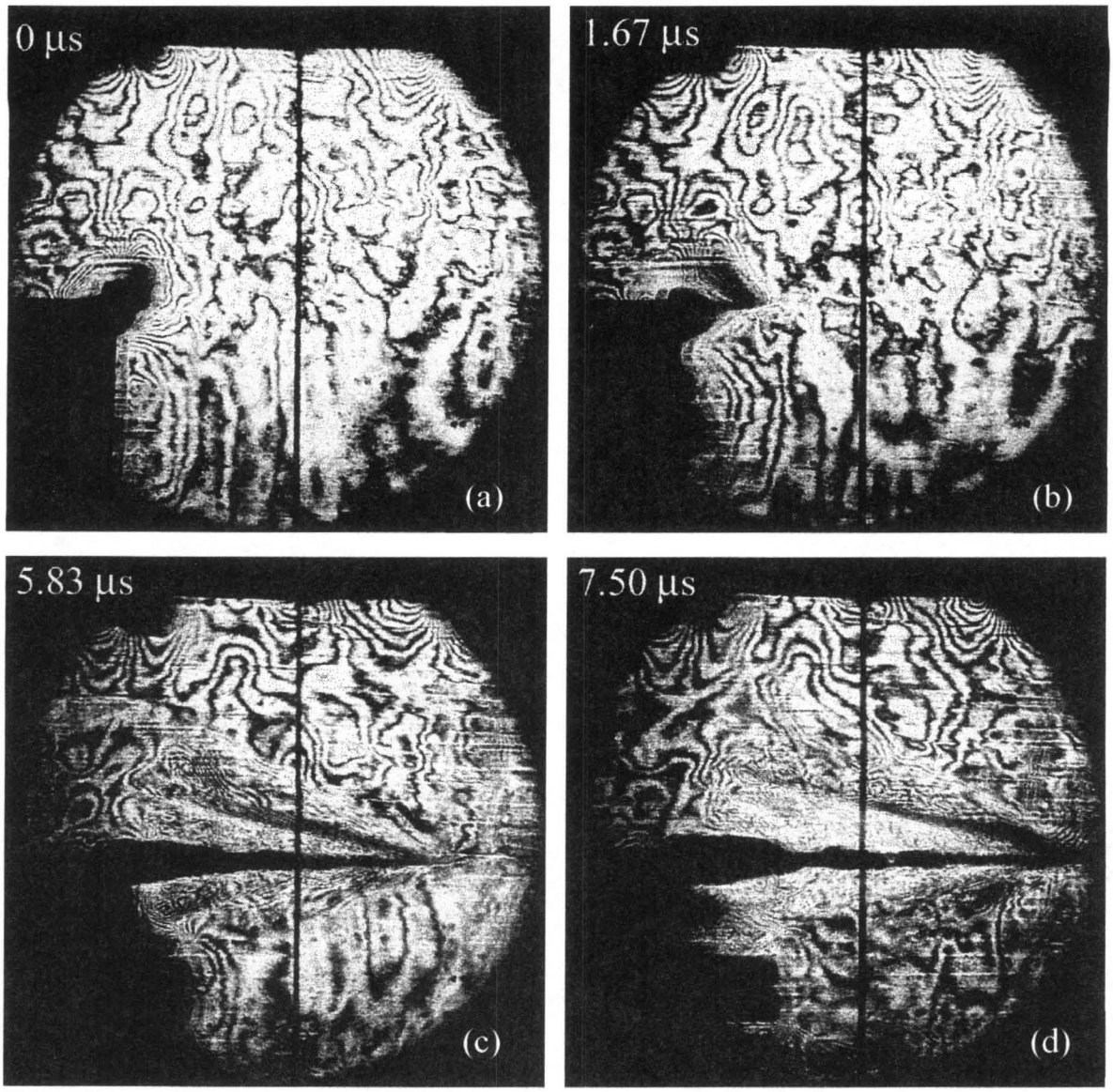

Figure 14

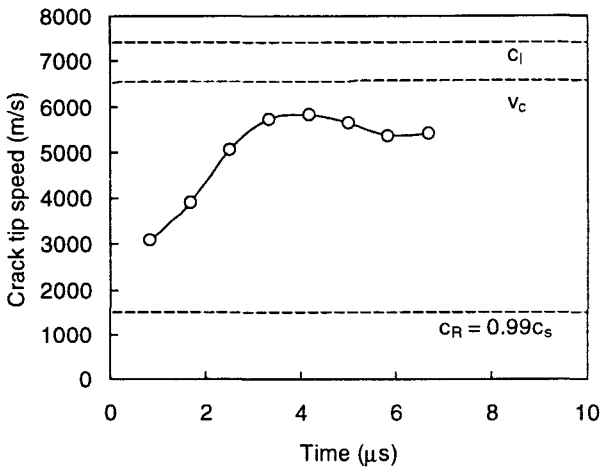
8000
7000
6000
5000
4000
3000
2000
1000
0
Crack tip speed (m/s)
0
2
4
6
8
10
Time (μs)
c_l
v_c
$c_R = 0.99c_s$

Figure 15

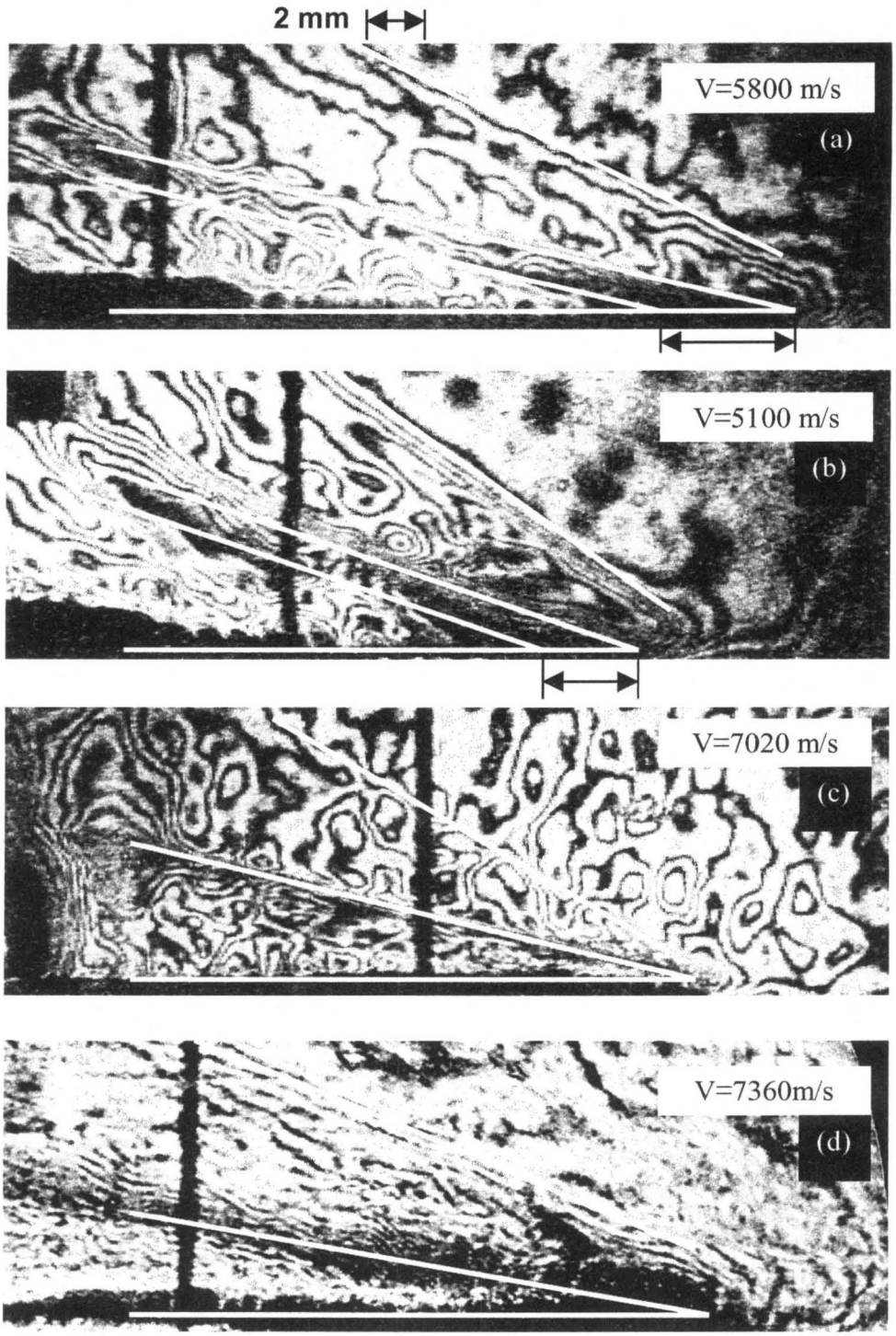

Figure 16

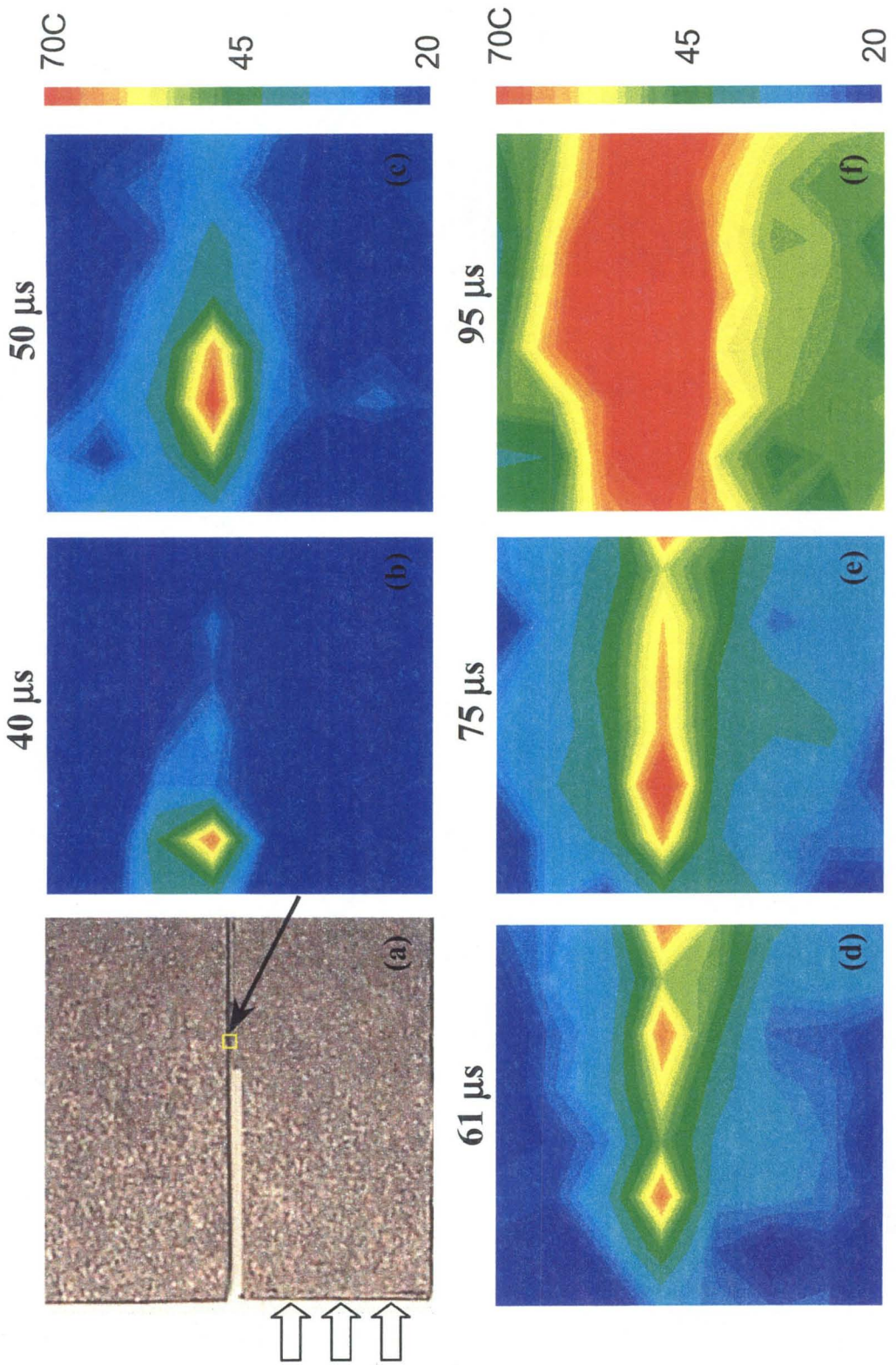

Figure 17

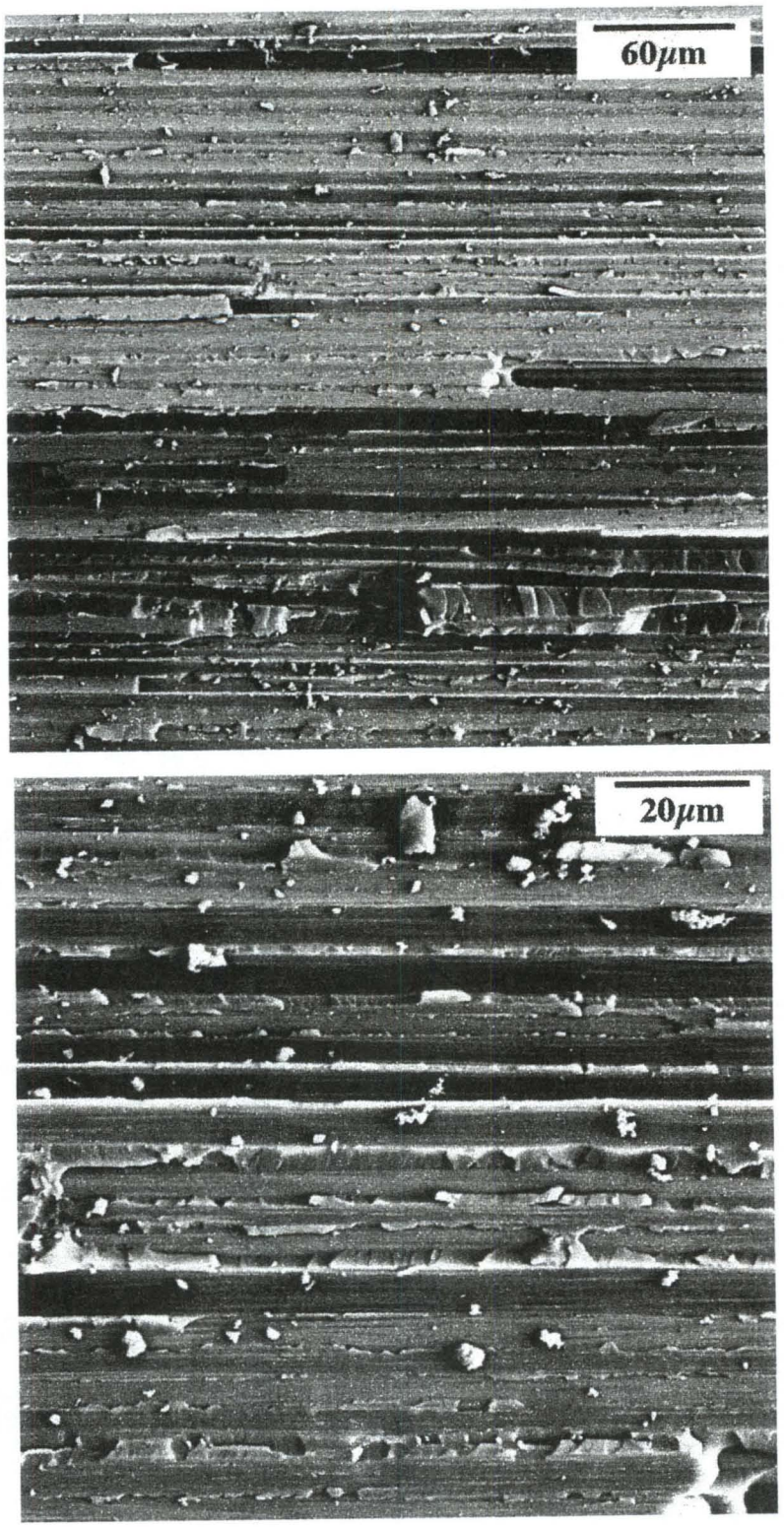

Figure 18

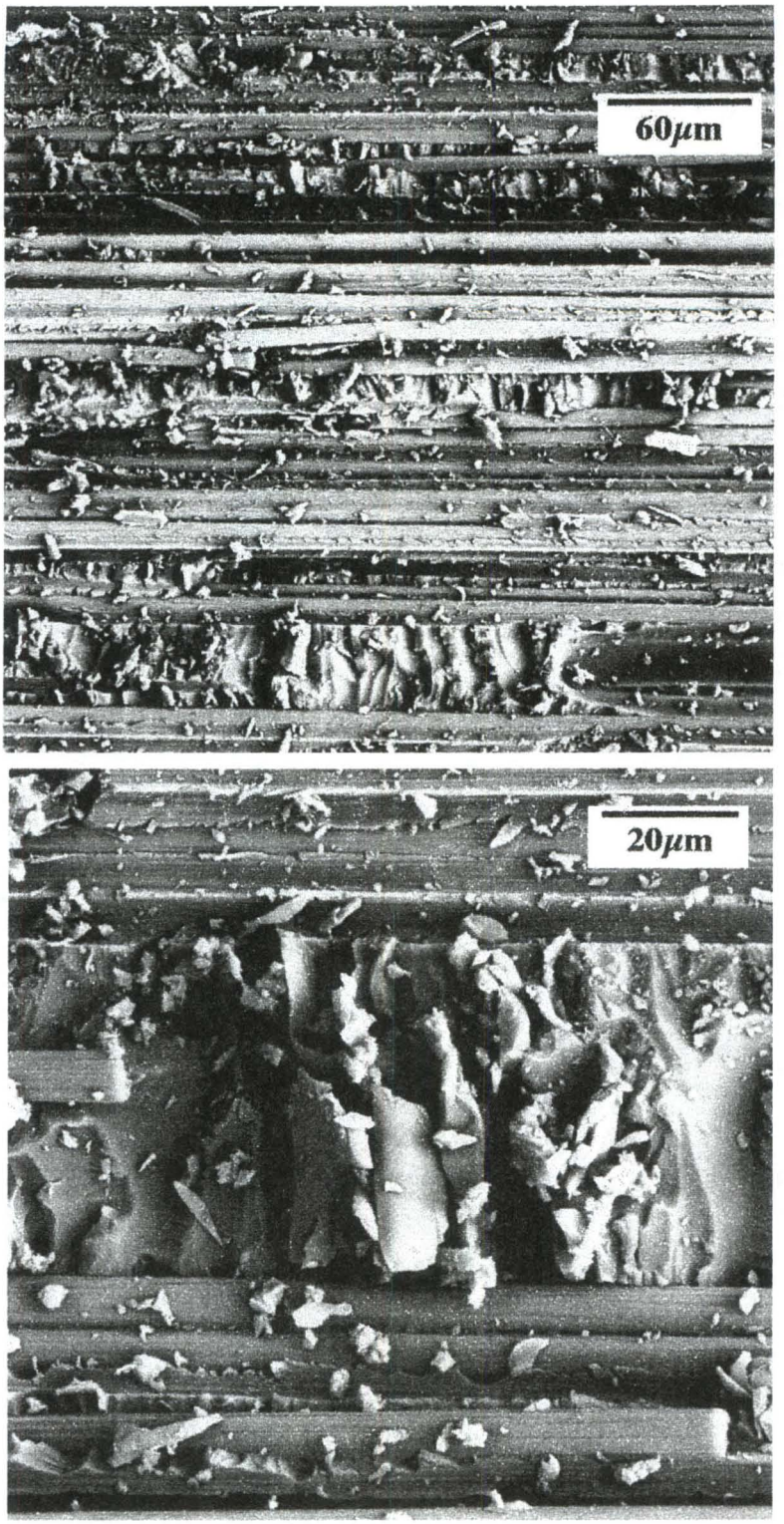

Figure 19

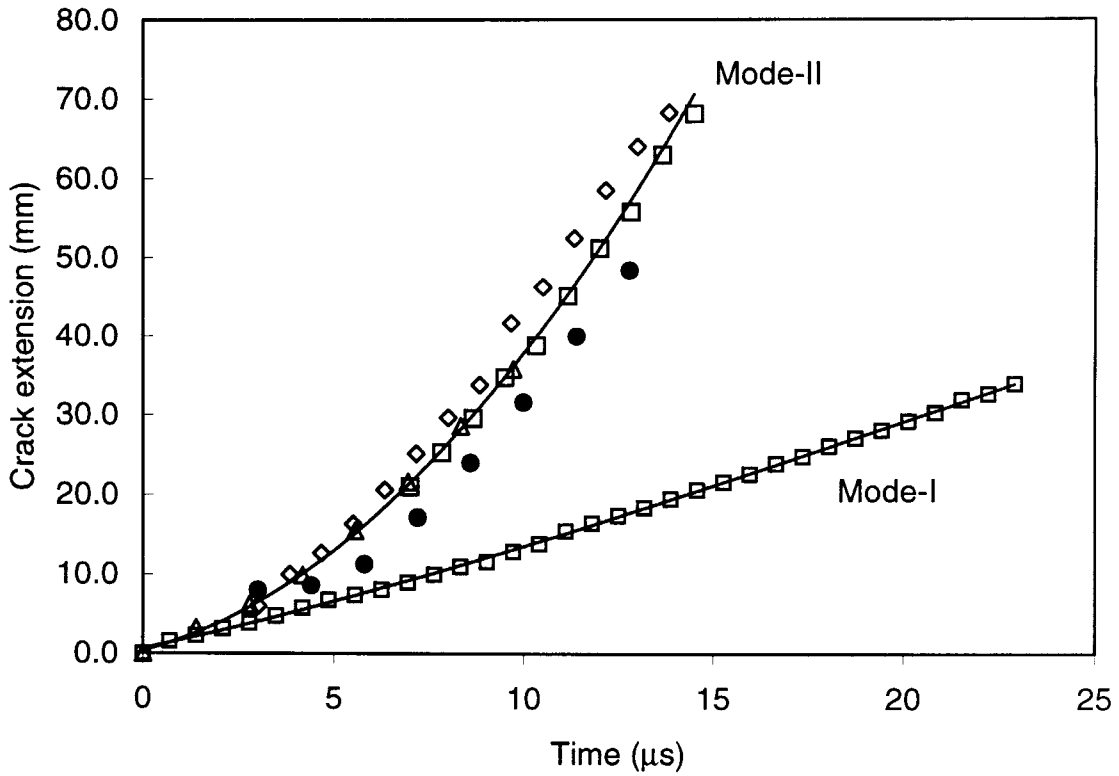
80.0
70.0
60.0
50.0
40.0
30.0
20.0
10.0
0.0
Crack extension (mm)
0
5
10
15
20
25
Time (μs)
Mode-II
Mode-I

Figure 20

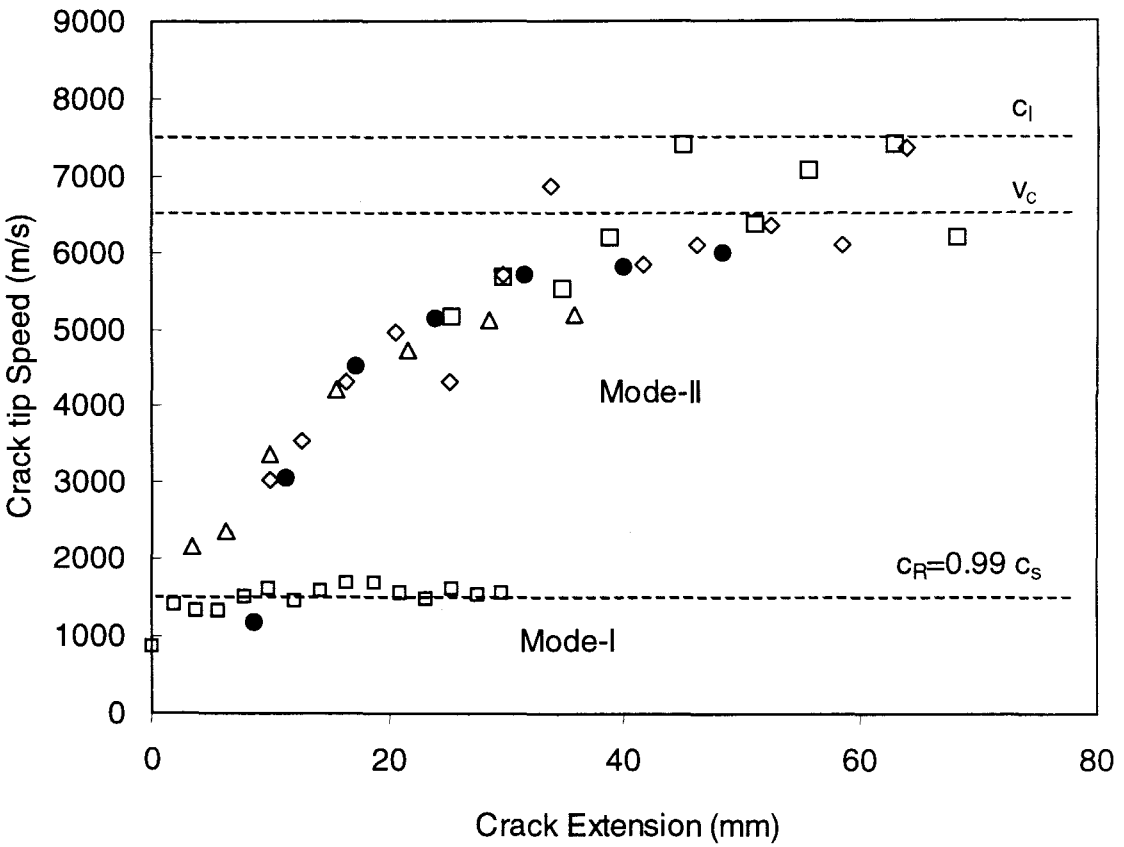
9000
8000
7000
6000
5000
4000
3000
2000
1000
0
Crack tip Speed (m/s)
0
20
40
60
80
Crack Extension (mm)
c_l
v_c
Mode-II
c_R=0.99 c_s
Mode-I

Figure 21

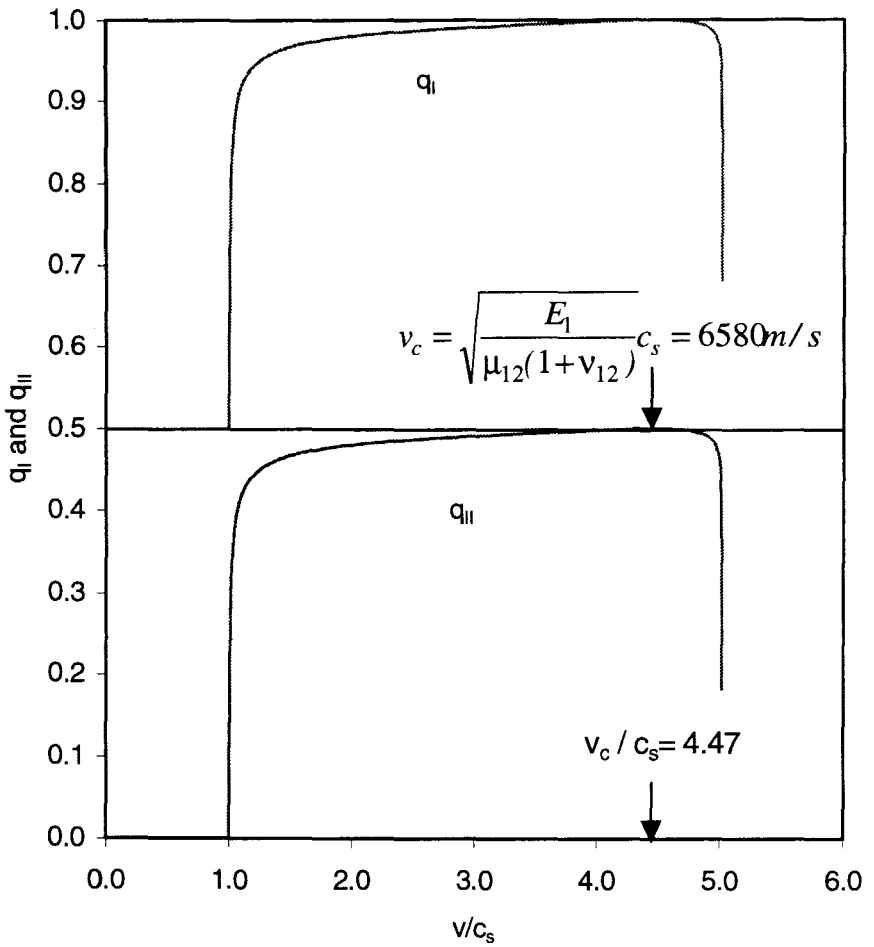
1.0
0.9
0.8
0.7
0.6
0.5
0.4
0.3
0.2
0.1
0.0
q_I and q_{II}
q_I
$v_c = \sqrt{\frac{E_1}{\mu_{12}(1+\nu_{12})}} c_s = 6580 m/s$
q_{II}
$v_c / c_s = 4.47$
0.0
1.0
2.0
3.0
4.0
5.0
6.0
v/c_s

Figure 22

Chapter 2

Dynamic Fracture of Unidirectional Composite Materials: Mode-I Crack Initiation and Propagation

ABSTRACT

An experimental study of mode-I dynamic crack initiation and propagation in fiber-reinforced unidirectional graphite/epoxy composite plates is presented in this paper. Single-edge notched specimens were dynamically loaded in mode-I by impacting with a steel projectile opposite the machined notch at moderate impact speeds of up to 57 m/s. The crack-tip location and the dynamic stress intensity factor were obtained from full-field measurements in real-time using a high-speed camera in conjunction with coherent gradient sensing (CGS) optical interferometry. The dependence of the dynamic initiation fracture toughness on the loading rate was determined and was found to be constant for low loading rates and to increase rapidly above $\dot{K}_I^d > 10^5$, consistent with observed trends in homogeneous isotropic materials. Cracks propagated along the fibers either in the matrix or the fiber/matrix interface, and accelerated to various steady state speeds less than the Rayleigh wave speed of the composite depending on the initial loading. The dynamic crack propagation toughness, K_{ID}, was measured as a function of crack tip speed and was observed to decrease with crack tip speed up to the Rayleigh wave speed of the composite.

1 INTRODUCTION

Due to the nature of typical composite material applications such as turbine fan blades, marine hull structures and tank armors, most of the damage incurred by composites is impact induced. Impact loading results in dynamic failure along the weak interfaces that are inherent in composite materials. Thus, dynamic crack growth along weak planes becomes a significant mode of failure in composites and other layered/sandwiched structures. In order to design damage tolerant composite components, it is necessary to understand two highly dynamic events: a) the rapid loading of a stationary crack to the onset of crack growth and b) the subsequent fast crack growth of a crack.

The distinct dynamic fracture regimes of initiation and growth are very important in transient events. It has long been recognized in the literature that the *initiation* fracture toughness of structural metals (Freund, 1990; Freund, Duffy and Rosakis, 1981) and polymer materials (Ravi-Chandar and Knauss, 1984a) are highly dependent on the rate of loading and may be drastically different from the quasi-static initiation fracture toughness. Thus, in general, the crack initiation toughness is a material dependent function of loading rate. Analogously, the toughness of a dynamically *growing* crack is often a strong function of the crack tip speed because the speed determines the local strain rate in the region directly ahead of the propagating crack. The dependence of toughness on crack tip speed for a given material also dictates the conditions for crack arrest, such as maximum crack arrest lengths. However, very few studies have been conducted which address dynamic crack growth. Some of the first studies of this nature in structural metals were conducted by Rosakis, Duffy and Freund (1984) and Zehnder

and Rosakis (1990), whereas dynamic propagation studies on polymers have been discussed by Dally (1979).

Detailed experimental studies of either quasi-static or dynamic crack propagation in fiber-reinforced composites are few in literature. Liu et al. (1998a) investigated quasi-static fracture of polymer composites using the optical technique of CGS interferometry. Khanna and Shukla (1994) extended the theoretical model of Piva and Viola (1988) and used it to analyze measurements from strain gages and to determine mode-I dynamic stress intensity factors for cracks propagating in unidirectional glass-epoxy composite laminates at constant crack-tip speed. Lambros and Rosakis (1997), using CGS interferometry in conjunction with high-speed photography, looked at the initiation and growth in thick unidirectional graphite-epoxy composite plates under symmetric one point impact loading. They observed crack tip speeds for mode-I loading which approached $0.5c_R$, where c_R is the speed of the Rayleigh surface waves travelling in the direction of the fibers of a half space (one major direction of anisotropy). Finally, Liu et al. (1998a), also used CGS and high-speed photography to investigate the dependence of the mode-I dynamic fracture toughness on crack growth.

In this paper, we present the first extensive experimental results pertaining to both mode-I fracture initiation and propagation under dynamic loading. The main differences between this investigation and dynamic fracture investigations on isotropic materials are that 1) the material is orthotropic, and 2) the material has weak planes in the fiber direction along which the crack is constrained to move. The orthotropic nature of the material will

influence the near-tip mechanical field and hence, how the stress intensity factor is calculated. In addition, we expect that the existence of a weak plane parallel to the fibers will make the propagation behavior distinct from other homogeneous isotropic materials. We used the full-field optical technique of CGS in conjunction with high-speed photography to enable qualitative characterization of the highly transient processes. Stress intensity factors were calculated from the CGS fringe patterns for both stationary and propagating cracks. Crack-tip speed histories were then computed for propagating cracks from the interferograms and the limiting crack tip speeds were thus determined.

In the next section, dynamic crack initiation and dynamic crack growth criteria are reviewed. The equations for a stationary and a propagating crack in an orthotropic material are then given. After describing the material and the experimental procedure, the experimental results on the dependence of dynamic crack initiation toughness on loading rate are presented. This section is followed by the results of the dynamic crack propagation experiments, which include steady state crack tip speeds and propagation toughness for mode-I cracks.

2 BACKGROUND

2.1 The dynamic initiation criterion – effect of loading rate

Let a body with an initial crack of length a_o be loaded monotonically by P(t) until crack initiates at a critical load P_o corresponding to time t_o. For linear elastic materials under small-scale yielding conditions, failure is associated with the attainment of a critical value of the stress intensity factor at a time t_o called the fracture toughness, i.e.,

$K_I(P(t),a_o) = K_{IC}$. The value K_{IC} is a material property and is independent of geometry. However, when the loading rate is high, it has been observed that this critical value depends on the local, near-tip strain rate (Freund, Duffy and Rosakis, 1981; Freund, 1990). A measure of the strain rate around the crack-tip can be represented by the amplitude of the strain field, which, for small scale yielding, is the stress intensity factor. Thus, when a body with a crack a_o is being loaded dynamically with time, the crack will start growing at time t_o if the following criterion is satisfied:

$$K_I^d(P(t),a_o) = K_{IC}^D(\dot{K}_I^d(t)) \text{ at } t=t_o. \quad (1)$$

This rate dependence reflects local nonlinear deformation processes at the crack tip, such as material nonlinear behavior. It also encompasses the inertia effects on the rate dependent process of crack growth through mechanisms such as void nucleation, growth and coalescence in the case of ductile materials, and microcrack formation in the case of brittle materials. In the above equation, the left-hand side is the instantaneous value of the stress intensity factor, whereas the right hand side represents the dynamic fracture toughness at which the crack initiates at the corresponding loading rate at time $t=t_o$. The stress intensity factor on the right is obtained through numerical techniques for the particular geometry and dynamic loading history, whereas the particular value for the right hand side is determined from dynamic fracture experiments.

2.2 Dynamic crack growth criterion – crack tip equation of motion

When a crack initiates dynamically, it propagates with a speed that cannot be predicted by continuum mechanics alone. Here, again, we would need the notion of a dynamic crack growth toughness, which would similarly be a function of the strain rate near the

crack tip. The dynamic stress field is not only a function of the time dependent generalized loading but also the crack length and the crack-tip speed so that we have $K_I^d(P(t),a(t),\dot{a}(t),t)$.

For the crack to continue growing at a particular speed, the dynamic stress intensity factor has to maintain a specific material value, K_{ID}, called the dynamic crack growth toughness. Like the dynamic initiation toughness, the dynamic growth toughness is a material property that is also a function of the strain rate at the crack tip following the same argument as above. However, in this case the crack-tip speed is the dominant parameter that represents the strain rate effect to a first order approximation, so that the propagation criterion becomes

$$K_I^d(P(t),a(t),\dot{a}(t),t) = K_{ID}(\dot{a}(t)) \text{ at } t>t_o. \tag{2}$$

The left-hand side of this equation measures the strength of the near tip fields which drive crack propagation. The right hand side represents the resistance of the material to crack propagation, which incorporates, besides the surface energy, all nonlinear material behavior, such as plasticity and microcracking, and material inertia effects. Establishing the uniqueness and the existence of the relationship between the dynamic crack growth toughness on the crack tip speed is the main goal of this investigation besides establishing the rate dependence of the initiation fracture toughness.

2.3 Asymptotic crack tip stress fields in orthotropic solids

2.3.1 Stationary crack in an orthotropic solid

The elastic near-tip stress fields for a stationary crack in an anisotropic material were established by Stroh (1958) and by Sih, Paris and Irwin (1965). The most singular terms can be expressed in terms of the stress intensity factors in mode-I and mode-II where the stress intensity factors are defined by

$$\begin{aligned} K_I &= \lim_{x_1 \to 0^+} \sqrt{2\pi x_1}\,\sigma_{22}(x_1,0) \\ K_{II} &= \lim_{x_1 \to 0^+} \sqrt{2\pi x_1}\,\sigma_{12}(x_1,0). \end{aligned} \tag{3}$$

The explicit forms for the most singular term in the asymptotic expression for the stresses were presented by Liu et al (1998a). For a homogeneous elastic orthotropic material we can define three non-dimensional material parameters (Suo, 1990)

$$\lambda = \frac{b_{11}}{b_{22}}, \quad \rho = \frac{2b_{12} + b_{66}}{2\sqrt{b_{11}b_{22}}}, \quad \kappa = \frac{3\sqrt{b_{11}b_{22}} + b_{12}}{2\sqrt{b_{11}b_{22}} - b_{12}}, \tag{4}$$

where b_{ij}'s are components of the compliance matrix for plane stress. For any simply connected domain undergoing planar deformation with tractions prescribed on its boundary, the stresses depend only on the two nondimensional elastic parameters, λ and ρ. The use of these constants simplifies the long expressions for the asymptotic stress fields around a crack tip in an orthotropic material. For unidirectional graphite/epoxy composite material that we are using in this study, $\lambda = 0.08176$ and $\rho = 4.1$. For the case of $\rho > 1$, the most singular stress components of the asymptotic stress field are

$$\begin{aligned} \sigma_{11}(r,\theta) &= K_I f_{11}(r,\theta,\rho,\lambda) + K_{II} f_{12}(r,\theta,\rho,\lambda) \\ \sigma_{12}(r,\theta) &= K_I f_{21}(r,\theta,\rho,\lambda) + K_{II} f_{22}(r,\theta,\rho,\lambda). \end{aligned} \tag{5}$$

The angular functions, f_{ij}, are given by

$$
\begin{aligned}
f_{11} &= \frac{1}{\sqrt{2\pi}} \frac{\lambda^{-1/2}}{\rho_1 - \rho_2} \left(\rho_1 \frac{1}{\sqrt{r_1}} \cos\frac{\theta_1}{2} - \rho_2 \frac{1}{\sqrt{r_2}} \cos\frac{\theta_2}{2} \right) \\
f_{12} &= -\frac{1}{\sqrt{2\pi}} \frac{\lambda^{-1/4}}{\rho_1 - \rho_2} \left(\rho_1^2 \frac{1}{\sqrt{r_1}} \sin\frac{\theta_1}{2} - \rho_2^2 \frac{1}{\sqrt{r_2}} \sin\frac{\theta_2}{2} \right) \\
f_{21} &= -\frac{1}{\sqrt{2\pi}} \frac{1}{\rho_1 - \rho_2} \left(\rho_2 \frac{1}{\sqrt{r_1}} \cos\frac{\theta_1}{2} - \rho_1 \frac{1}{\sqrt{r_2}} \cos\frac{\theta_2}{2} \right) \\
f_{22} &= \frac{1}{\sqrt{2\pi}} \frac{1}{\lambda^{-1/4}(\rho_1 - \rho_2)} \left(\frac{1}{\sqrt{r_1}} \sin\frac{\theta_1}{2} - \frac{1}{\sqrt{r_2}} \sin\frac{\theta_2}{2} \right),
\end{aligned}
\tag{6}
$$

where

$$
\begin{aligned}
r_{1,2} &= r\sqrt{\cos^2\theta + \lambda^{-1/2}\rho_{1,2}^2 \sin^2\theta} \ , \\
\theta_{1,2} &= \tan^{-1}\left(\lambda^{-1/4}\rho_{1,2}\tan\theta\right) \\
\rho_{1,2} &= \sqrt{\frac{\rho+1}{2}} \pm \sqrt{\frac{\rho-1}{2}} \, .
\end{aligned}
\tag{7}
$$

Thus, unlike the isotropic case, the stresses are also functions of the material properties. The stresses are independent of material properties only on the crack plane, i.e., at θ=0.

The energy release rates are related to the stress intensity factors by (Sih et al., 1965; Hutchinson and Suo, 1992)

$$
\begin{aligned}
G_I &= \left(\frac{1+\rho}{2E_1E_2} \right)^{1/2} \lambda^{-1/4} K_I^2 = \lambda^{-3/4} \sqrt{\frac{1+\rho}{2}} \cdot \frac{K_I^2}{E_1} \\
G_{II} &= \left(\frac{1+\rho}{2E_1E_2} \right)^{1/2} \lambda^{1/4} K_{II}^2 = \lambda^{-1/4} \sqrt{\frac{1+\rho}{2}} \cdot \frac{K_I^2}{E_1} .
\end{aligned}
\tag{8}
$$

2.3.2 Subsonically propagating crack in an orthotropic solid

Crack tip fields of a dynamically growing crack in anisotropic elastic solids have been derived before by Wu (1989) using Stroh's formulation and Huang et al. (2001):

$$\begin{aligned}\sigma_{11}(r,\theta,\rho,\lambda,v) &= K_I f_{11}(r,\theta,\rho,\lambda,v) + K_{II} f_{12}(r,\theta,\rho,\lambda,v)\\ \sigma_{22}(r,\theta,\rho,\lambda,v) &= K_I f_{21}(r,\theta,\rho,\lambda,v) + K_{II} f_{22}(r,\theta,\rho,\lambda,v),\end{aligned} \tag{9}$$

where the angular functions, f_{ij}, are given by

$$\begin{aligned}f_{11} &= \frac{1}{\sqrt{2\pi a_3}}\left\{b_1(\mu_1)a_1(\mu_2)\frac{\cos\theta_1/2}{\sqrt{r_1}} - b_1(\mu_2)a_1(\mu_1)\frac{\cos\theta_2/2}{\sqrt{r_2}}\right\}\\ f_{12} &= \frac{1}{\sqrt{2\pi a_3 c_{66}}}\left\{-b_1(\mu_1)a_1(\mu_2)\frac{\sin\theta_1/2}{\sqrt{r_1}} + b_1(\mu_2)a_1(\mu_1)\frac{\sin\theta_2/2}{\sqrt{r_2}}\right\}\\ f_{21} &= \frac{1}{\sqrt{2\pi a_3}}\left\{-a_1(\mu_2)a_2(\mu_1)\frac{\cos\theta_1/2}{\sqrt{r_1}} + a_1(\mu_1)a_2(\mu_2)\frac{\cos\theta_2/2}{\sqrt{r_2}}\right\}\\ f_{22} &= \frac{1}{\sqrt{2\pi a_3 c_{66}}}\left\{a_2(\mu_1)a_2(\mu_2)\left(\frac{\sin\theta_1/2}{\sqrt{r_1}} - \frac{\sin\theta_2/2}{\sqrt{r_2}}\right)\right\},\end{aligned} \tag{10}$$

and the variables a_i, b_i are functions of crack tip speed and material properties as follows:

$$\begin{aligned}a_1(\mu_\alpha) &= c_{11} - \rho v^2 + \mu_\alpha^2 c_{12}\\ a_2(\mu_\alpha) &= \mu_\alpha\left\{c_{22}(c_{11} - \rho v^2 - \mu_\alpha^2 c_{66}) - c_{12}(c_{12} + c_{66})\right\}\\ b_1(\mu_\alpha) &= \mu_\alpha\left\{c_{11}c_{66} - c_{12}(\rho v^2 + \mu_\alpha^2 c_{66})\right\}\\ a_3(\mu_1,\mu_2) &= a_1(\mu_1)a_2(\mu_2) - a_1(\mu_2)a_2(\mu_1),\end{aligned} \tag{11}$$

and

$$r_\alpha = \sqrt{x_1^2 + \mu_\alpha^2 x_2^2} = r\sqrt{\cos^2\theta + \mu_\alpha^2 \sin^2\theta} \quad \text{and} \quad \theta_\alpha = \tan^{-1}\left(\mu_\alpha \frac{x_2}{x_1}\right) \tag{12}$$

$$\mu_1(v)=\sqrt{\frac{B-\sqrt{B^2-4AC}}{2A}} \qquad \text{where} \quad A=c_{22}c_{66}$$
$$\mu_2(v)=\sqrt{\frac{B+\sqrt{B^2-4AC}}{2A}} \qquad B=c_{11}c_{22}-(c_{22}+c_{66})\rho v^2-c_{12}^2-2c_{12}c_{66} \quad (13)$$
$$C=(c_{11}-\rho v^2)(c_{66}-\rho v^2).$$

The energy release rate for a subsonically growing crack is (Wu, 1989; Liu, 2001)

$$G=\frac{\alpha_s m(v)}{2_{c_{66}} R(v)}\left(\lambda^{-1/2}\alpha_l K_I^2+\alpha_s K_{II}^2\right), \quad (14)$$

with

$$\eta=\frac{c_l}{c_s},$$

$$\gamma=1+\frac{\eta^2}{\lambda^{-1/2}}\left(\frac{3-k}{1+k}\right),$$

$$s(v)=\frac{\alpha_l^2(v)\eta^4\lambda-\gamma^2+\alpha_s^2(v)}{2\alpha_1(v)\alpha_s(v)\eta^2\sqrt{\lambda}},$$

$$\zeta(v)=\frac{\alpha_l(v)\alpha_s(v)}{\sqrt{\lambda}},$$

$$m(v)=\frac{\eta^2}{\lambda^{-3/4}}\frac{\sqrt{2}}{\sqrt{\alpha_l(v)\alpha_s(v)}}\sqrt{\left(1+\frac{\alpha_l^2(v)\eta^4\lambda-\gamma^2+\alpha_s^2(v)}{2\alpha_1(v)\alpha_s(v)\eta^2\sqrt{\lambda}}\right)},$$

$$R(v)=\frac{\eta^4}{\lambda^{-3/2}}\left\{\alpha_l\alpha_s-\left(\frac{3-k}{1+k}\right)^2\frac{\alpha_s}{\alpha_l}-\frac{\lambda^{-1/2}(1-\alpha_s^2}{\eta^2}\right\}.$$

3 EXPERIMENTAL PROCEDURE

3.1 Material and homogenized material properties

A cross-section of the composite material is shown in figure 1. The fiber reinforced unidirectional graphite/epoxy composite plates were manufactured by Composite Mirror

Applications, Arizona, from 48 layers of graphite fiber and epoxy matrix pre-pregs laid up in the thickness direction to form a 6.3-mm thick plate. The fiber diameter was 7.3 μm and the volume fraction of the fiber in the pre-preg was 60-65%. The surface on one side of the composite plate was made optically flat by adding a thin layer of epoxy on one surface and then curing the composite specimen upon an optically flat glass plate. This surface was then made specularly reflective by coating it with a thin layer of aluminum of 1-2 μm thickness in a vacuum deposition chamber. The glass transition temperature of epoxy matrix was 132 C (270° F). The Poisson's ratio for matrix was 0.3 and for the fiber was 0.2.

The orientation of an orthonormal coordinate set with respect to the composite plate is shown in figure 1. The x_1-axis is defined to lie along the fibers, the x_3-axis is perpendicular to the plane of the composite surface (with an outward pointing unit vector), while the x_2-axis is perpendicular to the x_1-x_3 plane. If we assume the fibers are randomly distributed in the epoxy matrix, then the x_2-x_3 plane can be taken as a plane of isotropy and, macroscopically, the material may then be considered a transversely isotropic material. The stiffness matrix for a transversely isotropic matrix consists of five independent parameters: c_{11}, c_{22}, c_{12}, c_{23}, and c_{66}. These parameters are related to the easily measurable mechanical moduli E_1, E_2, μ_{23}, μ_{12}, and ν_{12} (Coker and Rosakis, 2001).

The transversely isotropic elastic constants and the stiffness matrix for our graphite/epoxy unidirectional composite material are given in table 1. The reduced stiffness matrix for plane stress cases is also shown in table 1.

The shear modulus, μ_{12}, was determined by quasi-static Iosipescu shear tests while uniaxial compression tests were conducted on an MTS hydraulic testing machine to determine Young's moduli, E_1, E_2, and the Poisson's ratio, υ_{12}. The calculated values for the stiffness components c_{11}, c_{22} and c_{66} were also verified with those obtained from the plane strain longitudinal and shear wave speeds in the direction of the major axes through the following relations:

$$c_l^{\parallel} = \sqrt{\frac{c_{11}}{\rho}}, c_l^{\perp} = \sqrt{\frac{c_{22}}{\rho}}, \text{ and } c_s = \sqrt{\frac{c_{66}}{\rho}}, \tag{15}$$

where $c_l^{\parallel}$ denotes the dilatational wave speed parallel to the fibers while $c_l^{\perp}$ denotes the dilatational wave speed perpendicular to the fibers, and c_s is the shear wave speed. The mass density of the composite plate was 1478 kg/m^3. The longitudinal wave speeds perpendicular and parallel to the fibers and the shear wave speed were obtained using ultrasonic pressure and shear transducers operating at a frequency of 5 MHz. These wave speeds are shown in table 2. It was noticed that significant deterioration in material properties of the composite material took place within a one-year period. The wave speed measurements carried out on virgin specimens a year before the experiments were conducted resulted in 30% higher wave speeds than the wave speeds obtained a year later. This change is attributed to humidity and temperature effects on the composite degrading the fiber/matrix interface during the time the specimens were left sitting on the shelf. The wave speeds reported in table 2 are the ones measured just before the fracture experiments were conducted. Also shown are the plane stress longitudinal wave speeds obtained by replacing c_{ij} by the plane stress stiffness matrix c_{ij}' given in table 1. The bar

wave speed in the graphite fiber was 11230 m/s (as reported by the manufacturer) and the dilatational wave speed in epoxy was measured to be 2500 m/s. The final row of table 2 shows the speed, $c_R^{\parallel}$, of Rayleigh waves propagating along the x_1 direction (parallel to the fibers) on the surface of an anisotropic half space and is obtained as the real root, $v = c_R^{\parallel}$, of the equation (Ting, 1996):

$$\left(\frac{c'_{11}c'_{22} - c'^2_{12}}{c'_{22}c'_{66}} - \frac{\rho v^2}{c'_{66}}\right)\sqrt{\frac{c'_{22}}{c'_{11}}\left(1 - \frac{\rho v^2}{c'_{66}}\right)} - \frac{\rho v^2}{c'_{66}}\sqrt{1 - \frac{\rho v^2}{c'_{11}}} = 0 . \qquad (16)$$

For the properties of our material, $c_R^{\parallel} = 0.99\, c_s$.

3.2 Specimen and loading geometry

Two types of specimens and two types of loading geometries were used for crack initiation and propagation experiments. For crack initiation experiments at low loading rates two sizes of a three-point single-edge notched bend (SENB) specimen were used in an MTS servohydraulic machine as shown in figure 2. The smaller size was 40 mm by 20 mm and the stress intensity factor was determined from boundary load measurements (figure 2a). The second geometry was a single edge notch specimen of 127 mm in width and 203 mm in height (figure 2b). The fibers were parallel to the shorter edge of the specimens. A notch of 1.5 mm width and 5 and 25 mm in length for the small and large specimens, respectively, were machined parallel to the fibers using a diamond saw.

For high-loading rate dynamic crack initiation and crack propagation experiments, the larger SEN specimens were used and subjected to impact loading with a cylindrical projectile (figure 3). As shown in the figure, the loading was symmetric to achieve

mode-I and a gas gun was used to propel the projectile. At the point of impact, a steel tab was glued to the composite to ensure uniform loading and to prevent crushing of the composite at the impact point. The loading rate was varied by changing the impact speed of the projectile. Moderate impact speeds of up to 57 m/s were used. The projectile used was either steel or polycarbonate, the latter of which allowed higher impact speeds for the same pressure. During the impact experiments, cracks initiated from the blunt notch. The blunted initial notch allowed more strain energy to be stored prior to the generation of the dynamically growing crack and thus controlled (to a certain degree) the initiation crack tip speed.

3.3 Dynamic fracture experiments and coherent gradient sensing technique

A schematic of the dynamic crack propagation experimental setup and of the optical technique of coherent gradient sensing, CGS, is shown in figure 4. The specimen was subjected to impact loading through a projectile fired from a gas gun. The projectile was 75 mm long, 50 mm in diameter and was made of hardened steel. A steel piece was bonded to the specimen at the impact site to prevent crushing of the composite plate during impact and to induce a planar loading wave front. The projectile speed was varied 10 to 57 m/s.

The dynamic stress field produced by the impact loading wave leads to a time varying out-of-plane displacement field on the surface of the composite plate. The optical technique of CGS by reflection was used in conjunction with high-speed photography to record in real time the slopes of this out-of-plane deformation field. CGS is a full-field,

lateral-shearing interferometer. The details of CGS can be found in several articles (Tippur *et al.*, 1991,1991; Rosakis, 1993) and its application to crack initiation and subsonic growth in composite materials has been demonstrated before (Lambros and Rosakis, 1997, Liu, *et al.*, 1998a).

The experimental setup used a coherent, monochromatic, collimated laser beam of 50-mm diameter which was incident on the specimen and was reflected from the initially optically flat and specularly reflective surface. Subsequently, the reflected beam acquired an optical path difference due to the nonuniform specimen surface deformations generated near the crack tip after impact. The reflected beam passed through two high-density line diffraction gratings G_1 and G_2 of pitch p = 0.0254 mm (40 lines/mm). The lines of the gratings were oriented parallel to the x_2 direction. The separation distance between these gratings is denoted by Δ and is typically 40 to 60 mm. The gratings diffracted the reflected beam and recombined it with itself to form an interferogram. The light from the gratings was collected by a filtering lens L and a diffraction spot pattern was obtained on the filtering plane, which was located at the back focal plane of the lens L. By using a filtering aperture, all but one of the ± 1 diffraction orders were blocked. One of those two remaining diffraction spots was imaged to produce an interference pattern on the image plane of a camera.

CGS, when used in reflective mode, measures the in-plane gradients of out-of-plane displacements:

$$\frac{\partial u_3}{\partial x_1} = \frac{mp}{2\Delta}, \quad m = 0, \pm 1, \pm 2, \ldots, \tag{17}$$

where $u_3(x_1,x_2)$ is the out-of-plane displacement field of the reflective surface of the specimen, p and Δ are the pitch and separation of the two high-density gratings, and m is the fringe order for the x_1 gradient contours. According to the above equation, which holds when the lines of the gratings are parallel to the x_2 direction, each CGS fringe is a locus of points that have the same slope in the x_1-direction. Under conditions of plane stress, $u_3(x_1,x_2)$ is related to the thickness averages of the stresses as follows (see Lambros and Rosakis, 1997 and Liu et al., 1998a):

$$u_3 = \frac{h}{2}\,(b_{31}\sigma_{11} + b_{32}\sigma_{22}), \tag{18}$$

where h is the specimen thickness and b_{ij} are components of the compliance matrix $\underline{b}$, inverse to the stiffness matrix $\underline{c}$ in equation (1), for the particular case of plane stress state. In our case, $b_{31} = -3.124\times10^{-12}$ and $b_{32} = -4.831\times10^{-11}$.

The interference pattern was captured by a rotating mirror type high-speed camera (Cordin model 330A). The camera is capable of recording 80 frames at framing rates of up to 2 million frames per second. In the current experiments, the interframe time in the experiments varied from 0.69 - 1.39 μs and the image was recorded on 35 mm black and white film (Kodak TMAX-400). The laser used was an argon-ion laser operating at a wavelength of 514.5 nm in a pulsed mode of 8ns pulse width. The recording process of the event commenced with the impact of the projectile on a strain-gage mounted on the steel plate, leading to a sharp voltage jump, thus triggering the pulsing of the laser.

3.4 Determination of the stress intensity factor from the CGS fringes

The amount of shearing, δ, is related to the separation of the two gratings by

$$\delta \approx \Delta \frac{l}{p}, \tag{19}$$

where l is the wavelength of light, and p is the pitch of the two line diffraction gratings (in our case p= 25×10^{-3} m). In order to increase the number of fringes for our brittle material, we use a separation distance of at least 60 mm between the gratings. Thus, for our case in which the separation, Δ, is large we need to include the effect of finite shearing. In this case, a more accurate equation is the finite difference version of the CGS equations (Bruck and Rosakis, 1992, 1993):

$$\frac{u_3(x_1+\frac{\delta}{2},x_2)-u_3(x_1-\frac{\delta}{2},x_2)}{\delta}=\frac{mp}{2\Delta} \qquad m=0,\pm1,\pm2,\ldots \tag{20}$$

$$\begin{aligned} u_3(x_1+\frac{\delta}{2},x_2)&=\frac{1}{2}h\left[b_{31}\sigma_{11}^{+}+b_{32}\sigma_{22}^{+}\right] \\ u_3(x_1-\frac{\delta}{2},x_2)&=\frac{1}{2}h\left[b_{31}\sigma_{11}^{-}+b_{32}\sigma_{22}^{-}\right] \end{aligned} \tag{21}$$

where the displacements and stresses are evaluated with the origin shifted by a distance $\delta/2$ and $-\delta/2$, for superscripts "+" and "-" respectively, i.e.,

$$\sigma_{11}^{+}=\sigma_{11}(x_1+\frac{\delta}{2},x_2), \text{ and } \sigma_{11}^{-}=\sigma_{11}(x_1-\frac{\delta}{2},x_2) \text{ etc. .}$$

Inserting the expressions for out-of-plane displacements into the finite difference CGS equation we have

$$\frac{h}{2\delta}\left[b_{31}\left(\sigma_{11}^{+}-\sigma_{11}^{-}\right)+b_{32}\left(\sigma_{22}^{+}-\sigma_{22}^{-}\right)\right]=\frac{mp}{2\Delta} \ . \tag{22}$$

Replacing the stresses with the first term of the asymptotic expansions, we have

$$\frac{h\Delta}{\delta p}\left[K_I\left\{b_{31}\left(f_{11}^{+}-f_{11}^{-}\right)+b_{32}\left(f_{21}^{+}-f_{21}^{-}\right)\right\}+K_{II}\left\{b_{31}\left(f_{12}^{+}-f_{12}^{-}\right)+b_{32}\left(f_{22}^{+}-f_{22}^{-}\right)\right\}\right]=m(x,y). \quad (23)$$

Here, f^{+} and f^{-} are obtained from equations (5) for the stationary crack and equations (9) for the subsonically propagating crack, with x_1 replaced by $x_1+\delta/2$ in the expression for f^{+} and $x_1-\delta/2$ in the expression for f^{-}. Finally, we have linear equations in terms of mode-I and mode-II stress intensity factors:

$$K_I a_1 + K_{II} a_2 = m(x,y), \quad (24)$$

where

$$\begin{aligned} a_1 &= \frac{h\Delta}{\delta p}\left\{b_{31}\left(f_{11}^{+}-f_{11}^{-}\right)+b_{32}\left(f_{21}^{+}-f_{21}^{-}\right)\right\} \\ a_2 &= \frac{h\Delta}{\delta p}\left\{b_{31}\left(f_{12}^{+}-f_{12}^{-}\right)+b_{32}\left(f_{22}^{+}-f_{22}^{-}\right)\right\} \end{aligned} \quad (25)$$

From a given CGS interference fringe pattern, the fringe positions are determined and a linear least squares fitting procedure based on the above equations was used to extract K_I and K_{II}. For the purposes of this paper least squares fits were made only for K_I. K_{II} was fixed to be zero since we have symmetric loading of the crack tip.

4 DYNAMIC CRACK INITIATION

4.1 Crack initiation experiments

As described in the previous section, two types of experiments were conducted to determine initiation fracture toughness as a function of the loading rate. At quasistatic conditions and low loading rates, a fast hydraulic MTS loading frame was used to apply

loading rates up to $\dot{K}_I^d = 2\times10^3$ MPa$\sqrt{\text{m}}\text{s}^{-1}$. To impart higher loading rates of up to $\dot{K}_I^d = 10^7$ MPa$\sqrt{\text{m}}\text{s}^{-1}$, the specimen was impacted with a projectile using a gas gun.

The low loading rate experiments were conducted with a small single edge notch specimen subjected to three-point bending. The crosshead of the loading frame was driven at different speeds to change the applied loading rate on the specimen. Since the loading rate was low, the stress intensity factor was determined from the boundary loads using standard equations from the literature for our test configuration. The stress intensity solutions readily available in literature are approximations for isotropic materials. However, Suo (1990) found that an orthotropic rescaling reduces plane elasticity problems for orthotropic materials to equivalent problems for materials with cubic symmetry, which may be approximated by isotropic ones under certain conditions. This technique allows us to extract approximate solutions for fracture parameters of orthotropic materials from the isotropic solutions found in standard handbooks. For a single edge notched bend (SENB) specimen, the stress intensity factor for an isotropic material as a function of the crack length is given by

$$K_I^{\,isotropic} = \frac{P}{t\sqrt{W}} F(a/W), \tag{26}$$

where t is the specimen thickness and the function F is given by (Anderson, 1994)

$$F(a/W) = 3\frac{S}{W}\sqrt{\frac{a}{W}}\left[1.99 - \frac{a}{W}\left(1-\frac{a}{W}\right)\left(2.15 - 3.93\frac{a}{W} + 2.7\left(\frac{a}{W}\right)^2\right)\right] \Big/ 2\left(1+2\frac{a}{W}\right)\left(1-\frac{a}{W}\right)^{3/2}.$$

The stress intensity factor for the orthotropic material is given by solution for the stress intensity factor for an isotropic material multiplied by a calibration factor $Y(\rho)$ (Bao et al., 1992):

$$K_I = Y(\rho) K_I^{isotropic}, \tag{27}$$

where[1]

$$Y(\rho) = \sqrt{\frac{1+\rho}{2}}\left(1 + 0.1(\rho-1) - 0.016(\rho-1)^2 + 0.002(\rho-1)^3\right). \tag{28}$$

The function $Y(\rho)$ is accurate with an error of less than 2% for single edge notch bend specimens and is independent of crack length change. For the composite material used in this study, $\lambda = 0.08176$ and $\rho = 4.1$, we have $Y(\rho) = 1.96$.

Figure 5 shows the variation of K_I^d with time for three experiments at different loading rates determined from measured load and equations 26-28. The fracture toughness was taken as the maximum value before failure. The loading rate was determined by a linear fit to the data obtained just prior to fracture. As can be seen from the figure, the load displacement response is very close to linear which is expected of a brittle material such as graphite/epoxy composite. The list of three-point bend experiments together with the fracture toughness and the loading rate is tabulated in table 3. The fracture toughness was almost constant over the loading rates up to 26 $\text{MPa}\sqrt{\text{m}}\text{s}^{-1}$. This result is in agreement with Liu et al. (1997) where they found no rate dependence of mode-I initiation fracture toughness for $\dot{K}_I^d < 10^4$ $\text{MPa}\sqrt{\text{m}}\text{s}^{-1}$.

---

[1] In Bao et al. (1992), there is a factor of $\sqrt{(1+\rho)/2}$ missing in equation (2) of their paper.

A quasi-static test was also conducted on a larger single edge notched bend specimen using the CGS technique to determine the stress intensity factors from the near tip deformations. In this case, a 50-mm field of view around the notch tip also allowed us to follow the crack after initiation. The CGS interferograms around the notch tip are shown in figure 6. The first frame shows that just prior to crack initiation the stress concentration is increasing at the notch tip. Using the equations for a stationary crack presented before and using the least square fit of mode-I stress intensity factor to the fringe pattern we obtain loading rate of 0.011 $\mathrm{MPa}\sqrt{\mathrm{m}}\mathrm{s}^{-1}$ and a fracture toughness of 2.5 $\mathrm{MPa}\sqrt{\mathrm{m}}$, which agrees very well with the boundary value measurements.

To obtain higher loading rates, one-point bend impact experiments were conducted in conjunction with high speed photography and CGS. The list of dynamic fracture experiments that were conducted is presented in table 4. At higher loading rates the boundary loads may not correspond to the loading at the crack tip due the stress wave loading. One solution is to record the load versus time for a given geometry and determine the stress intensity factor indirectly using a finite element analysis of the geometry subjected to the measured time dependent loading. However, a more direct method is to use full-field optical techniques where the near tip parameters are scrutinized in real-time. Using equations of elastodynamics the stress field around the crack tip can be used to infer the stress intensity factor. The second method is followed here.

Figure 7 shows a sequence of high-speed interferograms for an SEN specimen impacted symmetrically from right hand side with a projectile at 10 m/s. The field of view is 50 mm. The vertical line is a streak line and is an artifact of the camera. The notch extends from the left hand side and is being loaded, as can be seen from the growing of the fringe pattern. In the second frame, the crack is just before initiation and the final frame is the first frame after the initiation of the crack and the onset of fast propagation. From the right-hand side, the incoming flexural waves can be observed. The flexural waves interfere with the near tip fringe pattern, making determination of the stress intensity factor difficult.

In figure 8(a), an enlargement of CGS interferograms around a dynamically loaded stationary crack is shown. This fringe pattern is fit by using K_I as the amplitude of the asymptotic field. Using this stress intensity factor, a second fringe pattern was generated analytically and is shown in 8(b). The general features of the fringe pattern are captured in the model in terms of the cusp in the front lobes and the shape of the fringes. For each frame up to initiation, we use this procedure to obtain the time variation of the stress intensity factor.

The dynamic stress intensity factor as a function of time of a stationary crack subjected to impact loading is shown in figure 9. The stress intensity factor monotonically increases until 7.5 μs after first loading of crack tip at which point crack initiates. The loading rate at crack initiation is obtained by taking the slope of the curve just before initiation. The maximum value of the stress intensity factor is taken as the fracture toughness at this

loading rate for this test. This procedure was repeated for all tests to obtain the relationship between the fracture toughness and loading rate.

4.2 Dynamic crack initiation criterion

Using the dynamic stress intensity factor values at initiation (called the dynamic fracture toughness) from different tests at different impact speeds we can construct the dynamic fracture toughness curve as a function of the loading rate as shown in figure 10. The data obtained for K_{IC}^{d} is over seven orders of magnitude in loading rate. It shows that under dynamic loading conditions, the values of K_{IC}^{d} increased dramatically with loading rate greater than 10^5 MPa$\sqrt{m}$/s whereas it stayed constant in the range less than 10^2 MPa$\sqrt{m}$/s. There is no data between 10^2 and 10^5 MPa$\sqrt{m}$/s and it would be useful to conduct experiments with a drop weight tower to attain these loading rates. This behavior is also seen in ductile and brittle isotropic homogeneous materials.

Figure 11 shows the same data plotted as K_{Ic}^{d} / K_{Ic}^{s} versus time to failure, t_f, where t_f is determined from the relation $\dot{K}_I^d = K_{Ic}^{d} / t_f$. Also shown in figure 11 are dynamic fracture toughness data obtained on Homalite-100 by Ravi-Chandar and Knauss (1984a) and data obtained on 2024-T3 thin aluminum sheets by Owen et al. (1998). With this data we compare dynamic fracture initiation behavior of the brittle composite with that of a ductile aluminum alloy and a relatively brittle polymer. Comparison of all the data shows that the qualitative behavior is very similar with a steep increase in dynamic fracture toughness at loading rates greater than 10^5 MPa$\sqrt{m}$/s.

The observed increase in fracture toughness in brittle materials was explained by purely elastodynamic considerations by Liu et al. (1998b). They analyzed the dynamic fracture problem by assuming the existence of a microcrack at a finite distance in front of the crack tip and they considered a criterion of a finite stress to coalesce this microcrack with the microcrack for crack initiation to occur. They found that the rise could be explained by the inability of the dynamic K-field to radiate out and establish itself fast enough at finite distances from the crack tip at these very high loading rates. The rising trend that is observed in aluminum sheets is also observed in other ductile metals. However, although the macroscopic behavior is the same, the microscopic mechanism is the inertia effects on plasticity and ductile void growth.

5 DYNAMIC CRACK GROWTH

5.1 Dynamic crack growth experiments

Growing mode-I cracks were generated by impacting the specimen symmetrically along the notch line by a cylindrical projectile at speeds varying from 10 m/s to 57 m/s (see figure 3). The specimens were impacted with different types of projectiles to increase the range of impact speeds. The three types of projectiles used were 2"-diameter steel, 1"-diameter steel and 2"-diameter polycarbonate projectiles. A list of the dynamic crack propagation experiments is shown in table 4. Also listed with the experiments are the choice of projectile and corresponding impact speed.

A selected sequence of experimental CGS interferograms corresponding to mode-I crack initiation and propagation are shown in figure 12 for the impact speed of 12 m/s. Only four out of the eighty interferograms are presented here. The first frame shows the CGS

interference fringes that developed around the notch tip just before crack initiation. In the second frame the fringe pattern is shown at the beginning of crack propagation. The shapes of the fringe patterns do not differ qualitatively between a stationary crack and a fast growing crack. However, as the crack tip speed becomes a significant portion of the Rayleigh wave speed, the fringes become noticeably elongated in the vertical direction. In addition, the fringes are squeezed backwards. The elongation of the fringes is due to the K-field in a fast growing crack. This can be seen in figure 13, where the analytically generated fringe pattern for a slow crack, figure 13(a), is compared with a crack propagating at 1400 m/s, figure 13(b), for $K_I = 2$ MPa$\sqrt{\text{m}}$. As the crack tip speed increases, the fringes elongate perpendicular to the direction of crack growth.

The time of observation is limited by the flexural waves caused by the impact entering the field of view from the right and distorting the near-tip out-of-plane displacement field substantially. In an investigation that used CGS technique on steel (Guduru et al., 2001), shearing the image perpendicular to the crack direction and the loading wave direction was shown to be successful in eliminating the out-of-plane displacement gradient distortions caused by the flexural waves. However, in the case of composite materials, this arrangement made the undulations due to the fibers more visible and was thus disregarded.

5.2 Crack tip speed

Using the entire sequence of pictures obtained from a given experiment, the crack tip history was determined (figure 14a) for Mode-I symmetric loading. The crack tip speed as a function of crack length was then obtained by differentiation of crack tip history by

using a sectional, quadratic, three-point fit to the crack length history and is shown in figure 14b. Results are shown for different impact speeds with different projectiles (see table 4). The crack rapidly accelerates in each case to a steady state velocity, which apparently depends on a combination of impact speed and projectile type (steel or polycarbonate).

In all cases, the cracks rapidly accelerate to a steady state speed which increases with impact speed but always stays less than $c_R^{\parallel}$. Different impact speeds give rise to different steady state crack tip speed. For the case of impact speed of 57 m/s with a steel projectile, the crack was found to grow initially at 1350 m/s, within the time resolution of the high-speed camera, and then accelerated to the Rayleigh wave speed, $c_R^{\parallel}$, of the composite in the direction of the fibers ($c_R^{\parallel}$ = 1548 m/s). If one regards the small oscillations in the calculated crack tip speeds as experimental error, the crack tip speed does not exceed the Rayleigh wave speed. The fact that mode-I cracks reach steady state levels very fast and that this steady state level changes with loading was also observed by Ravi-Chandar and Knauss (1984b) for homogeneous brittle materials with an upper bound of 30-40% of the Rayleigh wave speed.

5.3 Dynamic crack growth criterion

Stress intensity factors corresponding to a specific crack tip speed were determined by fitting a K-value to the CGS fringes by linear least squares method using the asymptotic stress fields for a subsonically growing crack in an orthotropic solid (equations 15-18).

The crack tip speed calculated in the previous section was used as an input for the linear regression analysis for K.

Special attention had to be paid to include in the analysis those fringes that lie in a range of validity of the two-dimensional K-field. As can be seen in figure 15, near the crack tip there is a growing wedge shaped disturbance due to the transient nature of crack growth, changing the fringe shape in that area. Thus, data behind the crack tip could not be used because it was affected by the disturbance behind the crack tip. Another restriction was the presence of the three-dimensional zone close to the crack tip where the stress field deviates from plane-stress state. For homogeneous materials, this is determined to be at radial distances less than ½ the specimen thickness (Rosakis, 1993). Using this as a guideline, we neglect data very close to the crack tip.

A separate restriction on the K-dominant area is the outer region whose dimensions are defined by the extent of the information regarding the crack tip has traveled. The K-field is established by the shear waves propagating outwards from the crack tip. At a particular time, t_1, the fringes a distance $c_s(t_1-t_o)$ away do not receive information about the crack tip at t_1, but instead carry the information regarding the crack tip at an earlier stage, t_o. For slow moving cracks with respect to the shear wave speeds the two cracks are coincident at short times and their fringe patterns are identical. However, fast moving cracks are separated by a measurable distance in a short amount of time. Thus, the fringes correspond to the current crack tip only close to the crack tip. This can be observed in the experimental fringes that are squeezed backwards where the center of the

fringes at the outer end corresponds to a crack tip at one interframe time before. We do not see this in the simulated fringe patterns, shown in figure 15(b), because the information regarding the crack tip is simultaneously everywhere. One way of accounting for this transient nature in homogeneous, isotropic materials is by incorporating higher order terms in the expression for the near-tip field stresses. However, since equivalently derived expressions for a crack in an orthotropic medium do not exist, the stress intensity factor was determined from fringes in an annulus around the crack tip using the first term singular fields only.

Stress-intensity factors and crack tip speeds determined for three specimens are shown in figure 16. Although there is a scatter amongst the data, a general trend of a decreasing K_{ID} with speed is apparent. Note that the K_{ID} for zero velocity, obtained by extrapolating to zero speed, is lower than the static fracture toughness value obtained in the previous section. This same trend was observed by Suetsugu *et al.* (1998) in the dynamic fracture behavior of Si_3N_4 ceramic materials. However, the decrease in K_{ID} with speed is opposite the general trend observed in homogenous materials such as metals and polymers, where instead an increase is observed.

In figure 17, the dynamic energy release rate is computed from K_{ID} using equation 18. The energy release rate seems to have a constant value independent of speed. In homogeneous materials, it is a rising function of speed. This was also observed in homogeneous isotropic materials such as glass (Sharon and Fineberg, 1999) and Si_3N_4 ceramic material (Suetsugu, 1998).

6 DISCUSSION

Once mode-I cracks initiate in homogeneous isotropic brittle materials, they reach a steady state crack growth speed rapidly (Ravichandran and Knauss, 1984b). The level of the steady state speed is dependent on the loading magnitude and is bounded by 0.4 times the Rayleigh wave speed of the material. Also under far-field loading, the energy supplied to the crack tip goes to zero as the crack tip speed approaches c_R (Freund, 1990; Broberg, 1989). This is true also of the stress intensity factor for an infinite crack in a homogeneous material. Experimentally it was determined that the fracture toughness goes up with speed in Homalite due to the extension of microcracks before asymptotically approaching infinity as the crack tip speed approaches the limiting speed. Afterwards, the crack breaks up into branches. Thus, in homogeneous, brittle materials the limiting speed is caused by the microbranching manifesting itself as a rise in the apparent fracture toughness. Similar limits for crack tip speed exists in ductile materials, however, in this case, the micromechanism for damage are due to plasticity and other dissipative mechanisms. At high speeds, the microcrack density and size around the crack tip increase, which may even lead to violate small scale yielding assumption where the region of inelasticity becomes significant compared to the region of K-dominance. Therefore, the apparent K does not represent the crack tip field, and this might be one explanation for the loss of uniqueness of the K versus speed relationship.

By employing a weak plane in an isotropic material the formation of microcracks that lead to branching is prevented. In this way, the energy dissipation mechanism for brittle materials can be neglected. Experimentally, it is found that the steady state crack tip

speed approaches c_R as the loading rate is increased (Washabaugh & Knauss, 1994). Hence, in this case, whatever the fracture toughness might be as a function of crack tip speed, the limiting crack tip speed is decided by elastodynamics, i.e., the fact that the energy supplied to the crack tip approaches zero as $v \to c_R$, thus limiting the crack tip speed for mode-I cracks to c_R. In our experiments, the weak fiber/matrix interface (as compared to the toughness of fibers) in graphite/epoxy composite material allows the mode-I crack to propagate without the effect of crack branching and, depending on the loading level, to reach speeds close to the Rayleigh wave speed of the material.

7 CONCLUDING REMARKS

Dynamic fracture experiments conducted in real time on prenotched unidirectional fiber reinforced graphite/epoxy plates indicate that Mode-I (opening cracks) may only propagate subsonically along the fibers with respect to the homogenized anisotropic material properties with an upper bound of the Rayleigh wave speed. We found that as in previous investigations where a mode-I crack is prevented from branching, that the crack rapidly approaches steady-state levels that are always below the Rayleigh wave speed of the composite, c_R. The steady-state speed depends on the impact speed and it never exceeds c_R within experimental error.

The dependence of the dynamic initiation fracture toughness on the loading rate was determined and was found to be constant for low loading rates and rapidly increasing above $\dot{K}_I^d > 10^5$, consistent with observed trends in homogeneous isotropic materials.

After initiation the crack propagates along the fibers, either in the matrix or the fiber/matrix interface accelerating to at most the Rayleigh wave speed of the composite, depending on the initial loading. Crack propagation toughness was also measured as a function of crack tip speed. It was observed that the fracture toughness, K_{ID}, decreases with crack tip speed.

In the future, a transient analysis to account for the unsteady crack tip speed for more accurate K-fits to the fringe pattern would be useful. Furthermore, it is essential that the loading should be applied such that flexural waves do not interfere with the problem. This can be accomplished either by loading the notch at the notch face with a wedge or preloading the specimen to 90% of the maximum load and then initiating the crack by impacting with a knife at the notch edge.

8 REFERENCES

Anderson, T. L., 1994. *Fracture Mechanics, Fundamentals and Applications*, Second Edition. CRC Press, New York.

Bao, G., Ho, S., Suo, Z. and Fan, B., 1992. The role of material orthotropy in fracture specimens for composites, *International Journal of Solids and Structures*, 29, 1105-1116.

Bruck, H. and Rosakis, A. J., 1992. On the sensitivity of coherent gradient sensing: I. A theoretical investigation of accuracy in fracture mechanics applications, *Optics and Lasers Engineering*, 17, 83-101.

Broberg, K. B., 1989. The near-tip field at high crack velocities, *International Journal of Fracture*, 39, 1-13.

Bruck, H. and Rosakis, A. J., 1993. On the sensitivity of coherent gradient sensing: II. An experimental investigation of accuracy in fracture mechanics applications, *Optics and Lasers Engineering*, 18, 25-51.

Coker, D. and Rosakis, A. J., 2001. Experimental observations of intersonic crack growth in asymmetrically loaded unidirectional composite plates, *Philosophical Magazine A*, 81, 571-595.

Dally, J. W., 1979. Dynamic photoelastic studies of fracture, *Experimental Mechanics*, 19, 349-367.

Freund, L. B., Duffy, J. and Rosakis, A. J. 1981. Dynamic fracture initiation in metals and preliminary results on the method of caustics for crack propagation measurements, *ASME Paper No. 81-PVP-15*.

Freund, L.B., 1990. *Dynamic Fracture Mechanics*, Cambridge University Press, New York.

Guduru, P. R., Rosakis, A. J. and Ravichandran, G., 2001. Dynamic shear bands: An investigation using high speed optical and infrared diagnostics, In preparation.

Khanna, S. K. and Shukla, A., 1994. Development of the stress field equations and determination of stress intensity factor during dynamic fracture of orthotropic composite materials, *Engineering Fracture Mechanics*, 47, 345-359.

Lambros, J. and Rosakis, A. J., 1997. Dynamic crack initiation and growth in thick unidirectional graphite/epoxy plates, *Composites Science and Technology*, 57, 55-65.

Liu, C., Huang, Y., Lavato, M. L. and Stout, M. G., 1997. Measurement of the fracture toughness of a fiber-reinforced composite using the Brazilian disk geometry, *International Journal of Fracture*, 87, 241-263.

Liu, C., Rosakis, A. J., Ellis, R. W. and Stout, M. G., 1998a. A study of the fracture behavior of unidirectional fiber-reinforced composites using coherent gradient sensing (CGS) interferometry, *International Journal of Fracture*, 90, 355-382.

Liu, C., Knauss, W. G. and Rosakis, A. J., 1998b. Loading rates and the dynamic initiation toughness in brittle solids, *International Journal of Fracture*, 90, 103-118.

Liu, C., Rosakis, A. J. and Stout, M. G., 2001. On the dynamics fracture of fiber-reinforced composites using high-speed photography and CGS interferometry, In preparation.

Owen, D. M., Zhuang, S., Rosakis, A. J. and Ravichandran, G., 1998. Experimental determination of dynamic crack initiation and propagation fracture toughness in thin aluminum sheets, *International Journal of Fracture*, 90, 153-174.

Piva, A. and Viola, E. 1988. Crack propagation in an orthotropic medium, *Engineering Fracture Mechanics*, 29, 535-48

Ravi-Chandar, K. and Knauss, W.G., 1984a. An Experimental investigation into Dynamic Fracture: I. Crack Initiation and Arrest, *International Journal of Fracture*, 25, 247-262.

Ravi-Chandar, K. and Knauss, W.G., 1984b. An Experimental investigation into Dynamic Fracture: II. Microstructural Aspects, *International Journal of Fracture*, 26, 65-80.

Rosakis, A. J., 1993. Two optical techniques sensitive to gradients of optical path difference: the method of caustics and the coherent gradient sensor (CGS), *Experimental Techniques in Fracture*, Ed. J. Epstein, VCH, New York, 327-425.

Rosakis, A. J., Duffy, J. and Freund, L. B., 1984. The determination of the dynamic fracture toughness of AISI 4340 steel by the shadow spot method, *Journal of the Mechanics and Physics of Solids*, 29, 305-326.

Sharon, E. and Fineberg, J., 1999. Confirming the continuum theory of dynamic brittle fracture for fast cracks, *Nature*, 397, 333-335.

Sih, G. C., Paris, P. C. and Irwin, G. R., 1965. On cracks in rectilinearly anisotropic bodies, *International Journal of Fracture Mechanics*, 1, 189-203.

Stroh, A. N., 1958. Dislocations and cracks in anisotropic elasticity, *Philosophical Magazine A*, 625-646.

Suetsugu, M., Shimizu, K. and Takahashi, S., 1998. Dynamic fracture behavior of ceramics at elevated temperatures by caustics, *Experimental Mechanics*, 38, 1-7.

Suo, Z., 1990. Delamination specimens for orthotropic materials, *Journal of Applied Mechanics,* 57, 627-634.

Ting, T. C. T., 1996. *Anisotropic Elasticity, Theory and Applications*, Oxford University Press, New York.

Tippur, H. V., Krishnaswamy, S. and Rosakis, A. J., 1991. Optical mapping of crack tip deformations using the method of transmission and reflection coherent gradient sensing: a study of crack tip K-dominance, *International Journal of Fracture*, 52, 91-117.

Washabaugh, P.G. and Knauss, W.G., 1994. A reconciliation of dynamic crack growth velocity and rayleigh wave speed in isotropic brittle solids, *International Journal of Fracture*, 65, 97-114.

Wu, K.-C., 1989. On the crack-tip fields of a dynamically propagating crack in an anisotropic elastic solid, *International Journal of Fracture*, 41, 253-266.

Zehnder, A. T. and Rosakis, A. J., 1990. Dynamic fracture initiation and propagation in 4340 steel under impact loading, *International Journal of Fracture*, 43, 271-285.

LIST OF TABLES

LIST OF FIGURES

Figure 10. Initiation fracture toughness as a function of loading rate for a unidirectional graphite/epoxy composite material.

Figure 11. Normalized initiation fracture toughness (or critical dynamic stress intensity factor) versus time to failure for a unidirectional graphite/epoxy composite material from this investigation, and 2024-T3 Aluminum (Owen, et al. 1997) and Homalite-100 (Ravi-Chandar & Knauss, 1984a).

Figure 12. CGS interferograms of a mode-I crack: (a) pre-initiation, (b) first recorded image after initiation, (c) crack growth at 0.90 c_R, (d) disturbance of the fringe pattern due to unsteady phenomenon.

Figure 13. Effect of crack tip speed on CGS fringe patterns in an orthotropic material: K_I = 2 MPa$\sqrt{m}$, K_{II} = 0 MPa$\sqrt{m}$: (a) stationary crack, and (b) propagating crack at v = 1400 m/s.

Figure 14. Crack tip position history (a) and crack tip speed as a function of distance (b) for mode-I cracks propagating under symmetric loading in an SEN specimen.

Figure 15. Comparison of (a) experimental and (b) analytically generated CGS fringes for a subsonically propagating mode-I crack in an orthotropic material (V= 1110 m/s).

Figure 16. Propagation fracture toughness for mode-I cracks growing along the fibers in graphite/epoxy unidirectional composite materials.

Figure 17. Dynamic energy release rate for mode-I cracks growing along the fibers in graphite/epoxy unidirectional composite materials.

Table 1: In-plane material properties of the Graphite/Epoxy unidirectional composite.

3-D Stiffness Matrix (GPa)

c_{11}	c_{22}	c_{12}	c_{23}	c_{66}	c_{44}
82	11.1	4.0	4.9	3.6	3.1

Plane Stress Stiffness Matrix (GPa)

c'_{11}	c'_{22}	c'_{12}	$c'_{66} = c_{66}$
80.5	9.0	2.2	3.6

Elastic Material Properties

E_1	$E_2 = E_3$	$\nu_{12} = \nu_{13}$	ν_{23}	$\mu_{12} = \mu_{13}$	μ_{23}
80 GPa	8.9 GPa	0.25	0.43	3.6 GPa	3.1 GPa

Table 2: Characteristic plane-strain and plane-stress wave speeds.

	5 MHz Ultrasonic transducer (Plane strain)	Plane stress
	m/s	m/s
$c_l^{\parallel}$	7450 ±100	7380
$c_l^{\perp}$	2740 ± 100	2470
c_s	1560 ± 50	1560
$c_R^{\parallel}$	1548	1548

Table 3: List of three point bend experiments to determine rate dependence of initiation fracture toughness at low loading rates.

Specimen	Crack (in)	a/W	Load (N)	$\dot{K}_I^d$ $(\mathrm{MPa}\sqrt{\mathrm{m}}\mathrm{s}^{-1})$	K_{max} $(\mathrm{MPa}\sqrt{\mathrm{m}})$
3	0.195	0.243	751.5	0.143	2.51
4	0.238	0.297	444.0	0.947	1.92
5	0.203	0.254	705.0	0.115	2.41
6	0.23	0.125	856.5	0.088	2.03
8	0.167	0.209	865.0	26.3	2.63
9	0.167	0.209	770.4	0.00133	2.35

Table 4: List of impact experiments for studying mode-I dynamic crack initiation and propagation.

Specimen ID	Impact Speed (m/s)	Loading projectile type*	Interframe time (μs)	Spacing between gratings (mm)	Initiation time (μs)	Characteristic crack tip speed† (m/s)
9701	10	1-2" steel	2.083	66	27	V_{ss} = 890
9703	12	1-2" steel	1.042	66	24	V_{ss} = 1220
9704	30	2-1" steel	0.694	80	38	V_{av} = 1050
9706	33	2-1" steel	0.694	80	40	V_{av} = 950
9705	57	2-1" steel	0.694	80	32	V_{ss} = 1560
9721-IR	63	3-2" polycarbonate	1.390	60	**	V_{ss} = 1300
9723-IR	63	3-2" polycarbonate	1.390	60	**	V_{ss} = 1350

* Loading projectile type 1 is 2" steel projectile, 2 is 1" steel projectile and 3 is 2" polycarbonate projectile (See figure 3).
** No initiation recorded. First frame of pictures initiates on a propagating crack.
† Steady state or average crack tip speeds recorded based on the long term behavior of the crack.

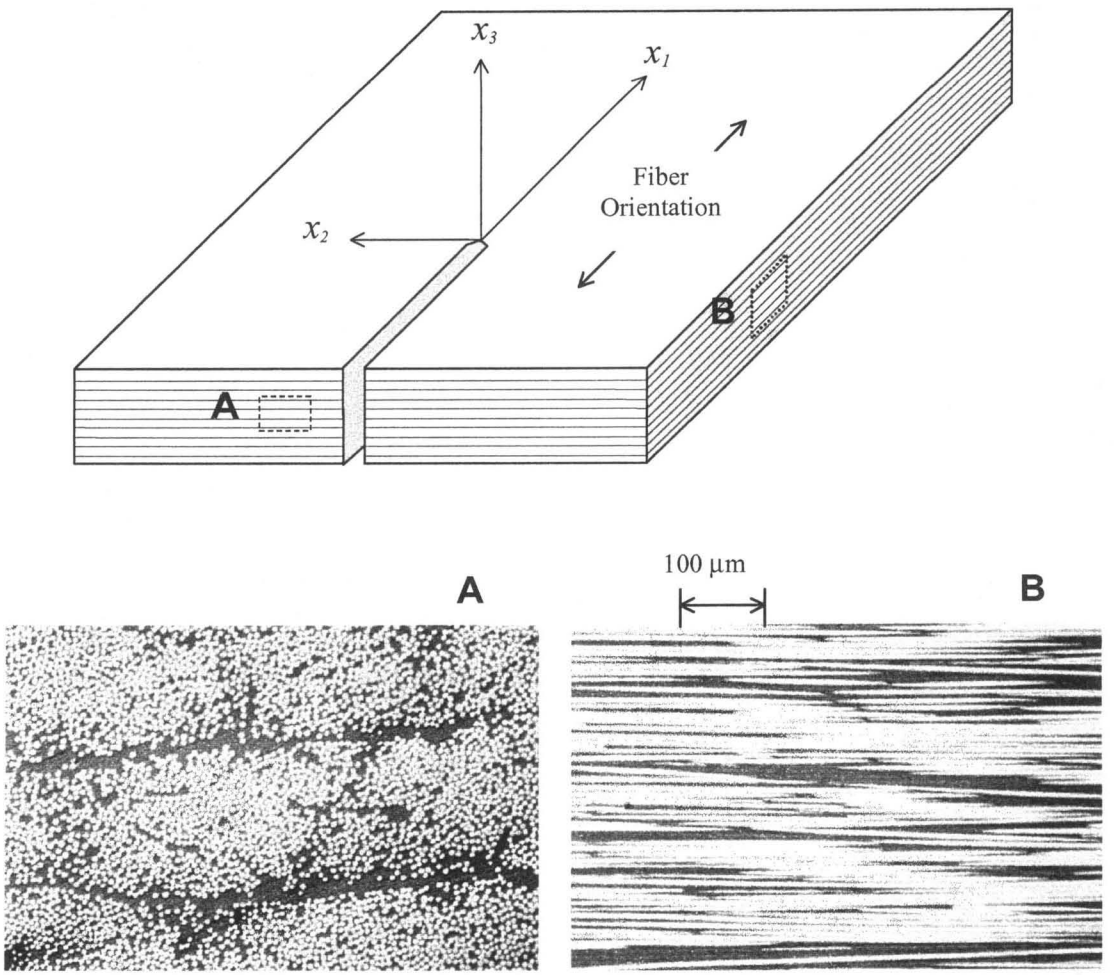

Figure 1

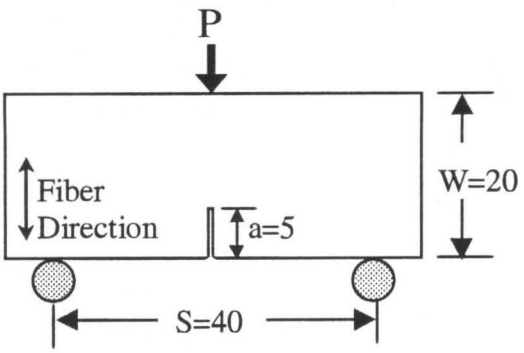
P
Fiber
Direction
a=5
W=20
S=40

(a)

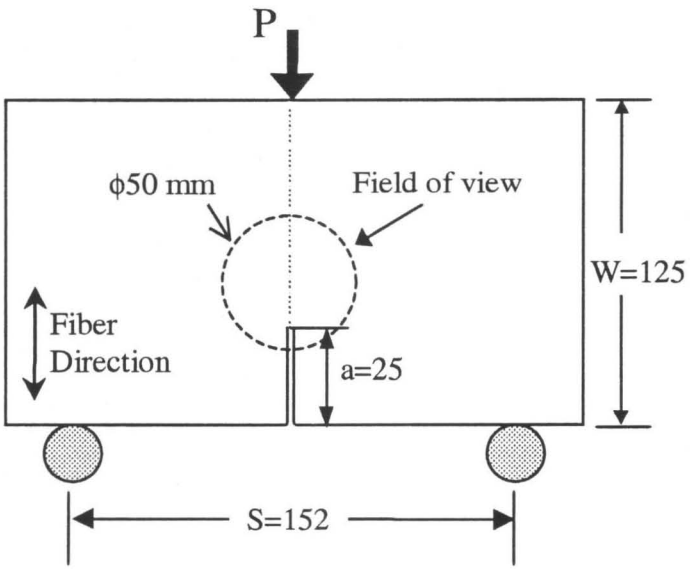
P
ϕ50 mm
Field of view
W=125
Fiber
Direction
a=25
S=152

(b)

Figure 2

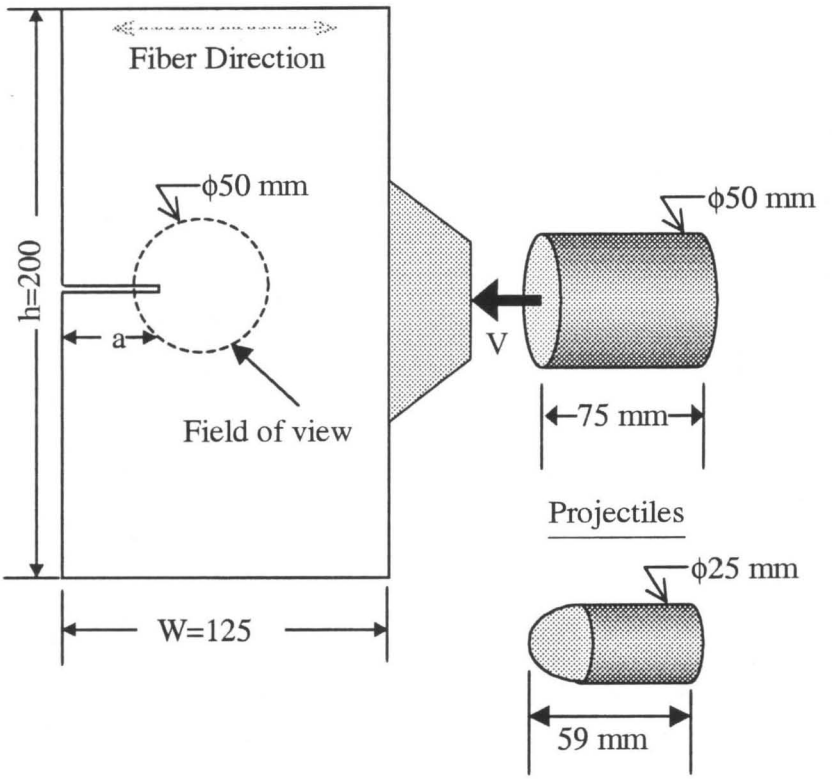
Fiber Direction
ϕ50 mm
h=200
a
Field of view
W=125
V
ϕ50 mm
75 mm
Projectiles
ϕ25 mm
59 mm

Figure 3

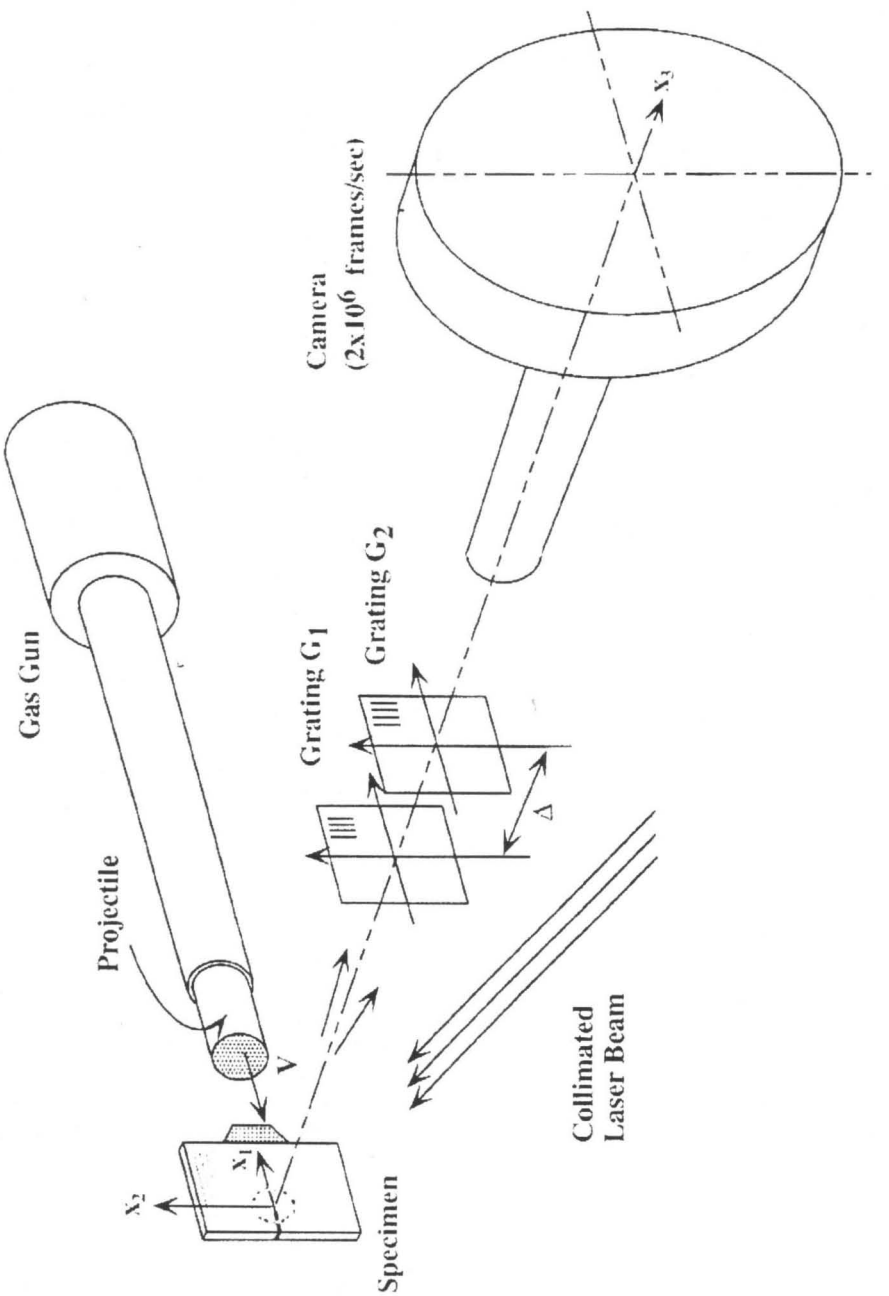
Gas Gun
Projectile
V
x_1
x_2
Specimen
Collimated
Laser Beam
Grating G_1
Grating G_2
Δ
Camera
(2x10^6 frames/sec)
x_3

Figure 4

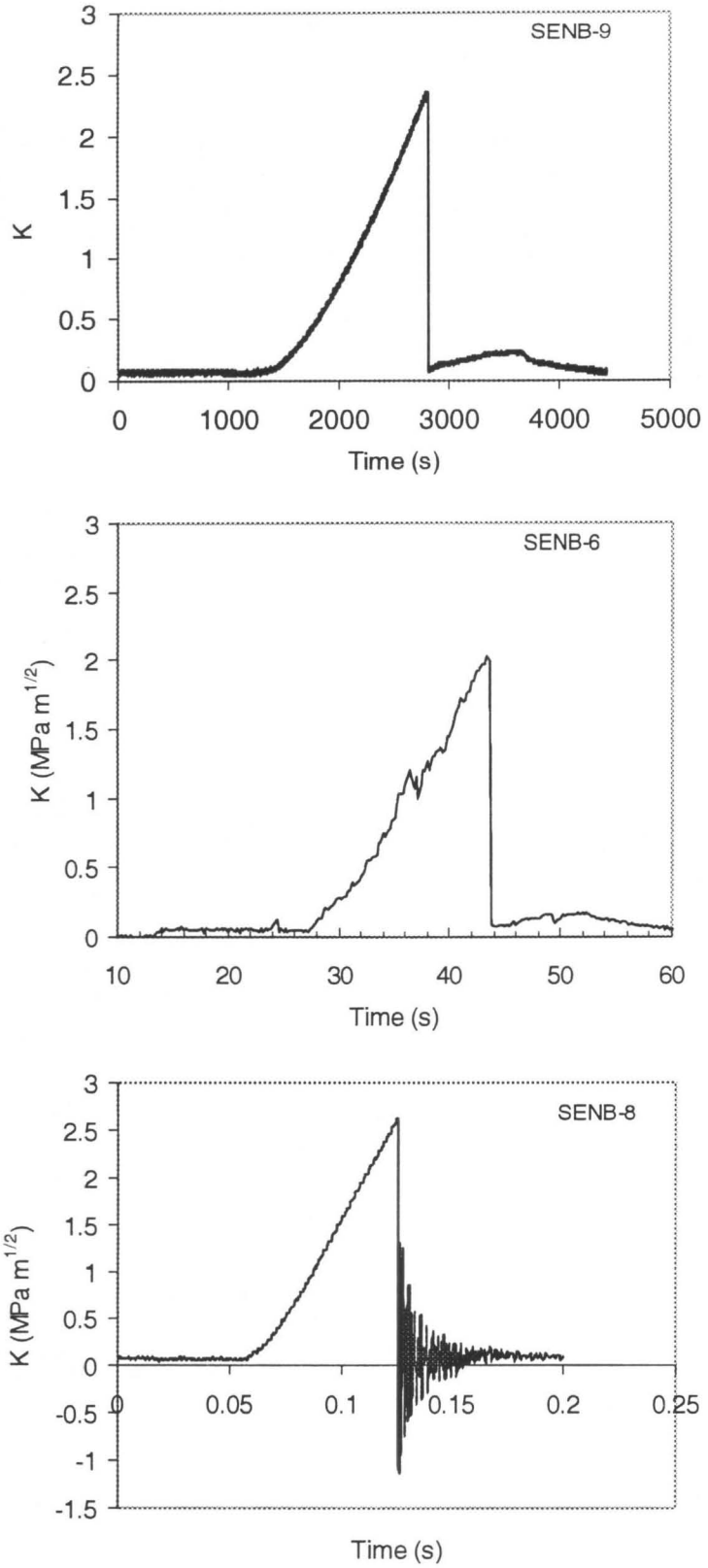

Figure 5

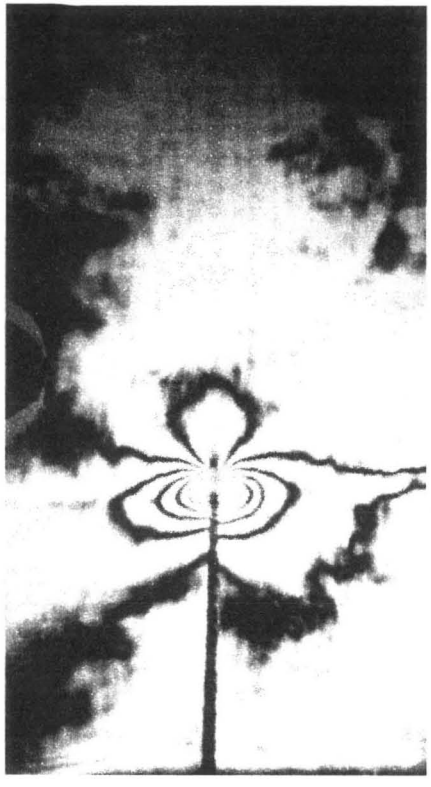

αa = 0

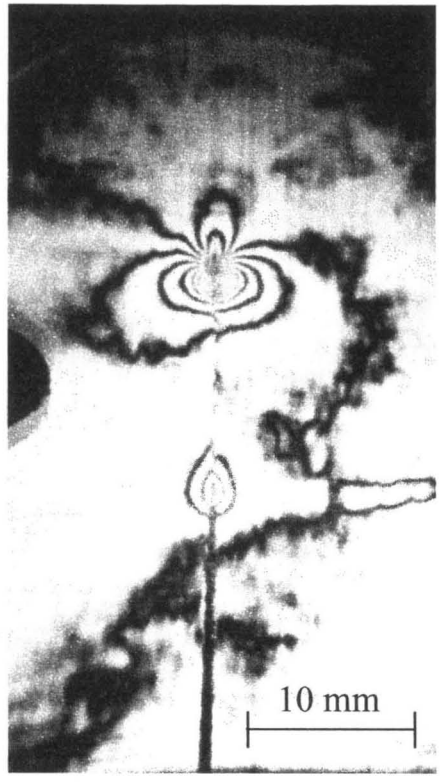

αa = 14 mm

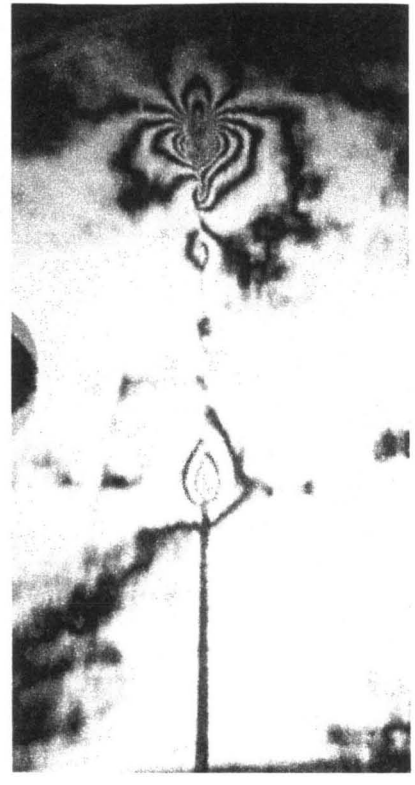

αa = 19 mm

Figure 6

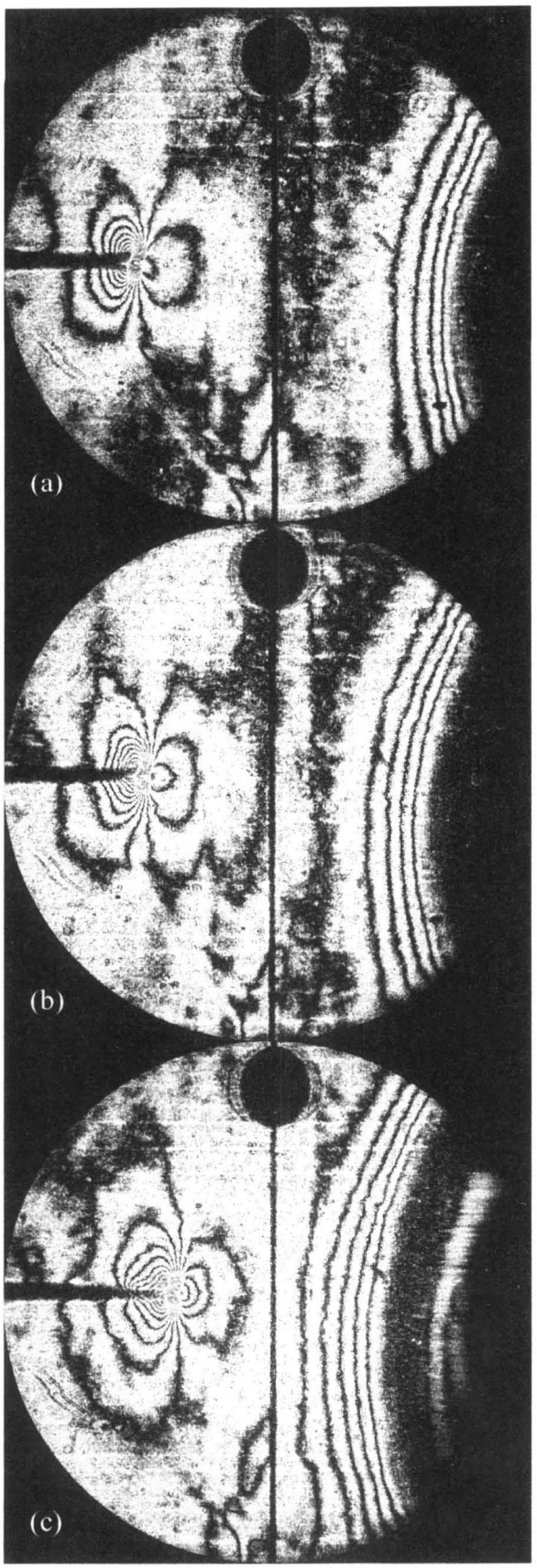

Figure 7

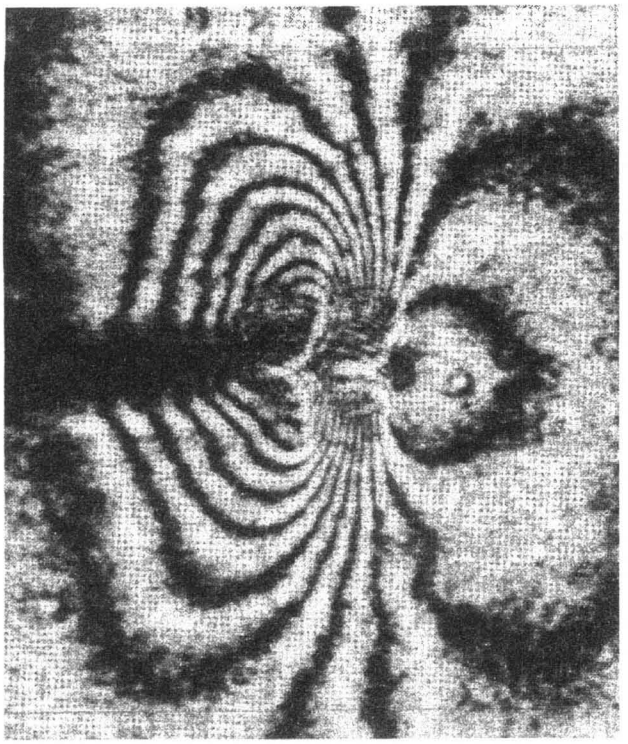

(a)

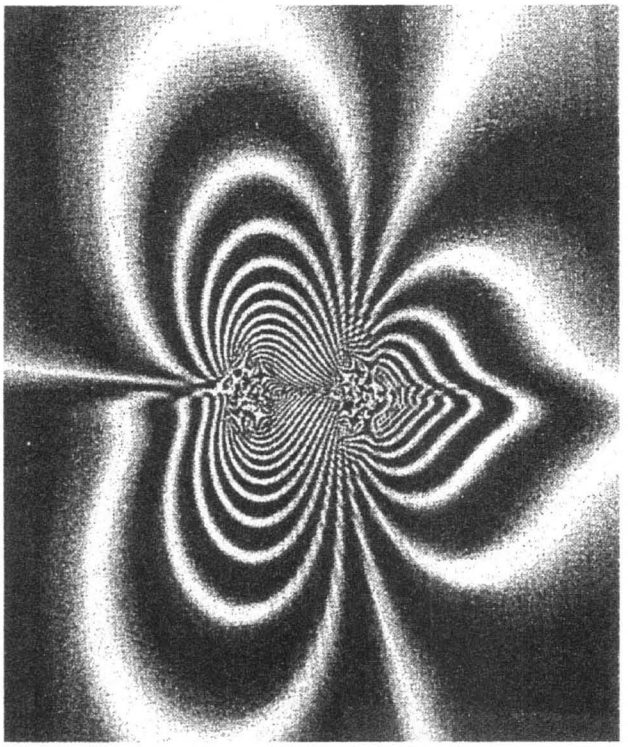

(b)

Figure 8

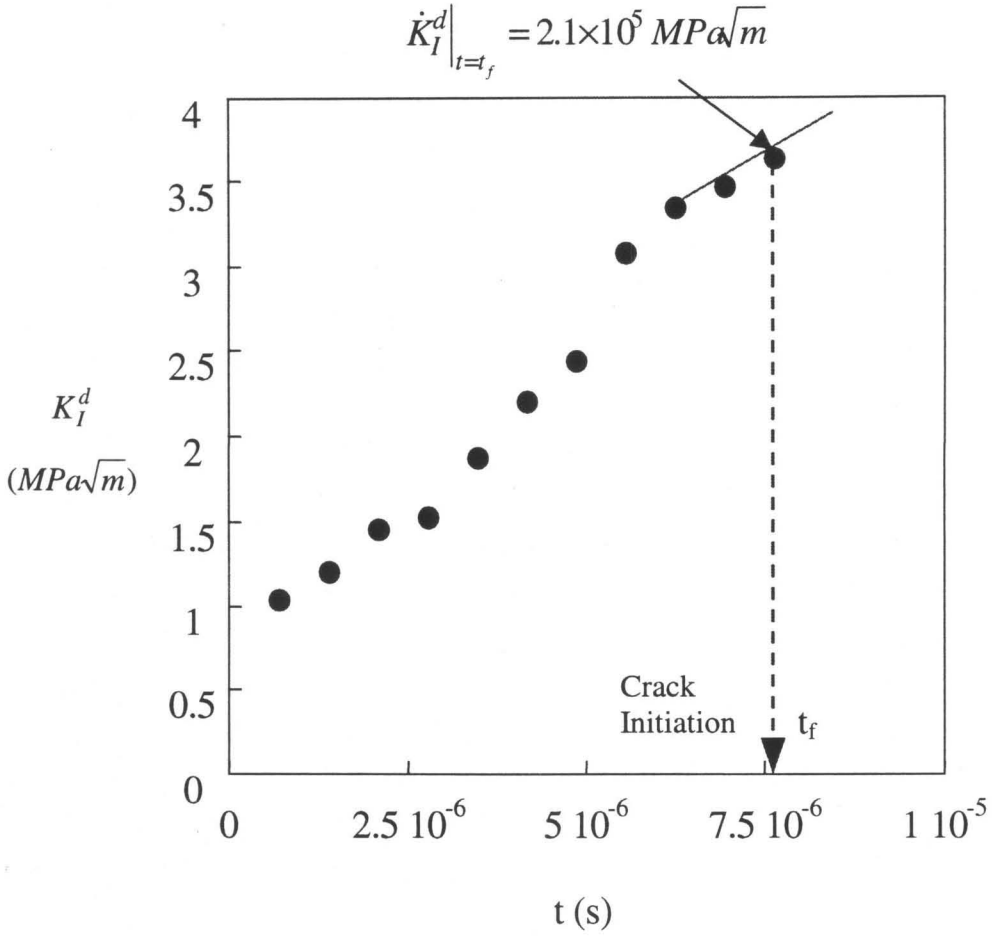
$\dot{K}_I^d\big|_{t=t_f} = 2.1\times10^5\ MPa\sqrt{m}$
K_I^d
$(MPa\sqrt{m})$
4
3.5
3
2.5
2
1.5
1
0.5
0
Crack
Initiation
t_f
0
2.5 10-6
5 10-6
7.5 10-6
1 10-5
t (s)

Figure 9

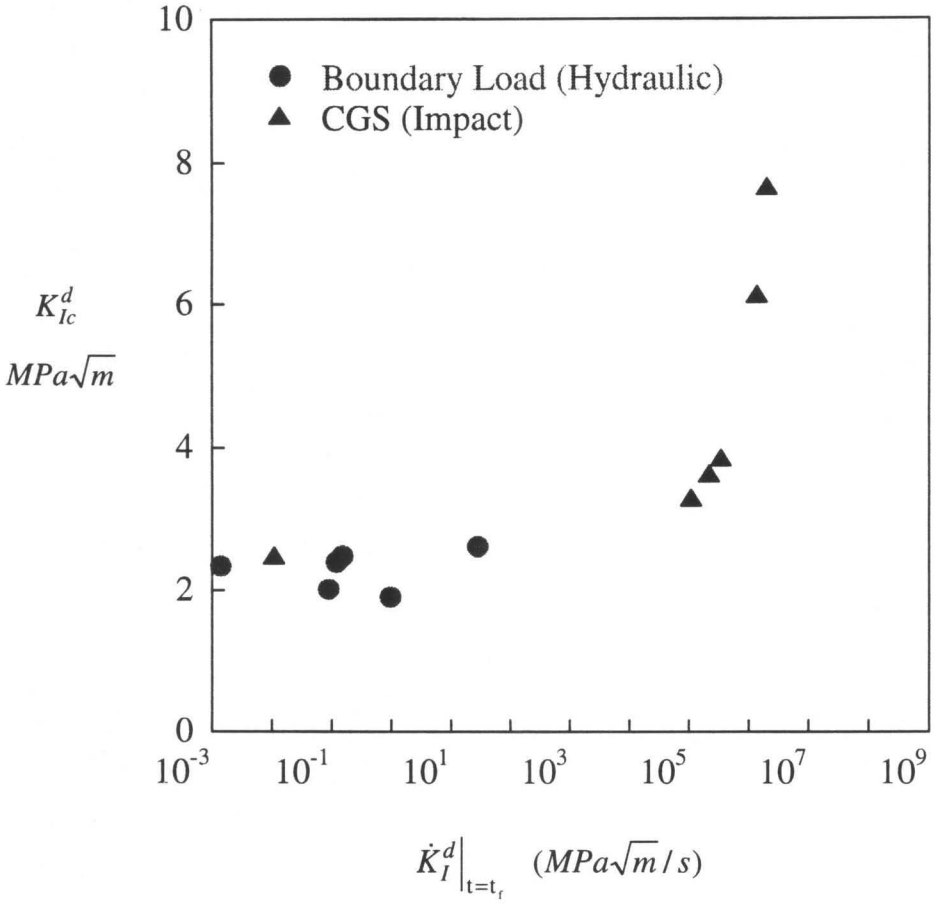
10
8
6
4
2
0
Boundary Load (Hydraulic)
CGS (Impact)
K_{Ic}^{d}
$MPa\sqrt{m}$
10^{-3}
10^{-1}
10^{1}
10^{3}
10^{5}
10^{7}
10^{9}
$\dot{K}_I^d\big|_{t=t_f}$ $(MPa\sqrt{m}/s)$

Figure 10

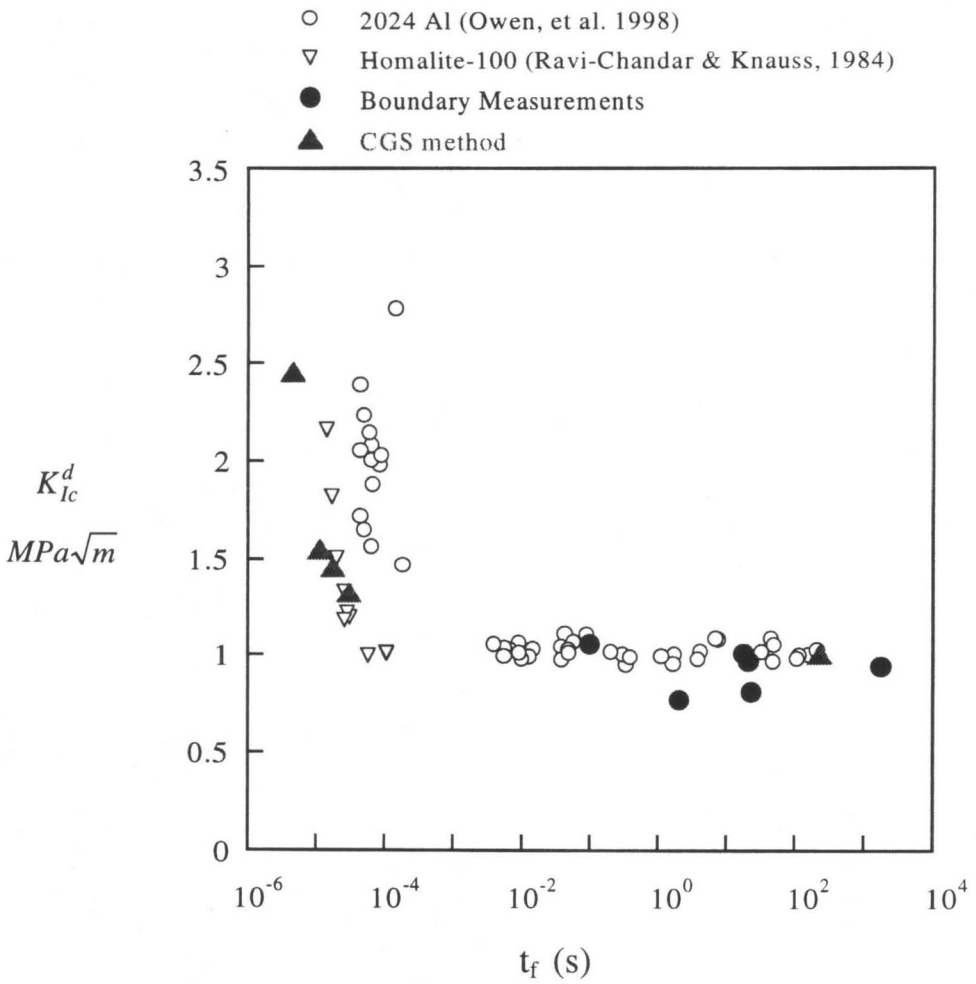
2024 Al (Owen, et al. 1998)
Homalite-100 (Ravi-Chandar & Knauss, 1984)
Boundary Measurements
CGS method
K_{Ic}^{d}
$MPa\sqrt{m}$
3.5
3
2.5
2
1.5
1
0.5
0
10^{-6}
10^{-4}
10^{-2}
10^{0}
10^{2}
10^{4}
t_f (s)

Figure 11

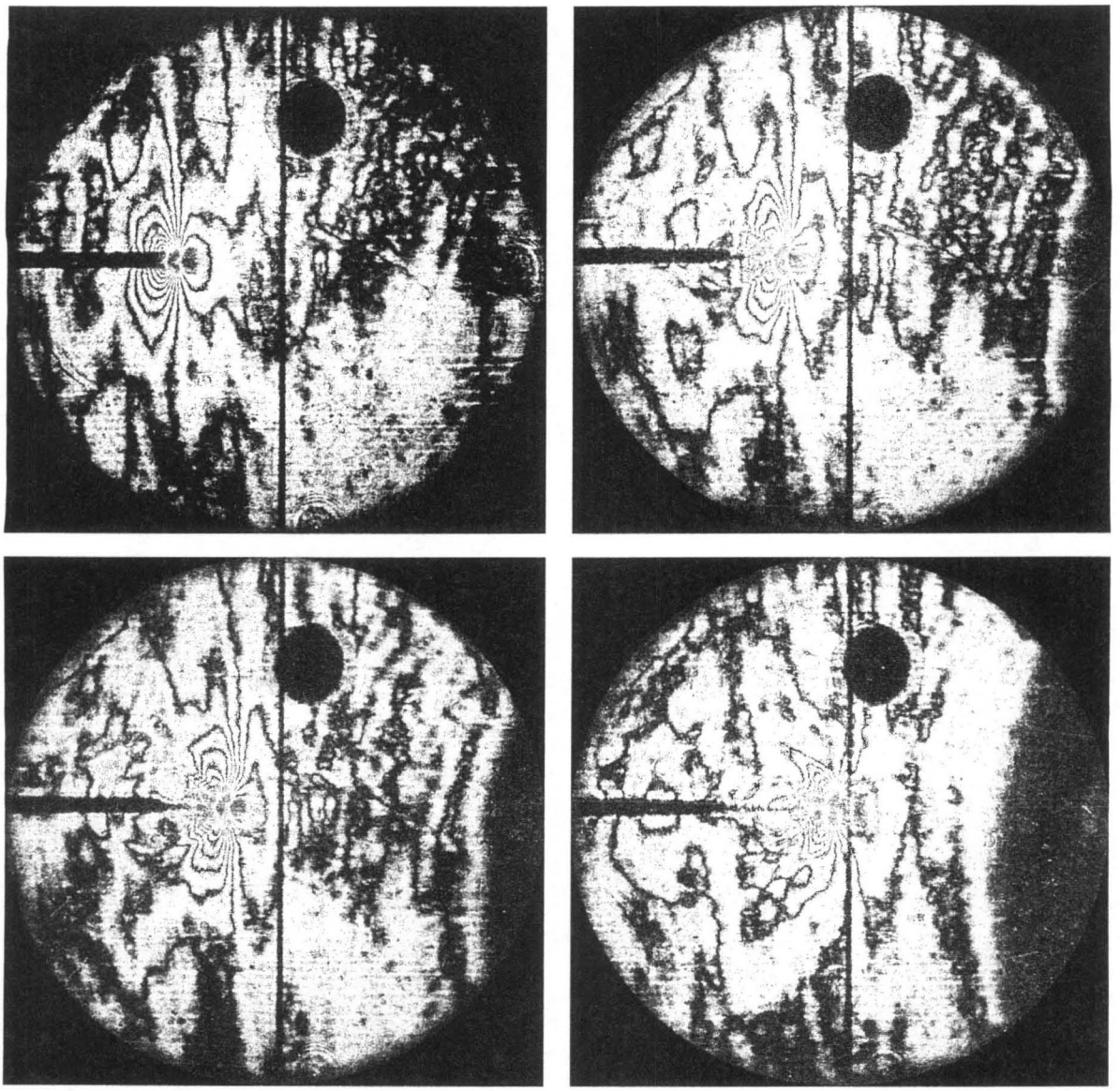

Figure 12

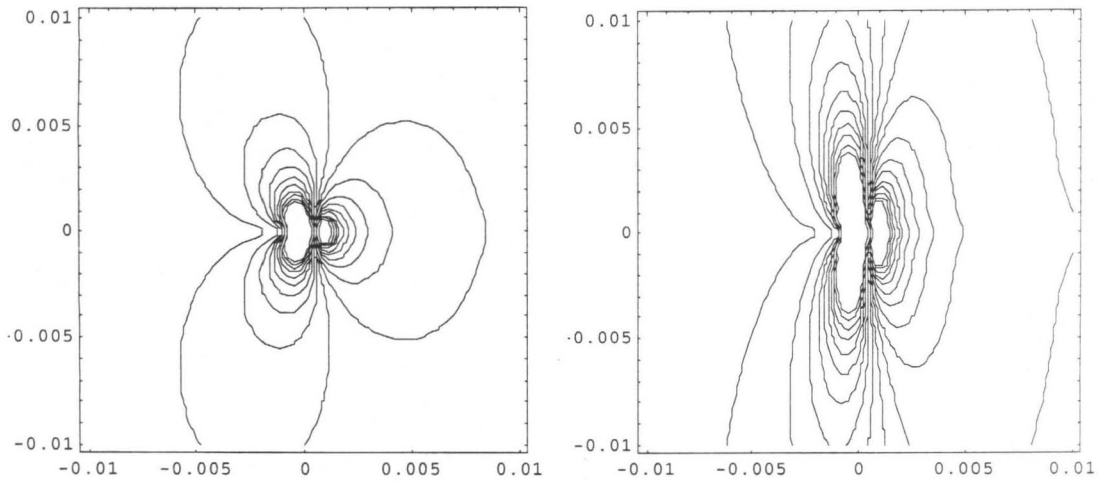
0.01
0.005
0
-0.005
-0.01
-0.01
-0.005
0
0.005
0.01
0.01
0.005
0
-0.005
-0.01
-0.01
-0.005
0
0.005
0.01

Figure 13

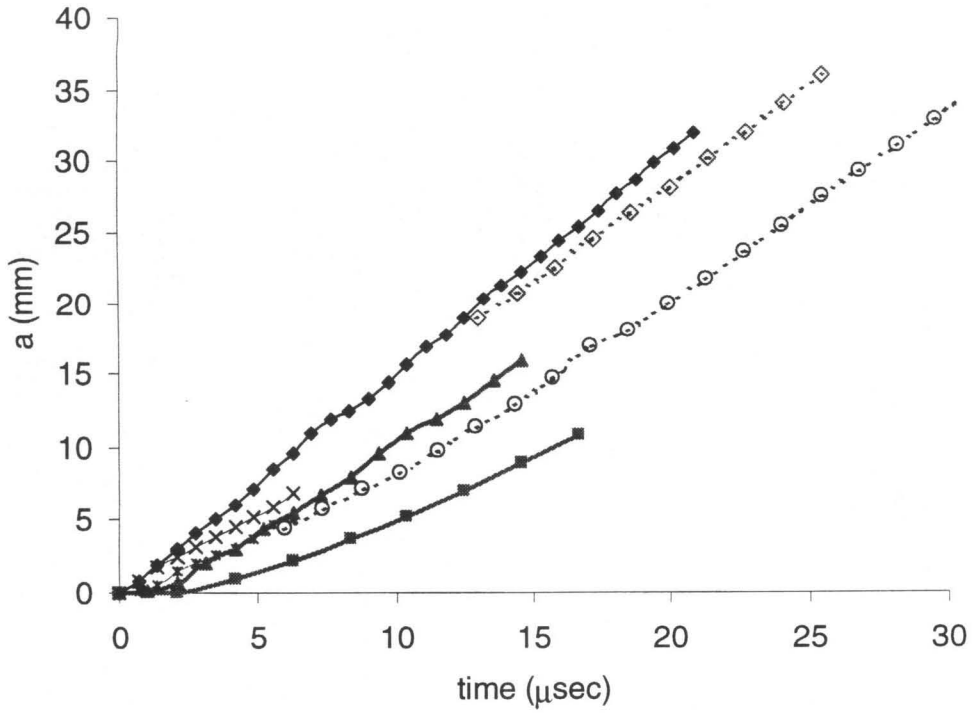
40
35
30
25
20
15
10
5
0
a (mm)
0
5
10
15
20
25
30
time (μsec)

(a)

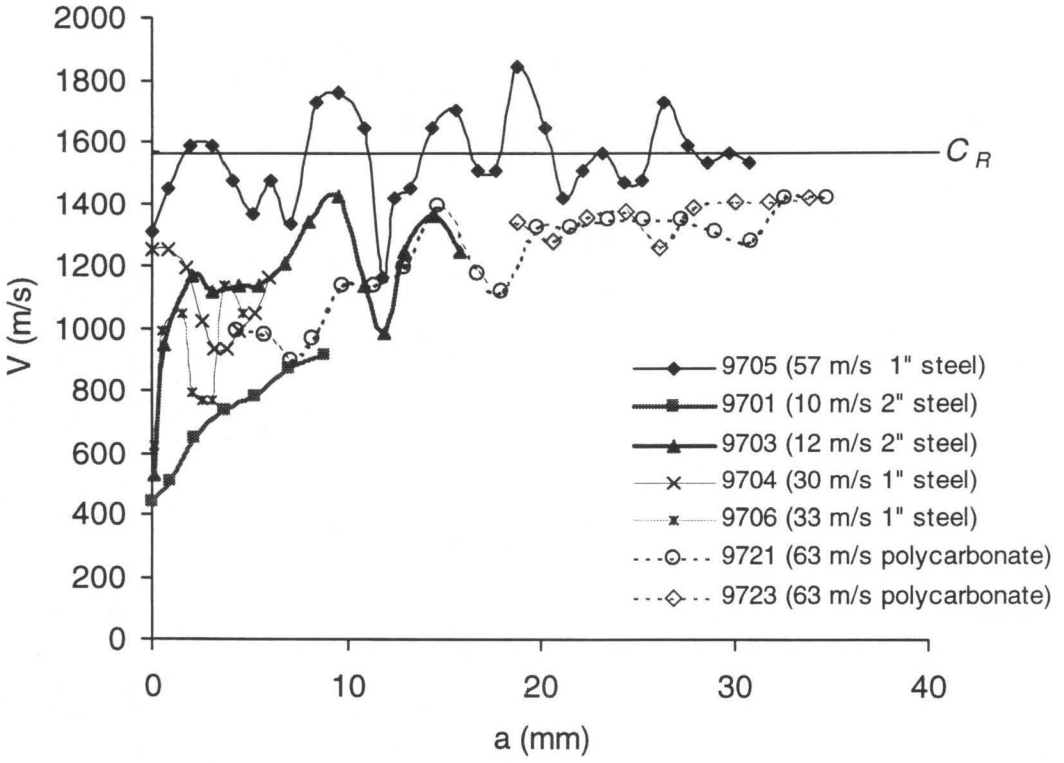
2000
1800
1600
1400
1200
1000
800
600
400
200
0
V (m/s)
0
10
20
30
40
a (mm)
C_R
9705 (57 m/s 1" steel)
9701 (10 m/s 2" steel)
9703 (12 m/s 2" steel)
9704 (30 m/s 1" steel)
9706 (33 m/s 1" steel)
9721 (63 m/s polycarbonate)
9723 (63 m/s polycarbonate)

(b)

Figure 14

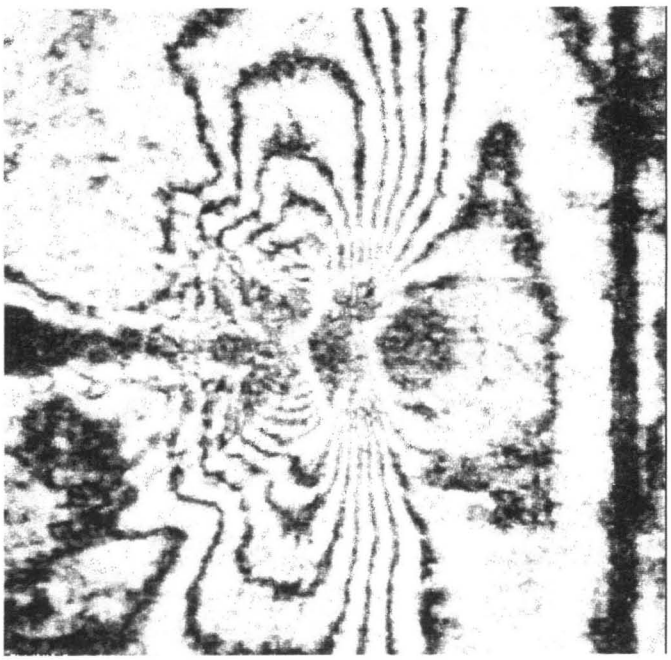

(a)

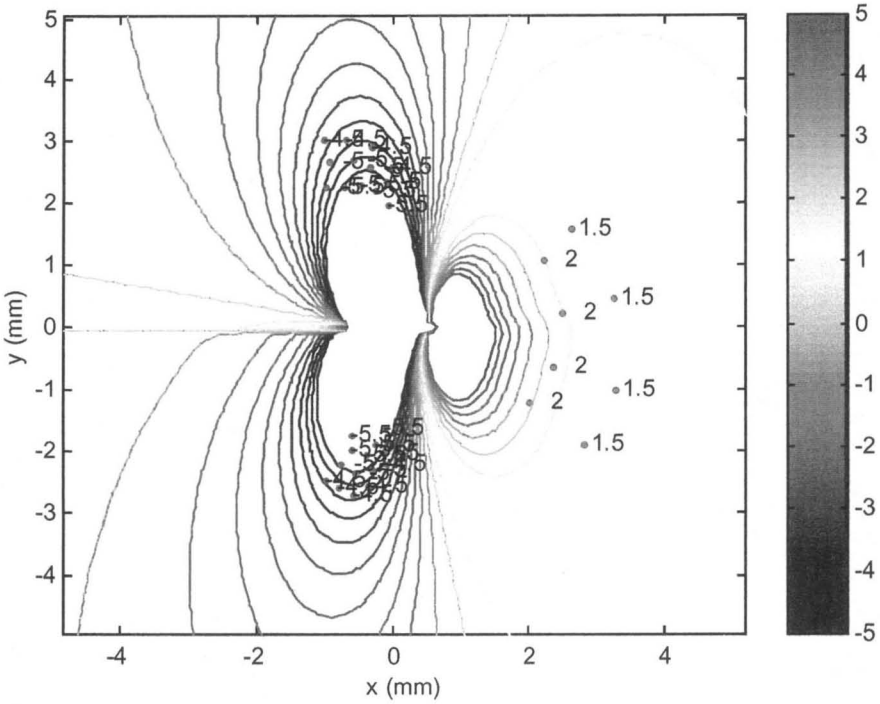

(b)

Figure 15

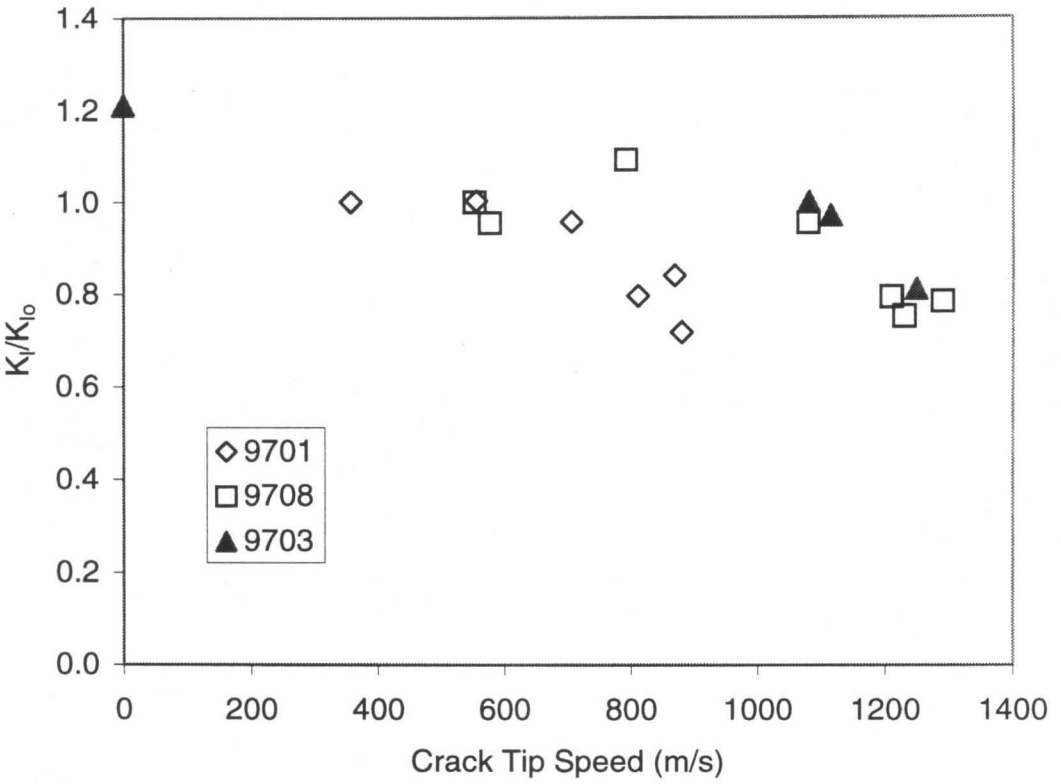
1.4
1.2
1.0
0.8
0.6
0.4
0.2
0.0
K_I/K_{Io}
0
200
400
600
800
1000
1200
1400
Crack Tip Speed (m/s)
9701
9708
9703

Figure 16

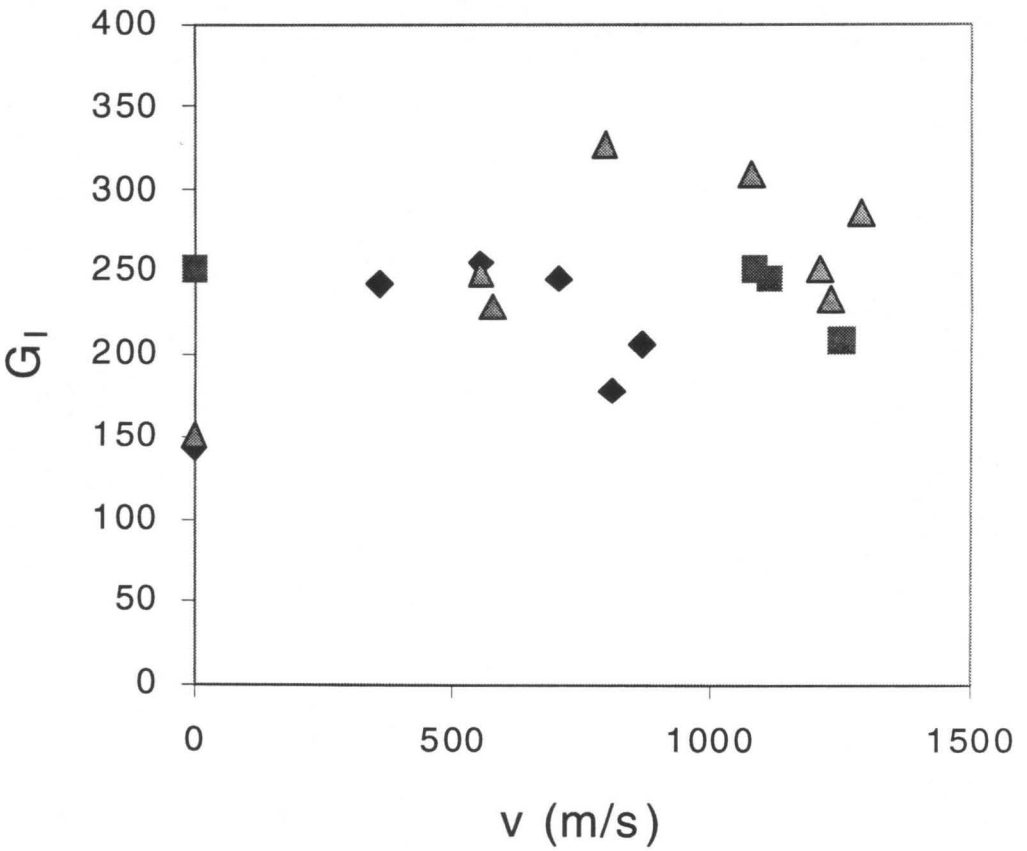

Figure 17

Chapter 3

Intersonic and Supersonic Crack Propagation at the Interfaces of Brittle Homalite/Composite Bimaterials

ABSTRACT

Dynamic crack growth is investigated along composite/Homalite interfaces subjected to impact loading. The specimens are loaded in different configurations by impacting them with a projectile. This dynamic loading causes the cracks to initiate and subsequently grow along the interface at very high speeds. The crack growth phenomenon is observed with dynamic photoelasticity in conjunction with high-speed photography. Varying the impact configuration resulted in different crack propagation speed regimes. On the basis of crack tip speeds three crack growth regimes are identified: crack growth at the dilatational wave speed of the composite, at the dilatational wave speed of the Homalite and at $\sqrt{2}$ times the shear wave speed of the Homalite. First conclusive evidence of crack growth at supersonic speeds with respect to lower speed material and sonic speeds with respect to the unidirectional composite is obtained. In addition, this investigation documents the first experimental observation of a mother/daughter crack mechanism allowing a subsonic crack to evolve into an intersonic crack. Finite element computations featuring cohesive elements predict the phenomena of supersonic crack growth and are validated by the experiments.

1 INTRODUCTION

Composite/metal bonded interfaces are to be found in many engineering applications such as the new generation of marine structures, lightweight missiles, turbine blades of gas turbine engines, etc. The adhesive bonding of composites to metals is often favored over traditional bolting since it increases the reliability of the structure by avoiding puncturing or drilling of holes in the composite. Under dynamic loading, such as impact and explosions, these structures fail at the weakest regions, which usually coincide with the bonded interfaces. Most of these structures are designed to sustain stress wave induced loading and as a result the field of dynamic interfacial failure becomes an important area of investigation. In addition, failure along interfaces is a highly dynamic event with cracks running at speeds comparable to the wave speeds in the constituent materials. In this paper we investigate very fast shear dominated crack growth in the interfaces of composite/homalite bimaterials.

In homogeneous isotropic materials, experimental, theoretical and numerical work has conclusively described the allowable crack propagation speed regimes. In Mode-I crack growth, the theoretical crack tip limiting speed is the Rayleigh wave speed of the material, c_R (Broberg, 1960; Freund, 1990), while super-Rayleigh propagation is excluded by energy considerations. Growing mode-II cracks cannot be sustained in purely homogeneous solids unless such cracks are trapped by a weak prescribed path or by an interface. When such a preferable crack path exists, mode-II cracks can grow and much like their mode-I counterparts they can theoretically accelerate up to c_R. In addition, theoretically, mode-II cracks can also grow at speeds between the shear wave

speed (c_s) and longitudinal wave speed (c_l) (i.e. intersonic speeds) (Freund, 1979; Broberg, 1989). However, the transition between sub-Rayleigh to intersonic is not very clear since the region between c_R and c_s is strictly forbidden. One mechanism that has been postulated on the basis of numerical observations is the nucleation of a daughter crack in front of the subsonically growing main crack and the subsequent coalescence of the mother and daughter cracks that combine and together continue propagating at intersonic speeds (Burridge, 1973; Andrews, 1976; Abraham and Gao, 2000; Geubelle and Kubair, 2001). Although there has been evidence of this phenomenon both from continuum mechanics computations and molecular dynamic simulations, no direct experimental evidence has been available to confirm the physical attainability of this mechanism. Another way of avoiding the restriction of the forbidden smooth transition between the subsonic and intersonic speeds in mode-II is the scenario of a crack that is spontaneously nucleated and always moves within the intersonic regime. Indeed, Rosakis et al. (1999, 2000) have experimentally shown that spontaneous intersonic shear crack growth is possible in a Homalite material along a weak plane. They observed transient crack tip speeds as high as c_l and steady-state crack propagation at $\sqrt{2}\,c_s$. For a detailed discussion of the state of the art on this subject see Samudrala and Rosakis (2001).

Similarly, past work on homogeneous orthotropic materials have clearly shown that there exist similar preferable crack tip speed regimes. Coker and Rosakis (1998, 2001) have experimentally observed in graphite/epoxy fiber-reinforced unidirectional composites that mode-I cracks cannot surpass the Rayleigh wave speed of the composite. They also

observed that mode-II cracks constrained to move along the major directions of anisotropy (crack path along the fibers) spontaneously became intersonic reaching up to the dilatational wave speed of the transversely isotropic composite and then settling down to a critical speed, v_c, of 6500 m/s. Analytical solutions have shown that (Piva and Hasan, 1996; Huang et al., 1999) this speed is the critical speed at which the energy release rate is finite for intersonic mode-II cracks in transversely isotropic materials and is equivalent to $\sqrt{2}\,c_s$ for isotropic materials. Motivated by these experiments, computational work with cohesive elements were conducted and showed that shear cracks in orthotropic materials can indeed accelerate up to the dilatational wave speed and eventually settle down in the vicinity of v_c, at specific steady state levels depending on the cohesive interfacial strength and on the loading pulse duration (Yu et al., 2001; Hwang and Geubelle, 2000). Although the composite materials were treated as homogeneous orthotropic solids and homogenized material descriptions were used in the above investigations, their success in describing the experimental observations demonstrates the power of homogenization of constitutive properties provided that fracture toughness inhomogeneity is properly accounted for by allowing for the existence of a preferable crack path along the fibers.

Intersonic crack propagation in bimaterials was first observed experimentally by Liu et al. (1993), Lambros and Rosakis (1995), Singh and Shukla (1996), Singh et al. (1997). In the context of bimaterials, we use the term intersonic speed to mean crack tip speed between the shear and longitudinal wave speeds of the lower wave speed material. Similarly, supersonic will mean crack tip speed higher than the longitudinal wave speed

of the lower wave speed material in the system. In these experiments, the higher wave-speed material (such as steel) of the bimaterial was dynamically loaded with a projectile opposite to the initial notch. The crack initiated from the prenotch at the opposite end and propagated at speeds 1.3 times the shear wave speed of the lower wave speed solid, moving towards the impact area. In some cases, at higher impact speeds one or two data points indicated the possibility of supersonic crack tip speeds. Thus it seemed that not only intersonic cracks were possible in bimaterials but also supersonic cracks. These experimental results invigorated analytical (Liu et al., 1995; Yu and Yang, 1995; Huang et al., 1998, 1999) and numerical work (Lo et al., 1994; Xu and Needleman, 1996; Needleman and Rosakis, 1999; Breitenfeld and Geubelle, 1997), in the area of dynamic decohesion in bimaterials. Numerical investigations showed strong dependence of crack tip limiting speeds on the loading rate, bond strength and impact speed. However, this extensive series of studies on bimaterial crack propagation did not conclusively resolve the issue of limiting crack tip speeds. Indeed, this problem is highly complicated by the presence of a series of parameters associated with the nature of the constituent solids and their bonding characteristics as well as the nature of dynamic loading. The relevant parameters include stress wave speed mismatch of the two constituent materials, variable loading configurations (intensity of impact loading, duration, sign of shear) and variable bond strengths.

In this article we examine the effect of loading configuration (which translates to direction of shear with respect to the more compliant material) on the crack tip speed regimes. In contrast, past work varied the crack tip speed regime by only changing the

impact speed or the bond strength. Since we are interested in exploring the maximum limits of crack tip speed history, our study features impact speeds that are higher than previous bimaterial studies as well as weaker bond choices. It should also be noted here that the composite/Homalite bimaterial has a very high mismatch in longitudinal wave speeds (while at the same time having a small density and shear wave speed mismatch). The ratio of the composite longitudinal wave speed to that of Homalite is 3.4 times whereas in Metal-Polymer bimaterials this ratio is close to 2.4. Indeed, the system was chosen so that this ratio would be maximized. In contrast, the shear wave speed ratio is 1.2 for the composite/Homalite system, which is much lower than the Metal-Polymer system with a ratio of the order of 2.5.

The material characteristics and the dynamic fracture experimental setup are described in the next section. Experimental observations and crack tip speeds for different loading configurations are presented afterwards. Finally, the results are discussed and some comparisons are made with finite element computations using cohesive elements.

2 MATERIAL AND SPECIMEN

The bimaterial specimens consisted of a unidirectional composite material bonded to a Homalite-100, a polyester resin that exhibits stress induced birefringence (figure 1). The material properties and wave speeds for Homalite-100 are listed in Table 1 (Rosakis et al., 1998). All properties listed are dynamic properties (equivalent strain rates of the order of 10^3/s and both plane-strain and plane-stress values for the wave speeds are displayed.

The composite material used in this investigation is a fiber-reinforced unidirectional graphite-epoxy composite. The composite plates were manufactured by Composite Mirror Applications, AZ, from 48 layers of graphite fiber and epoxy matrix pre-pregs laid up in the thickness direction to form a plate 6.3 mm thick. The fiber diameter was 7.3 mm and the volume fraction of the fibers in the pre-preg was 60-65%. A cross-sectional view of the composite is shown in figure 1b. If x_1 is taken to be in the direction of the fibers, we then assume that the x_2-x_3 plane perpendicular to x_1 is isotropic since the fibers are randomly distributed. This allows us to treat the composite material macroscopically as a transversely isotropic material. The relevant homogenized material properties and wave speeds were obtained using ultrasonic pressure and shear transducers operating at a frequency of 5 MHz (Coker and Rosakis, 2001) and are presented in Table 1. These properties are the dynamic material properties and were found to be strain rate independent in the ranges tested. Although epoxy is known to be strongly rate dependent, the rate independence of the graphite fiber properties has a dominant effect on the overall mechanical properties. The bar wave speed in the graphite fiber was 11230 m/s and the dilatational wave speed in epoxy was 2500 m/s. As shown in Table 1, there is a significant mismatch in the mechanical properties and more importantly, in cases where inertia plays an important role, in the wave speeds. The ratios of densities and shear wave speeds of composite to Homalite-100 are both 1.2 whereas the ratio in longitudinal wave speeds is 3.4. This is a much larger mismatch than steel/aluminum and polymer bimaterials used in previous investigations (Rosakis et al., 1998; Singh et al, 1997).

The specimen configuration and dimensions are shown in figure 1a. An initial notch, 25 mm long and 2.3 mm wide, was machined along the bond line at one edge of the Homalite-100 half. The Homalite part, as machined, was bonded to the composite using two adhesives: Weld-on 10 which is a two part adhesive consisting of methylmethacrylate monomer base resin and a catalyst containing methylethylketone, and Super Glue which is a single component adhesive consisting of ethylcyanoacrylate. The tensile strengths of these two adhesives are greater than 25 Mpa and less than the strength of Homalite. Although this can be regarded as a strong bond, the interfacial bond strength is always weaker than the bulk strength of either of the monolithic materials themselves and thus conducive to interfacial crack growth. The composite was oriented such that the fibers were parallel to the interface.

The specimens were dynamically loaded by impacting them with a steel projectile in three configurations as shown in figure 2. The three configurations are, impacting the composite below the notch (case 1), impacting Homalite-100 above the notch (case 2) and impacting the composite on the side opposite to the notch side (case 3). In all these cases, the nature of the loading arrangement resulted in a crack tip at the interface loaded primarily in shear. In some of the tests, a steel piece was bonded to the specimen on the impact site to prevent shattering of the Homalite part or the crushing of the composite plate and to induce a more or less planar wave front. Thus, different configurations at the site of impact used are shown in figure 2a. Configuration 1 uses the steel plate and the

impact site is 35 mm below the line of the interface whereas the two other configurations allow the impact to be right below the interface line.

3 EXPERIMENTAL METHOD

The experimental setup used to investigate dynamic crack propagation at the interface of a Homalite/Composite bimaterial specimen is shown in figure 3. The specimen was subjected to impact loading on the edge through either a 1" or 2" diameter steel projectile using a pressurized gas gun. Very moderate impact speeds of 20-50 m/s were used. A coherent, monochromatic, plane–polarized laser beam collimated at 100 mm is transmitted through the transparent Homalite half of the specimen. The stress field in the Homalite part is observed using dynamic photoelasticity in conjunction with high-speed photography.

Two sheets of circular polarizers (1/4-wave plate together with a linear polarizer) are placed on both sides of the specimen to form a circular polariscope. This allows us to use photoelasticity to observe the stress-state in a birefringent material such as Homalite. The method of photoelasticity has been described in Dally and Riley (1991) and for dynamic photoelasticity see, for example, Dally (1978). The generation of the isochromatic fringe pattern is governed by the stress optic law, which gives us the relationship between the fringe order at a point and the local in-plane principal stress components as

$$\sigma_1 - \sigma_2 = 2\tau_{\max} = \frac{F_\sigma}{h} N \ ,$$

where Fs is the material fringe constant associated with the incident light wave length, l, h is the specimen thickness, and N is the isochromatic fringe order. For Homalite-100, Fs=22.6 kN/m at a wavelength of 514.5 nm, and h=6.4 mm.

The resulting isochromatic fringe pattern was captured in real time on the film track of a rotating mirror type high-speed camera (Cordin model 330A) with a lens. The camera is capable of recording 80 frames at framing rates of up to 2 ´106 frames s-1 (0.5 ms interframe time). In the current experiments, the interframe time was 2.32 ms and the image was recorded on 35 mm black-and-white KODAK TMAX-400 film. The laser used was an argon-ion laser operating at a wavelength of 514.5 nm in a pulsed mode of 8 ns pulse width. The recording process of the event commenced with the impact of the projectile on a strain gage mounted on the point of impact, leading to a sharp voltage jump, thus triggering pulsing of the laser. In some experiments, a high-speed digital camera was used that is capable of framing rates of up to 100 million frames per second and could record 16 frames in an experiment.

4 Experimental Results

Three types of experiments were conducted where the specimen was impacted at different locations as explained in the previous section (figure 2). Table 2 shows the loading configuration for the experiment, the impact speed, the time of crack initiation and the steady state crack tip speed attained in each case. In all cases, the nature of the loading waves results in loading the crack tip primarily in shear and the nature of the stress wave loading is explained for each case next.

4.1 Stress Wave Loading

In case 1, the composite is impacted below the notch. A compressive loading wave front travels at the higher speed of longitudinal waves in the composite at 7400 m/s as shown in figure 4a. Because of the strong bond between the composite and the Homalite, the Homalite part is loaded by the loading wave at the interface causing a head wave to appear in Homalite. The existence of the head wave is due to the fact that the speed of the loading wave in the composite is supersonic with respect to the Homalite longitudinal wave speed. The acoustic mismatch across the bimaterial interface greatly reduces the transfer of energy from the composite to the Homalite. Thus, if an interface crack forms it would be driven by the composite loading wave and it would primarily be in a state of shear.

In case 2, the Homalite is impacted and the stress wave front progresses at the longitudinal wave speed of the Homalite (figure 4b). When the wave front hits the interface, it spreads in to the composite in which it travels at the longitudinal wave speed of the composite. This wave front then loads the Homalite at the interface far ahead of the initial wave front in Homalite. However, most of the wave energy and the particle velocity are in Homalite, which loads the crack in shear. Under this loading the crack has a tendency to grow into the composite in mode-I, but instead chooses to graze along the interface. Indeed, the high toughness of the composite along the fibers does not allow this crack to enter the lower part of the bimaterial and traps it in a prescribed path along the interface.

In case 3, the composite is loaded along the opposite edge from the notch (same as figure 4a). Initially the wave causes a head wave in the Homalite due to fast longitudinal wave speed in the composite. Again, the acoustic mismatch across the bimaterial interface greatly reduces the transfer of the stress wave energy from the composite to the Homalite. The main compressive dilatational stress reaches the notch tip and it loads the crack primarily in shear. At a later time, when the compressive loading wave is reflected from the edge as a tensile wave, it doubles the particle velocity in the composite enhancing the state of shear around the crack tip. An important difference between this type of loading and the two other cases is the fact that the crack often initiates under the action of the now reflected (tensile) wave. In this scenario, stresses normal to the interface are tensile (through the weak Poisson's ratio effect) and the resulting crack tip loading is one of shear and tension rather than shear and compression.

4.2 Case 1: Impact of the composite on the notch edge

Three experiments were conducted as listed in Table 2 where the composite was impacted below the notch at a high impact speed of 40 m/s. The bimaterials were bonded with Super Glue. In the initial set of tests, a steel piece was impacted as shown in configuration 1. The initial geometry and location of the steel piece caused the center of impact to be 30 mm lower than the level of the interface subjecting the crack tip to mixed-mode loading and the crack to initiate and propagate into the Homalite before it had a chance to experience high shear loading as shown in figure 5. Thus to increase the relative particle motion mismatch in shear and to initiate an interfacial crack, the

composite was impacted closer to the notch line in configuration 2 (figure 2). This succeeded in suppressing the initiation of a crack into the Homalite.

A typical sequence of isochromatic fringe patterns for this set of experiments (case 1) is shown in figure 6. The field of view is approximately 100 mm in Homalite with the loading applied from the left hand side on the composite (figure 2a). The interframe time between the pictures is 3 μs. Two sets of fringes are observed. The first broad fringes correspond to the longitudinal head wave and an angle of 17° corresponds to a disturbance at the interface traveling at 7300 m/s. This is the compressional loading wave due to impact traveling at the longitudinal wave speed of the composite in the direction of the fibers and loading the Homalite at the interface.

A second set of fringes are noticeable at a more shallow angle of 10° following the loading wave in the composite which corresponds to the interfacial disturbance traveling approximately at 7200 m/s. In the second and third pictures, this band is suddenly disrupted with seemingly random fringes. This observation is different from a general loading of the interface by a loading wave traveling in the composite. In this case, the angle and spacing of the fringes gradually change.

Therefore we hypothesize that the images in figure 6 are pictures of a disturbance due to the formation of a crack behind the set of shear Mach waves. Two indications of a crack are as follows: there is no damage in front of the shear Mach waves whereas behind the fringes there is a damaged/rough region behind the shear fringes. Another indication is

the sudden change in spacing and slope due to the separation and sliding [emitting strong shear waves]. In addition, a secondary set of fine fringes is observed (figure 6d). There is a region of vortical fringe pattern between these two bands of shear fringes. We also observe the presence of secondary vertical mode-I cracks emanating from the interface at 60°. Similar secondary cracks resulting from frictional contact of the shear crack faces were observed before in other intersonic shear cracks in the Homalite/Homalite systems (Rosakis et al., 2000). Thus, we conclude, that there is a loading wave traveling at 7400 m/s followed by a supersonic crack tip at 7200 m/s. This conclusion is also supported by finite element calculations.

The interfacial cracks described above are so fast that we only obtain several frames before the crack tip moves out of field of view. Identification of a crack is made harder by the fact that in these photographs we do not observe the formation of typical fringe patterns associate with a crack tip in photoelasticity. Nor do we expect to see the typical stress field around a crack, since these are supersonic cracks and the information about the crack cannot spread beyond the Mach wave.

4.3 Case 2. Impact of Homalite-100 on the notch edge

In case 2, the Homalite part is impacted above the notch at speeds varying from 20-50 m/s as shown in figure 2a (case 2). In this case, all loading configurations were used (figure 2b). The progress of the loading compressional wave front in the Homalite is shown in figure 7. The wave is not perfectly vertical because, in this specimen, impact occurs in configuration 1, with the center of impact being 35 mm above the notch. As

mentioned before, some of the loading is transferred into the composite where the wave speed is higher causing a head wave in Homalite ahead of the loading wave front.

In figure 8, a sequence of isochromatic fringes around the crack tip is shown for specimen HCa impacted at 40 m/s. The interframe time is 5 μs. In this case, the photoelastic fringe pattern around the crack is a more familiar pattern observed for dynamically growing cracks at intersonic speeds (Singh and Shukla, 1996; Samudrala and Rosakis, 2001). A line of discontinuity, a shear shock wave, radiating from the crack tip at an angle close to 45° can be observed. This signifies that the crack is moving faster than the speed of the shear wave in Homalite. From the relation between the crack tip speed and the Mach angle, we calculate the crack tip speed to be $\sqrt{2}$ times the shear wave speed of Homalite. Also in figure 9a crack tip location as a function of time is presented. The crack tip speed is also calculated from a progressive 3-pt least squares fit to the crack tip history. The speed as a function of distance x_1 from both methods is shown in figure 9b which shows that the steady state crack tip speed is approximately $\sqrt{2}\, c_s$. In other experiments where the Homalite is impacted at different speeds, the same average steady state crack tip speed is obtained and thus is shown to be independent of the impact speed for the range tested here and for the strong bonding used in this investigation.

4.4 Case 3. Impact of the composite on the opposite edge from the notch

Two experiments were conducted for case 3 (see Table 2). A time sequence of photographs is shown in figure 10 for the slower impact speed of 27 m/s. The notch tip is on the lower left corner and the composite is impacted on the right hand side. In the first

frame, a loading wave approaching from the right can be seen. When the loading wave passes the crack tip it loads the crack primarily in shear because the wave speed mismatch between Homalite and the composite greatly impedes the transfer of the stress waves from the composite to the polymer. After the wave reflects off the left hand side and doubling the particle velocity, the crack initiates driven by the composite side. The interfacial crack propagates from the notch tip to the right at 1100 m/s, which is close to the Rayleigh wave speed of the Homalite. The crack tip history and crack tip speed is shown in figure 11. In this process a very unique phenomenon is observed. As seen in frame 4, a small daughter crack nucleated in front of the major crack and later coalesces with the mother crack. Afterwards, both crack coalesce and travel at a new crack tip speed of approximately 2100 m/s with a corresponding shear shock wave. This is very similar to the mother/daughter mechanism that was observed by Andrews and Burridge in their calculations (Andrews, 1976; Burridge, 1973), involving growing shear cracks moving along weak planes in constitutively homogeneous materials. This mechanism was proposed in response to the question of how subsonic shear cracks become intersonic since they have to pass through the forbidden region between the Rayleigh wave speed and the shear wave speed to become intersonic. This mechanism has also been observed in molecular dynamic simulations of Abraham and Gao (2000) and spectral scheme of elastodynamics by Geubelle and Kubair (2001). This observation is the first experimental proof of the mother/daughter mechanism for accelerating shear cracks along prescribed path, albeit in a bimaterial and not a homogeneous material.

A second experiment was conducted at a higher impact speed of 40 m/s. In this case our time resolution did not allow us to capture the sudden acceleration of the crack tip so we do not observe the formation of a daughter crack. The crack tip position as a function of time, and crack tip speed as a function of position are shown in figure 11. In both of these cases, the steady state crack tip speed reaches 2100 m/s, which is close to the dilatational wave speed of the Homalite.

5 DISCUSSION

The crack tip speed as a function of time and the coordinate x1 is shown in figure 12a and 12b, respectively, for all three cases discovered here. The steady state crack tip regime for each loading case is different. Case 1 is able to immediately accelerate to 6000 m/s with the energy supplied by the composite side at the dilatational wave speed of the composite. In case 2, depending on the loading rate, and within experimental error, steady state crack speeds either approach $\sqrt{2}\,c_s$ or remain in the neighborhood of c_s. In case 3, the crack tip speeds approach the dilatational wave speed of the Homalite, c_l. It is perhaps perplexing to see drastically different quantized limiting speeds for Cases 2 and 3 even for the same external loading rates. In both cases, the direction of shearing is the same and the direction of particle motion in the Homalite is in the direction of crack growth. One explanation could be that most of the energy is carried by the composite in case 3, pushing the crack faster to the dilatational wave speed of the Homalite. Another reason may be related to the differences in the Poisson's ratio related normal stress acting perpendicular to the interface. For case 2 we have compression while for case 3 we have tension superimposed on the dynamic shear.

The crack tip limiting speeds observed herein are more pronounced in these experiments compared to previous experiments on bimaterials. One reason for this could be the extreme mismatch in the longitudinal wave speeds in the constituent materials (modulus and shear wave speed mismatch is more extreme in metal/polymer bimaterials).

Finally, comparisons are made with finite element computations. The fast crack growth along an interface was simulated using the cohesive surface decohesion formulation of Needleman (1987) and Xu and Needleman (1994) where the failure characteristics are embodied in a phenomenological constitutive relation that describes separation along one or more cohesive surfaces. The parameters characterizing the cohesive surface separation law include the strength and the work of separation per unit area so that a characteristic length enters the formulation. These constitutive relations together with appropriate balance laws and initial boundary conditions completely specify the initial boundary problem. Fracture, when it occurs, emerges as a natural outcome of the loading history. No additional assumptions concerning crack initiation or crack propagation are needed. Crack initiation and the crack speed history are outcomes of the analyses. Plane strain conditions are assumed and a single cohesive surface along the interface between the two solids is specified so that the crack is constrained to grow along the bond line.

Figure 13 shows a comparison of the isochromatic fringe patterns for case 1 between computational and experimental cases. There is a remarkable similarity between the two cases and good agreement in the general features. In both cases, there exists a band of shear shock waves followed by a vortical structure region, and finally followed again by a band of shear shock waves. We can also observe the complicated stress concentrations (resulting from crack face contact) along the interface after the shear crack tip has passed. This kind of extreme deformations at the interface leads to secondary cracks in the experiments. However, the secondary cracks are not observed in the computations because the cohesive elements are only placed along the interface. The crack tip speed

from the computations is approximately 7000 m/s whereas in the experiments it is around 6000 m/s. This difference can be attributed to the fact that the composite dilatational wave speed in the computations is represented by the plane strain value, which is higher than the plane stress value used in the experiments.

6 CONCLUDING REMARKS

Dynamic fracture experiments were conducted in the Homalite/Composite bimaterials to investigate shear dominated interfacial crack initiation and growth. Cracks were found to immediately accelerate to quantized steady state speeds above the shear wave speed of the Homalite. Impacting the composite on the notch side resulted in truly supersonic interfacial crack tip speed, to 7300 m/s, the higher of the two longitudinal wave speeds of the composite, more than three times the longitudinal wave speed of the Homalite. Also, a shock wave structure characteristic of intersonic shear crack growth and emanating from the crack tip was observed. These experiments are the first clear and conclusive evidence of supersonic crack growth with respect to the lower wave speed constituent and sonic speed with respect to the higher speed anisotropic solid. Two other intersonic regimes were identified for different impact configurations. These corresponded to steady state speeds of $\sqrt{2}\,c_s$ and c_l of the Homalite. Cracks instantly accelerated to these discrete speeds within the time resolution of our cameras. Finally, we present experimental proof of the existence of the mother/daughter crack growth mechanism allowing shear dominated interfacial cracks to spontaneously jump from subsonic to intersonic crack tip speeds.

7 REFERENCES

Abraham, F. F. and Gao, H., 2000. How fast can cracks propagate?, *Physical Review Letters*, 84, 3113-3116.

Andrews, D.J., 1976. Rupture Velocity of Plane Strain Shear Cracks, *Journal of Geophysical Research,* 81, 5679-5687.

Breitenfeld, M. S. and Geubelle, P.H., 1997. Numerical Analysis of Dynamic Debonding under 2D In-Plane and 3D Loading, *International Journal of Fracture*, 85, 265-282.

Broberg, K.B., 1960. The Propagation of a Brittle Crack, *Archiv fur Fysik*, **18**, 159-192.

Broberg, K.B., 1989. The near-tip field at high crack velocities, *International Journal of Fracture*, 39, 1-13.

Burridge, R., 1973. Admissible speeds for plane strain shear cracks with friction but lacking cohesion, *Geophysics Journal of the Royal Astronomical Society*, 35, 439-455.

Coker, D. and Rosakis, A.J., 2001. Experimental observations of intersonic crack growth in asymmetrically loaded unidirectional composite plates, *Philosophical Magazine A*, 81, 571-595. Also, The California Institute of Technology Solid Mechanics Report #98-16, 1998.

Dally, J. W., 1978. Dynamic photoelastic studies of stress wave propagation, in *Modern Problems in Elastic Wave Propagation*, Eds. J. Miklowitz and J. D. Achenbach, Wiley, New York, 3-21.

Dally, J. W. and Riley, W. F., 1991. *Experimental Stress Analysis*, McGraw-Hill, New York.

Freund, L.B., 1979. The mechanics of dynamic shear crack propagation, *Journal of Geophysics Research*, 84, 2199-2209.

Freund, L.B., 1990. *Dynamic Fracture Mechanics*, Cambridge University Press, Cambridge.

Geubelle, P. H. and Kubair, D. V, 2001. Intersonic crack propagation in homogeneous media under shear-dominated loading: numerical analysis, *Journal of the Mechanics and Physics of Solids*, 49, 571-587.

Huang, Y., Wang, W., Liu, C. and Rosakis, A.J., 1998. Intersonic crack growth in bimaterial interfaces: an investigation of crack face contact, *Journal of the Mechanics and Physics of Solids*, 46, 2233-2259.

Huang, Y., Wang, W., Liu, C. and Rosakis, A.J., 1999. Intersonic crack growth in unidirectional fiber-reinforced composites, *Journal of the Mechanics and Physics of Solids*, 47, 1893-1916.

Hwang, C. and Geubelle, P. H., 2000. A spectral scheme to simulate dynamic fracture problems in composites, *CMES—Computer Modeling in Engineering & Sciences*, 1, 4, 45-55.

Lambros, J. and Rosakis, A.J., 1995. Shear dominated transonic interfacial crack growth in a bimaterial-i: experimental observations, *Journal of the Mechanics and Physics of Solids*, 43, 169-188.

Liu, C., Huang, Y., and Rosakis, A. J., 1995. Shear dominated transonic interfacial crack growth in a bimaterial-ii. asymptotic fields and favorable velocity regimes, *Journal of the Mechanics and Physics of Solids*, 41, 1887-1954.

Liu, C., Lambros, J., and Rosakis, A. J., 1993. Highly transient elasto-dynamic crack growth in a bimaterial interface: higher order asymptotic analysis and optical experiment, *Journal of the Mechanics and Physics of Solids*, 41, 1887-1954.

Lo, C. Y., Nakamura, T. and Kushner, A., 1994. Computational analysis of dynamic crack propagation along bimaterial interface, *International Journal of Solids and Structures*, 31, 145-168.

Needleman, A., 1987. A continuum model for void nucleation by inclusion debonding, *Journal of Applied Mechanics*, 54, 525-531.

Needleman, A. and Rosakis, A.J., 1999. The effect of bond strength and loading rate on the conditions governing the attainment of intersonic crack growth along interfaces, *Journal of the Mechanics and Physics of Solids*, 47(12), 2411-2449.

Piva, A. and Hasan, W., 1996. Effect of orthotropy on the intersonic shear crack propagation, *Journal of Applied Mechanics*, 63, 933-938.

Rosakis, A.J., Samudrala, O, Singh, R.P. and Shukla, A., 1998. Intersonic crack propagating in bimaterial systems, Eds. Ravichandran, G., Rosakis, A.J., Ortiz, M., Rajapakse, Y.D.S., Iyer, K, Special volume of the *Journal of the Mechanics and Physics of Solids* devoted to Dynamic Failure Mechanics of Solids Honoring Professor Rodney Clifton, 46, 1789-1813.

Rosakis, A.J., Samudrala, O. and Coker, D., 1999. Cracks faster than the shear wave speed, *Science*, 284, 1337-1340. Also, The California Institute of Technology Solid Mechanics Report #98-17.

Rosakis, A.J., Samudrala, O. and Coker, D., 2000. Intersonic shear crack growth along weak planes, *Materials Research Innovations*, 3, 236-243.

Samudrala. O. and Rosakis, A.J., 2001. In preparation.

Singh, R. P. and Shukla, A., 1996. Subsonic and intersonic crack growth along a bimaterial interface, *Journal of Applied Mechanics*, 63, 919-924.

Singh, R.P., Lambros, J., Shukla, A. and Rosakis, A.J., 1997. Investigation of the mechanics of intersonic crack propagation along a bimaterial interface using coherent gradient sensing and photoelasticity, *Proceeding of the Royal Society of London*. A453, pp. 2649-2667.

Xu, X.-P. and Needleman, A., 1996. Numerical simulations of dynamic crack growth along an interface, *International Journal of Fracture*, 74, 289-324.

Yu, C., Ortiz, M., Coker, D., Rosakis, A. J. and Pandolfi, A., 2001. Three-dimensional modeling of intersonic crack growth in asymmetrically loaded unidirectional composite plates, in preparation.

Yu, H. and Yang W., 1995. Mechanics of transonic debonding of a bimaterial interface: The in-plane case, *Journal of the Mechanics and Physics of Solids*, 43, 207-232.

LIST OF TABLES

LIST OF FIGURES

Figure 6. A sequence of isochromatic fringe patterns at an interframe time of 3 μs showing interfacial supersonic crack growth due to impact of the composite on the left hand side (case 1).

Figure 7. Stress waves in Homalite due to impact of Homalite on the left hand side.

Figure 8. A sequence of isochromatic fringe patterns at an interframe time of 5 μs showing interfacial intersonic crack growth and corresponding shear shock front due to impact of the Homalite on the left hand side at an impact speed of 40 m/s (case 2).

Figure 9. (a) Crack tip position as a function of time and (b) crack tip speed evolution as a function of crack length for case 2 (impacting of Homalite).

Figure 10. A sequence of isochromatic fringe patterns at an interframe time of 2.3 μs showing mother/daughter crack growth mechanism due to impact of the composite on the right-hand side at an impact speed of 27 m/s (case 3).

Figure 11. (a) Crack tip position as a function of time and (b) crack tip speed evolution as a function of crack length for case 3 (impacting of Composite opposite to the notch).

Figure 12. Crack tip speed (a) as a function of time and (b) as a function of crack length for all cases considered

Figure 13. Comparison of isochromatic fringe patterns for case 1 (a) experimental, (b) finite element computations with cohesive zone model.

Table 1. Dynamic material properties and wave speeds for Homalite-100 and graphite-epoxy unidirectional composite.

	Homalite-100	Graphite-epoxy Composite
Young's Modulus E (GPa)	5.2	$E^{\parallel} = 80.0$
		$E^{\perp} = 8.9$
Shear Modulus, μ (GPa)	1.9	$\mu_{12} = 3.6$
Poisson's ratio, ν	0.34	$\nu_{12} = 0.25$
Density ρ (kg/m^3)	1230	1478
Shear Wave Speed, c_s (m/s)	1255	1560
Longitudinal Wave Speed (plane strain), $c_l^{pl-\varepsilon}$ (m/s)	2560	$c_l^{\parallel} = 7450$
		$c_l^{\perp} = 2740$
Longitudinal Wave Speed (plane stress) $c_l^{pl-\sigma}$ (m/s)	2187	$c_l^{\parallel} = 7380$
		$c_l^{\perp} = 2470$
Rayleigh Wave Speed (plane stress), $c_R^{pl-\sigma}$	1155	1548
Static tensile strength, σ_o (MPa)	48	36
Static shear strength, τ_o (MPa)	42	27

Table 2. Table of dynamic fracture experiments on Homalite/Composite bimaterial showing impact speed, loading configuration, time to crack initiation after impact, steady-state crack tip speed.

Specimen ID	Impact Speed (m/s)	Loading configuration*	Initiation time (μs)	Steady state crack tip speed** (m/s)
CASE 1. Impact of Composite on the notch edge				
HC13	40	3	8	6500
HCd	35	2	8	6000
HCe	27	2	4	5000
CASE 2. Impact of Homalite on the notch edge				
HC1	22	1	35	$1820 \approx \sqrt{2}c_s$
HC10	30	1	41	$1243 \approx c_s$
HC11	24	1	32	$1291 \approx c_s$
HC15	28	3	31	$1800 \approx \sqrt{2}c_s$
HCa	40	2	35	$1828 \approx \sqrt{2}c_s$
CASE 3. Impact of Composite on the opposite edge from the notch				
HC9	27	1	30	$2080 \approx c_l^H$
HC12	43	1	33	$2150 \approx c_l^H$

* See Fig. 2 for description of case types and loading configurations

** All wave speeds are plane stress values.

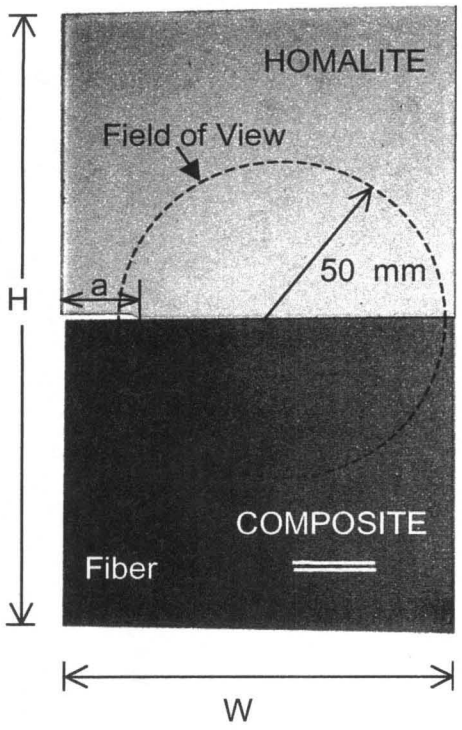
HOMALITE
Field of View
50 mm
a
H
COMPOSITE
Fiber
W

(a)

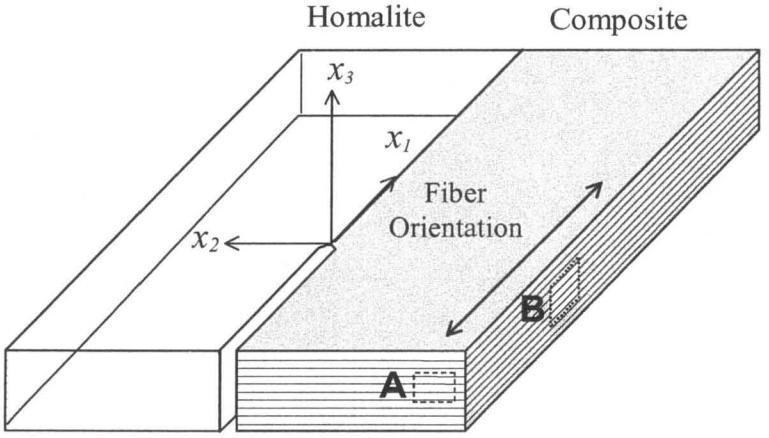
Homalite
Composite
x_3
x_1
Fiber
Orientation
x_2
B
A

(b)

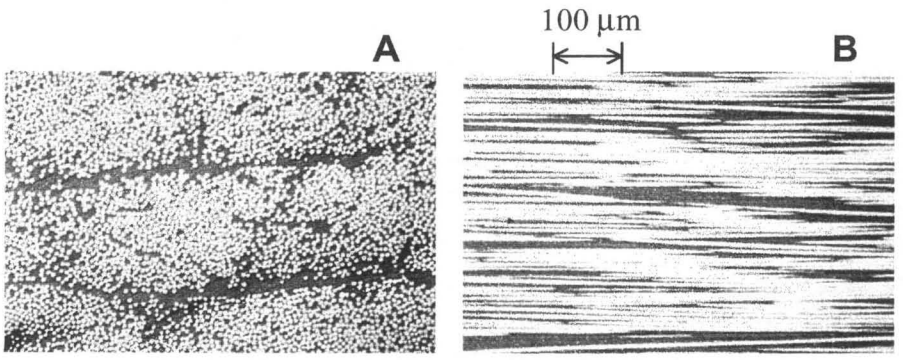
100 μm
A
B

Figure 1

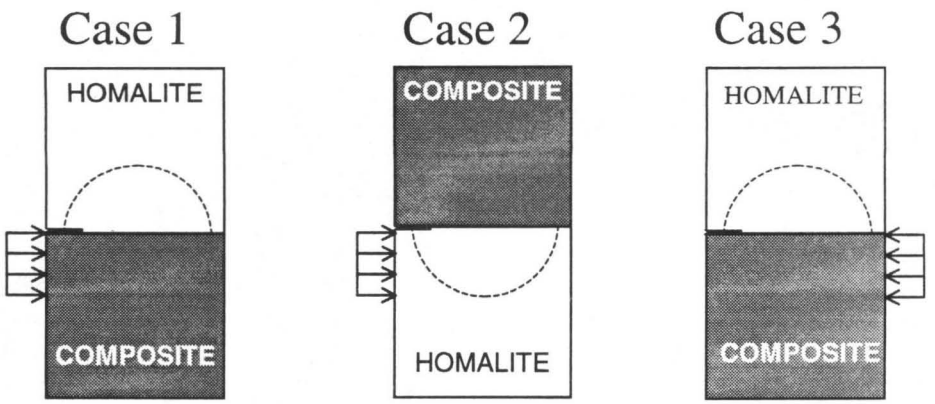

(a)

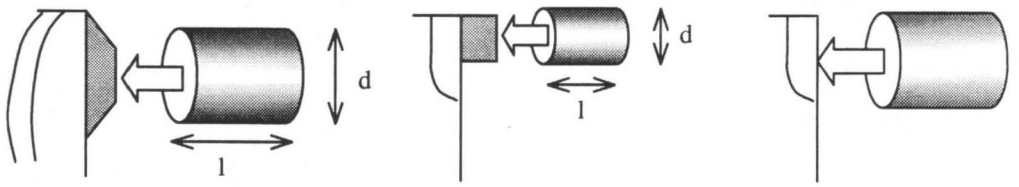

Configuration 1 Configuration 2 Configuration 3

(b)

Figure 2

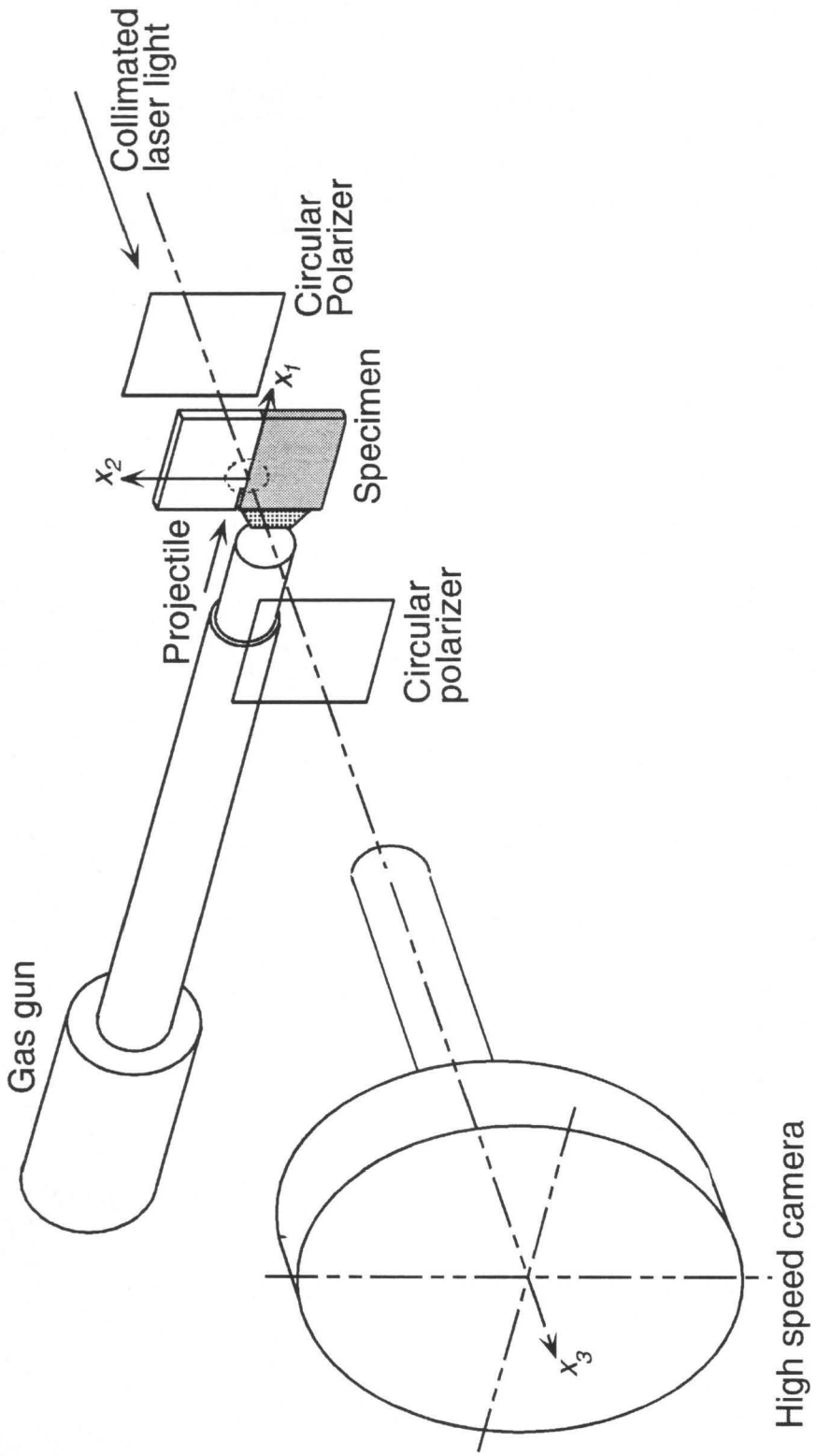
Collimated
laser light
Circular
Polarizer
x_1
x_2
Specimen
Projectile
Circular
polarizer
Gas gun
x_3
High speed camera

Figure 3

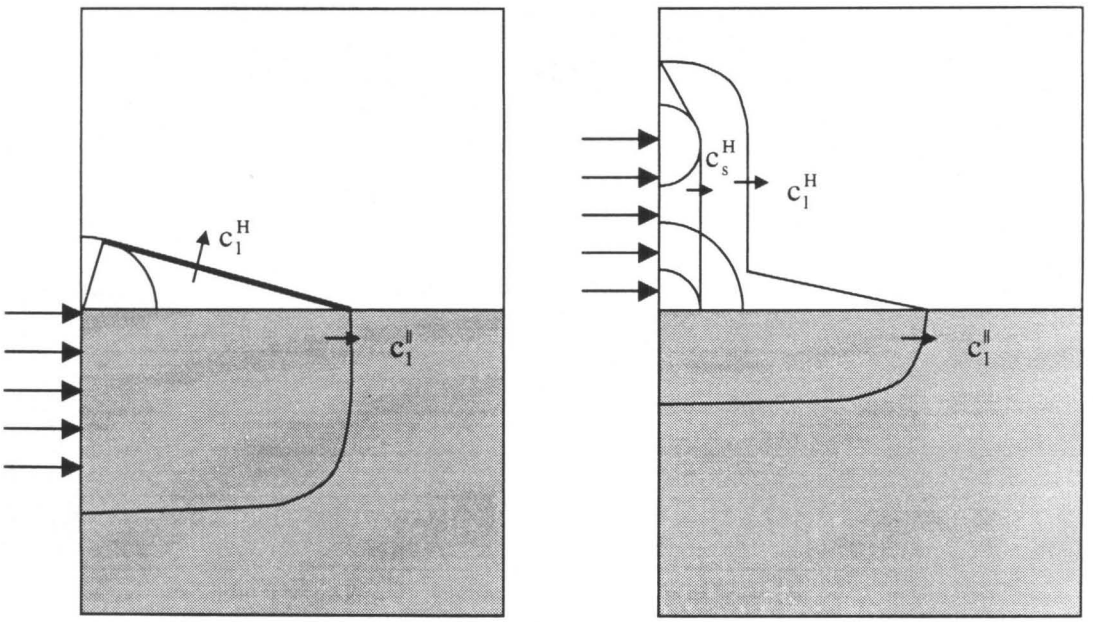

(a) (b)

Figure 4

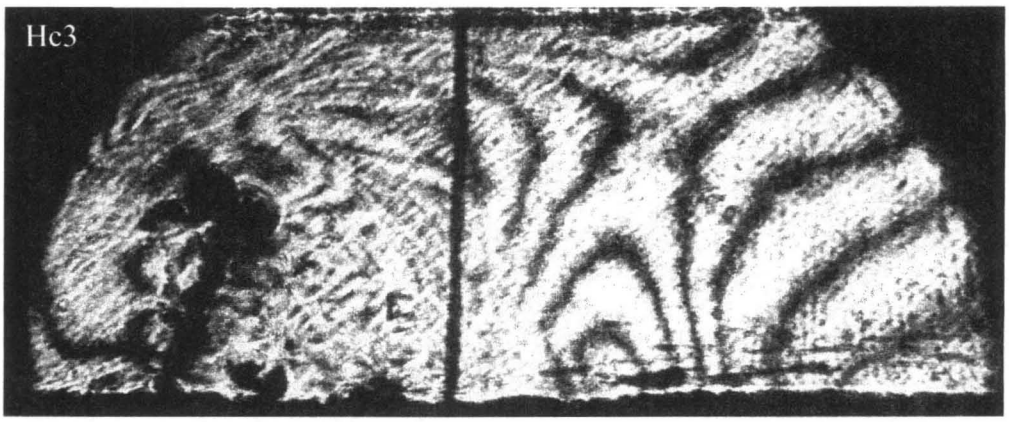

Figure 5

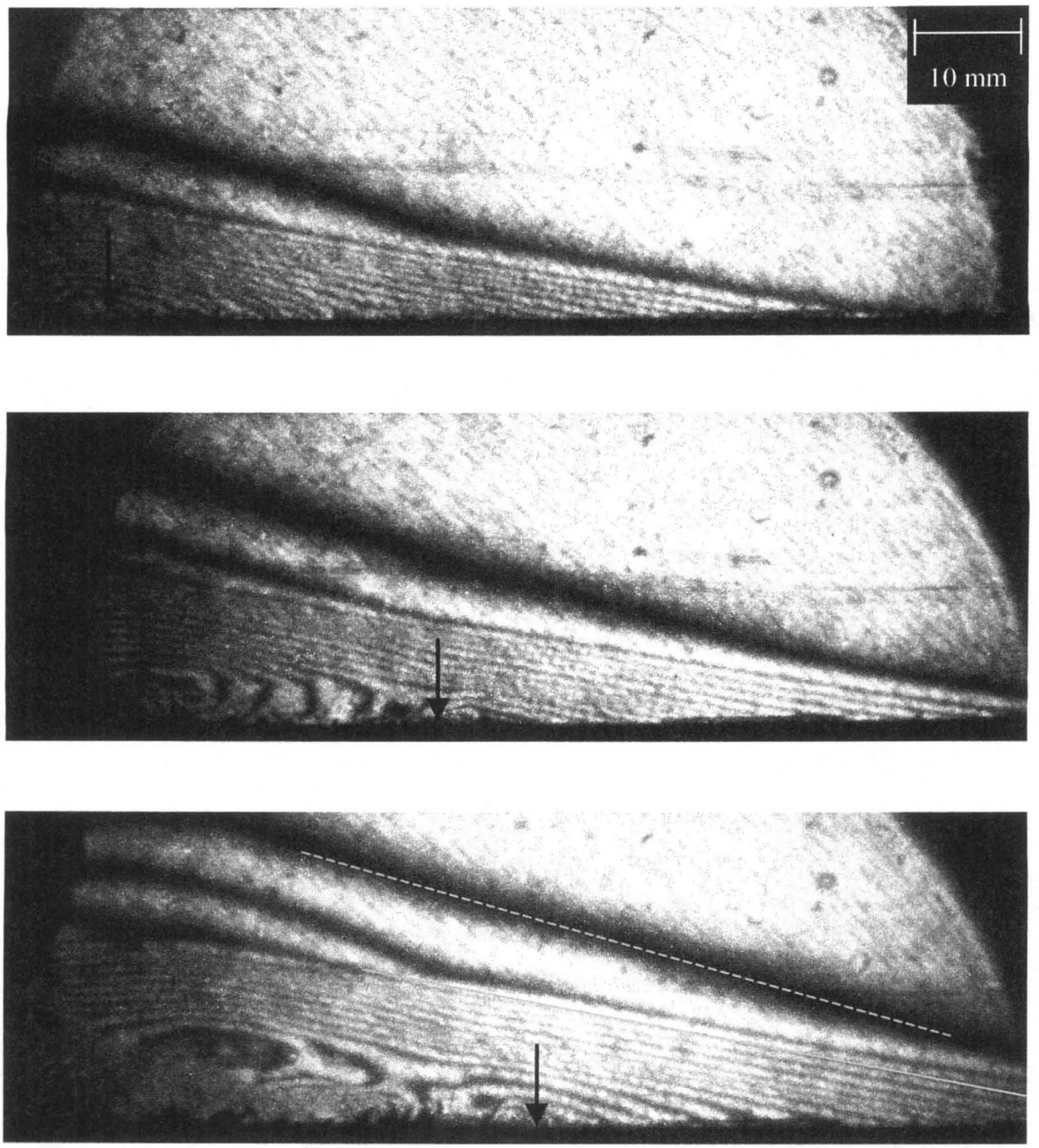

Figure 6

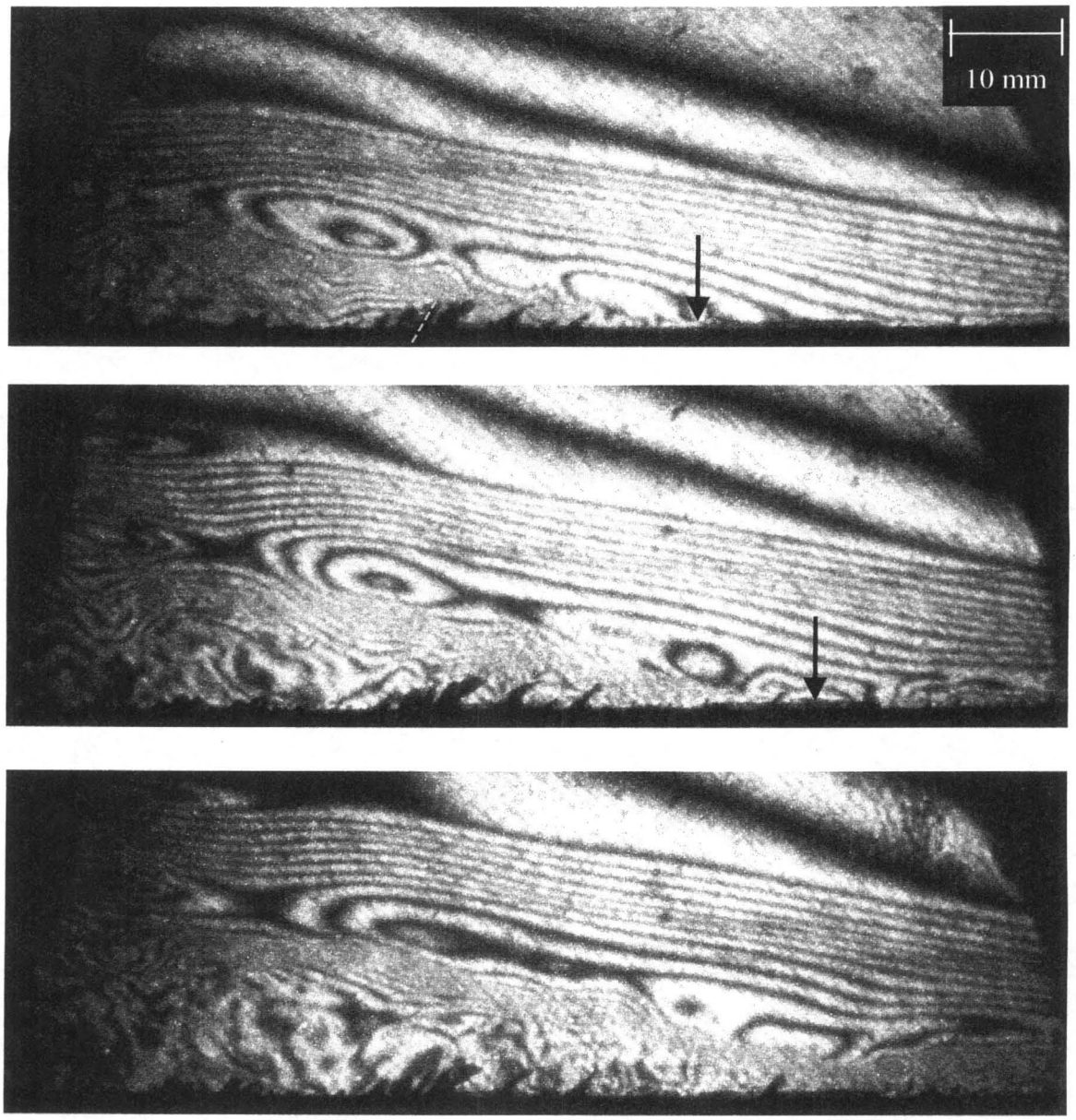

Figure 6 (continued)

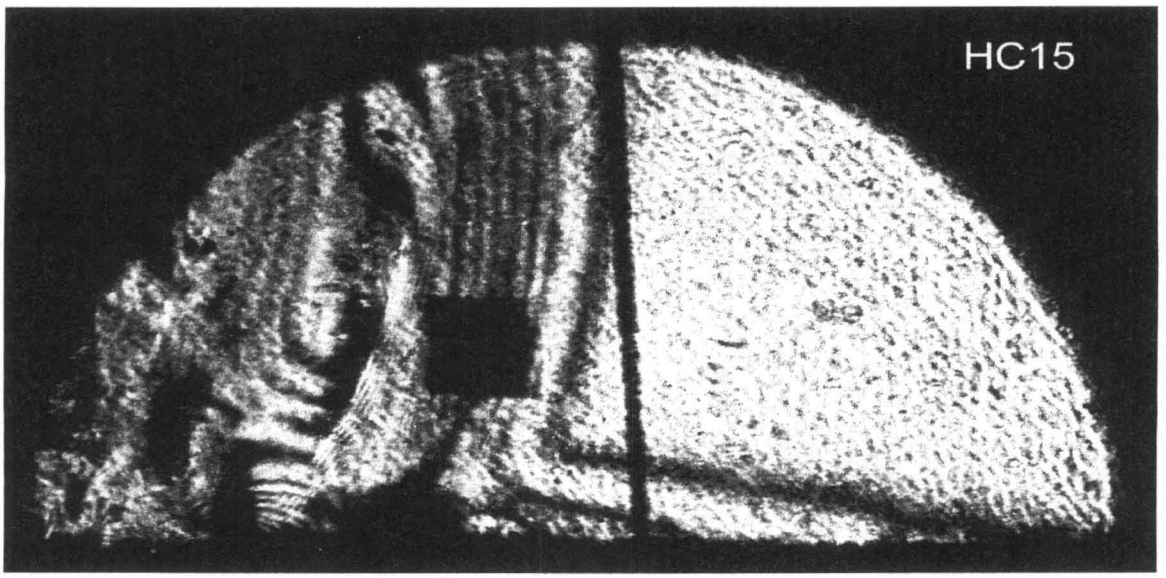

Figure 7

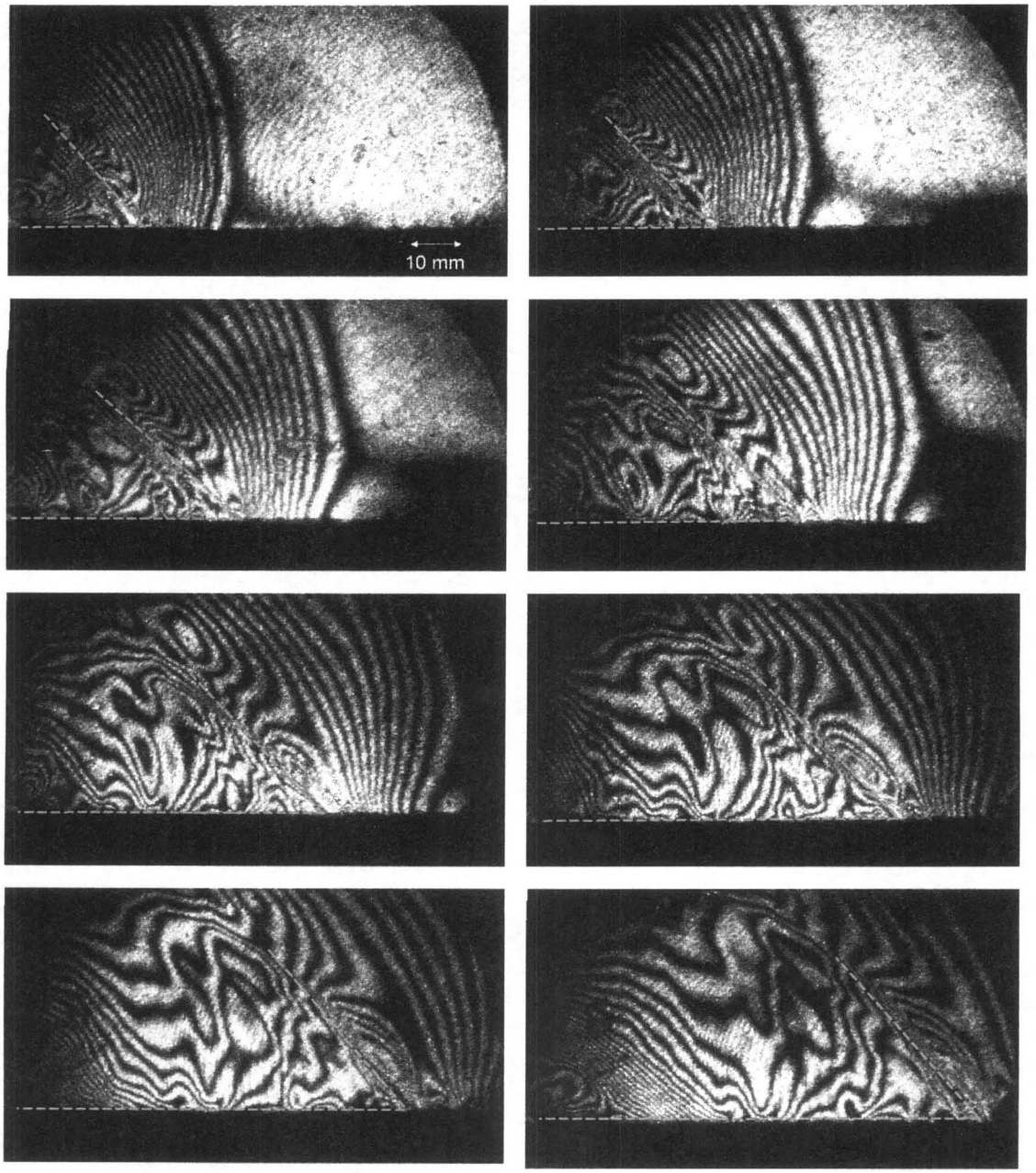

Figure 8

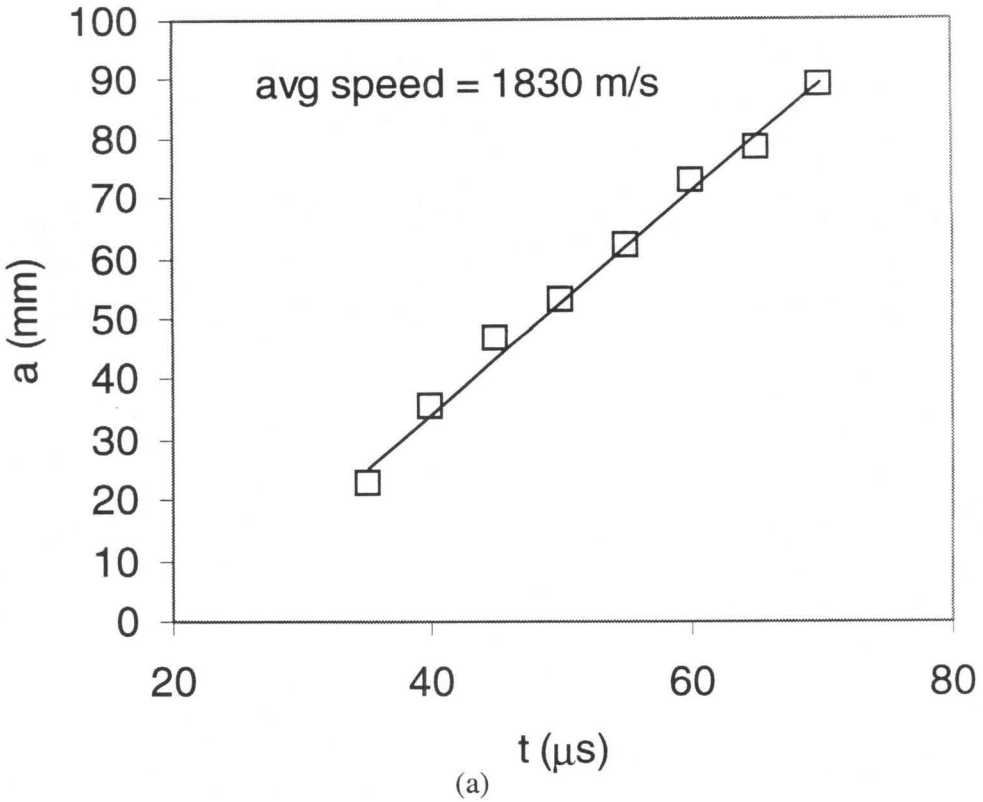
avg speed = 1830 m/s
a (mm)
t (μs)
0
10
20
30
40
50
60
70
80
90
100
20
40
60
80

(a)

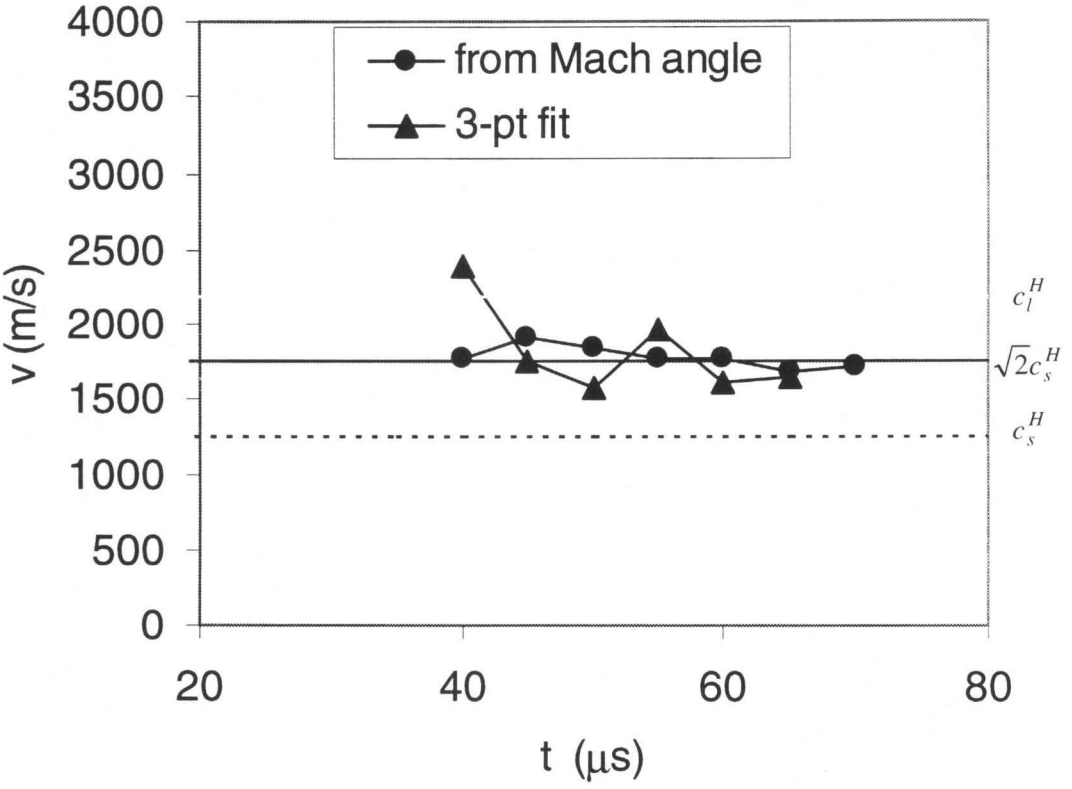
from Mach angle
3-pt fit
v (m/s)
t (μs)
c_l^H
$\sqrt{2}c_s^H$
c_s^H
0
500
1000
1500
2000
2500
3000
3500
4000
20
40
60
80

(b)

Figure 9

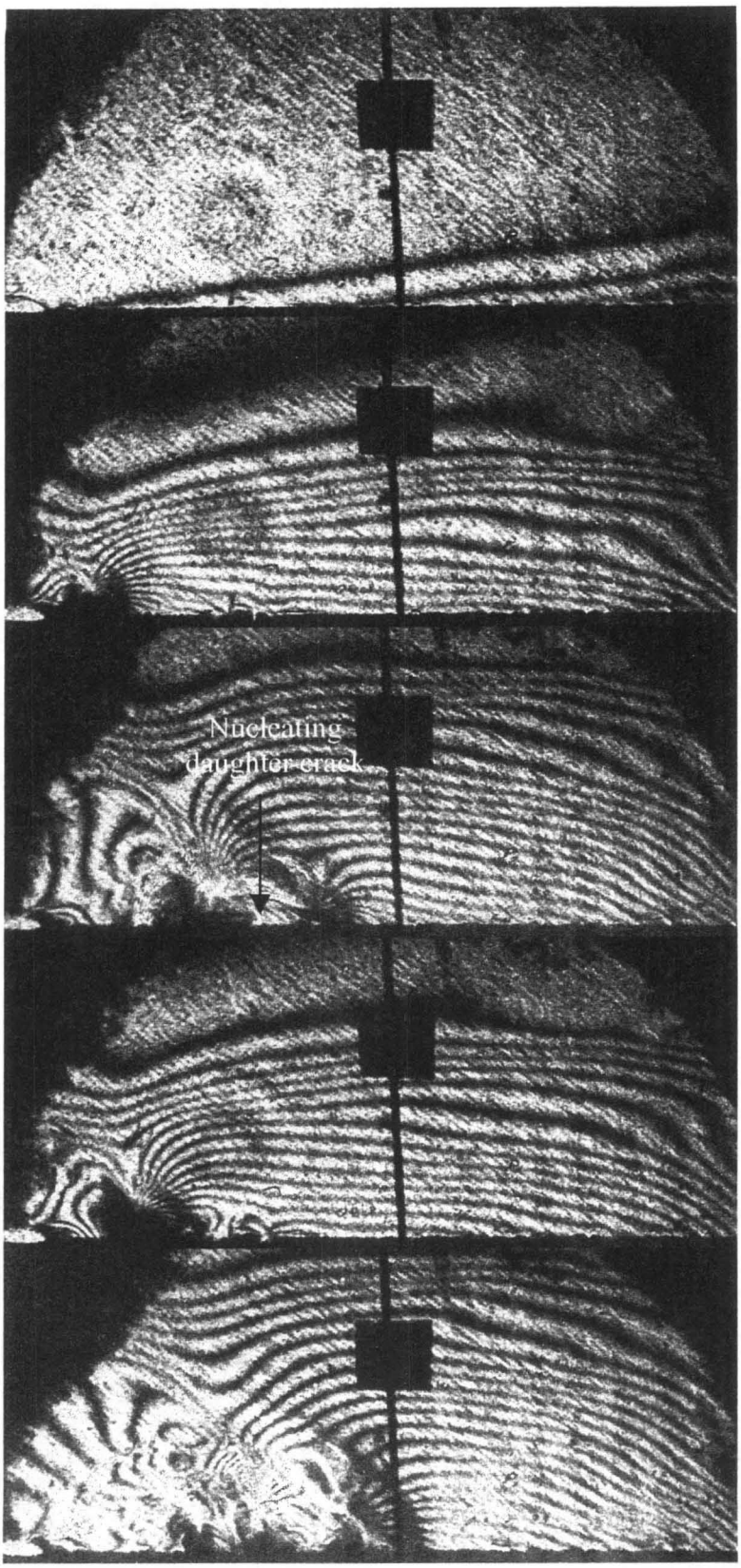

Figure 10

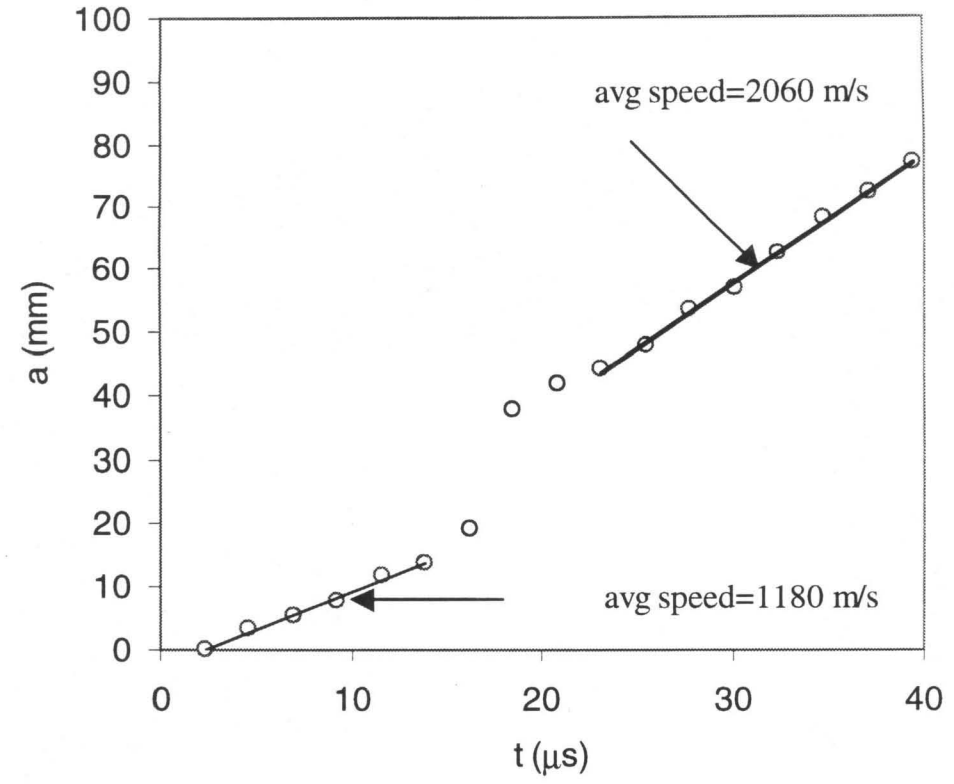
avg speed=2060 m/s
avg speed=1180 m/s
a (mm)
t (μs)
0
10
20
30
40
50
60
70
80
90
100

(a)

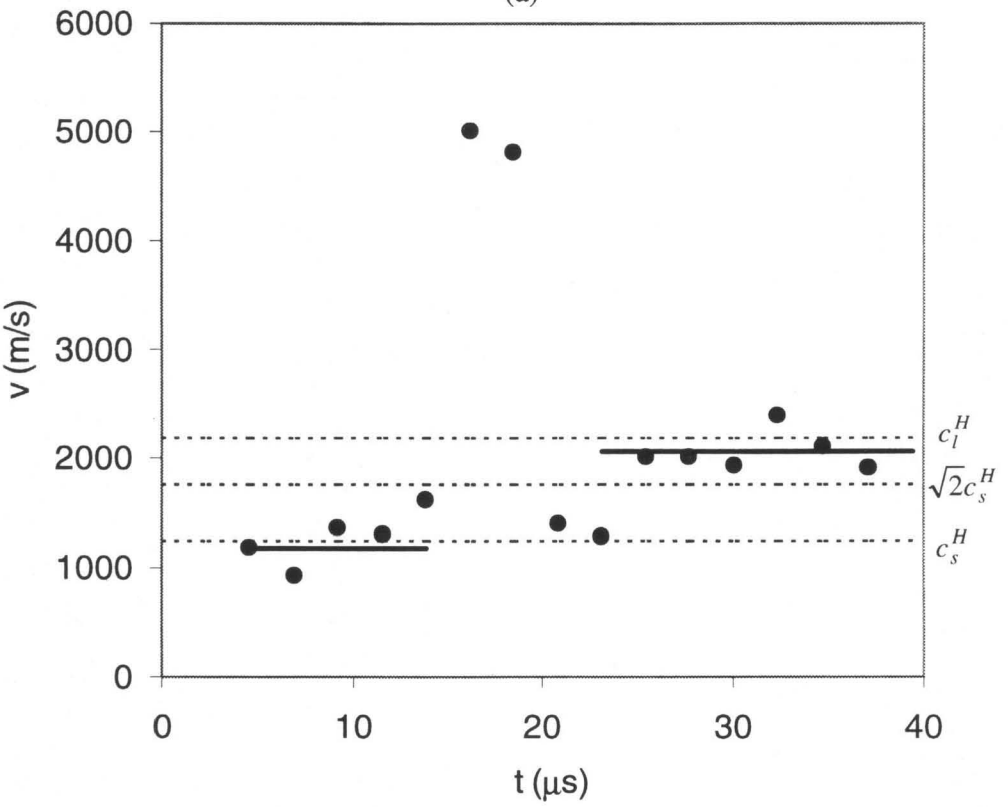
v (m/s)
t (μs)
0
1000
2000
3000
4000
5000
6000
c_l^H
$\sqrt{2}c_s^H$
c_s^H

(b)

Figure 11

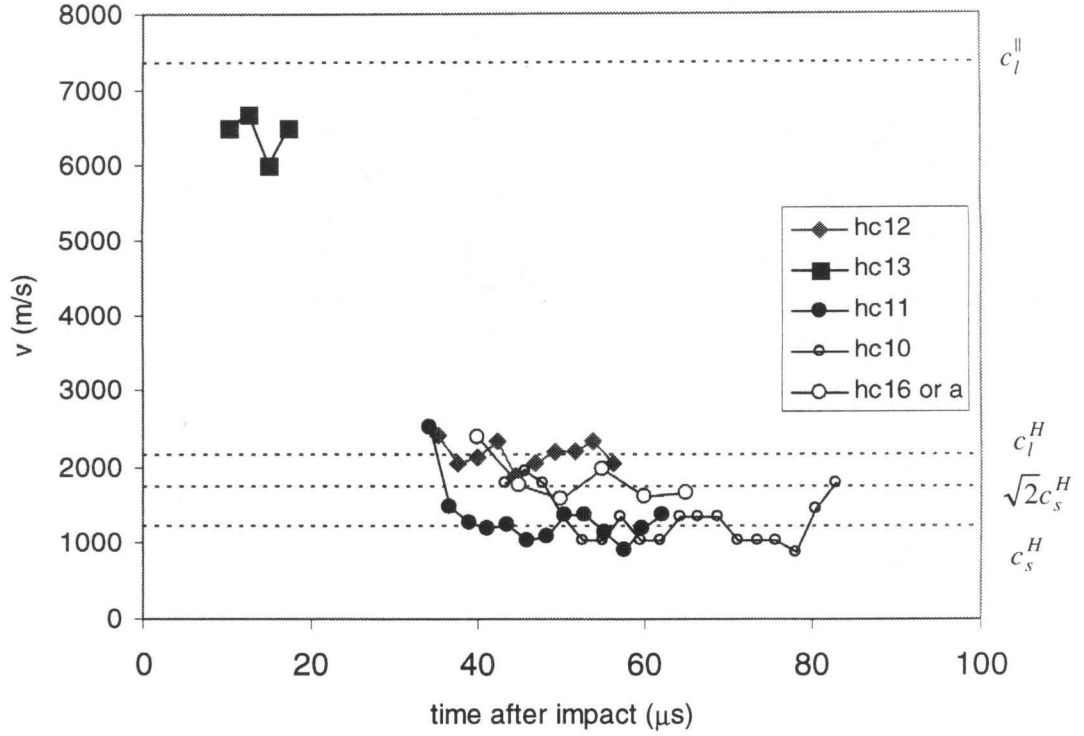
8000
7000
6000
5000
4000
3000
2000
1000
0
v (m/s)
0
20
40
60
80
100
time after impact (μs)
hc12
hc13
hc11
hc10
hc16 or a
$c_l^{\parallel}$
c_l^H
$\sqrt{2}c_s^H$
c_s^H

(a)

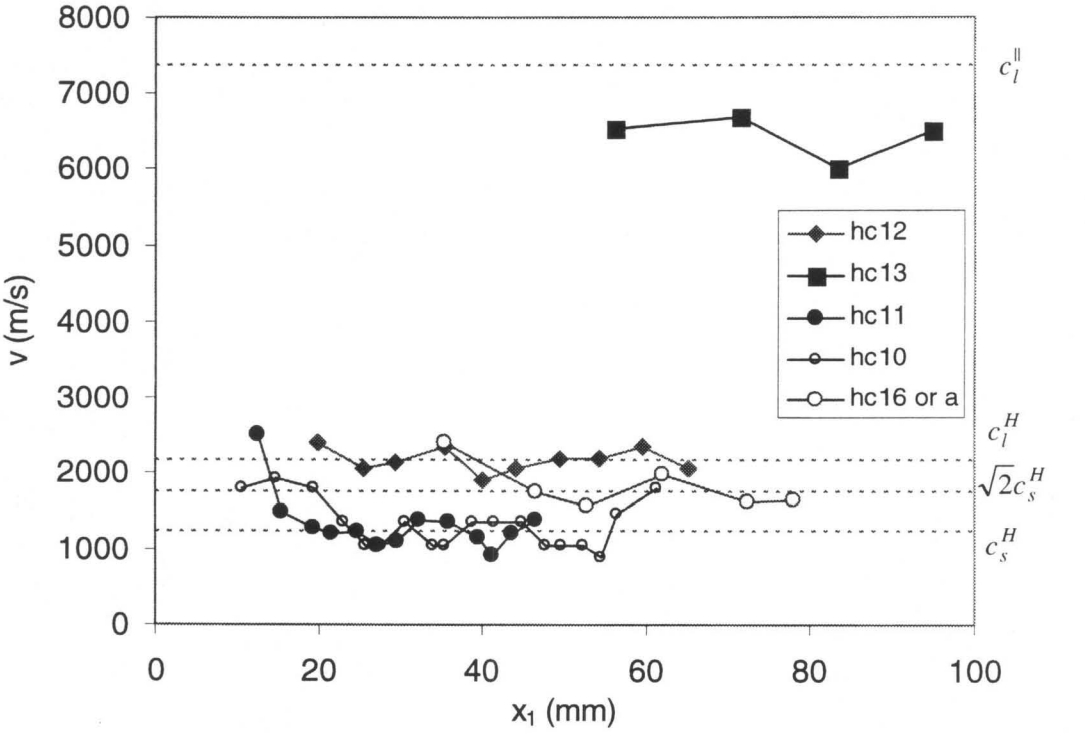
8000
7000
6000
5000
4000
3000
2000
1000
0
v (m/s)
0
20
40
60
80
100
x1 (mm)
hc12
hc13
hc11
hc10
hc16 or a
$c_l^{\parallel}$
c_l^H
$\sqrt{2}c_s^H$
c_s^H

(b)

Figure 12

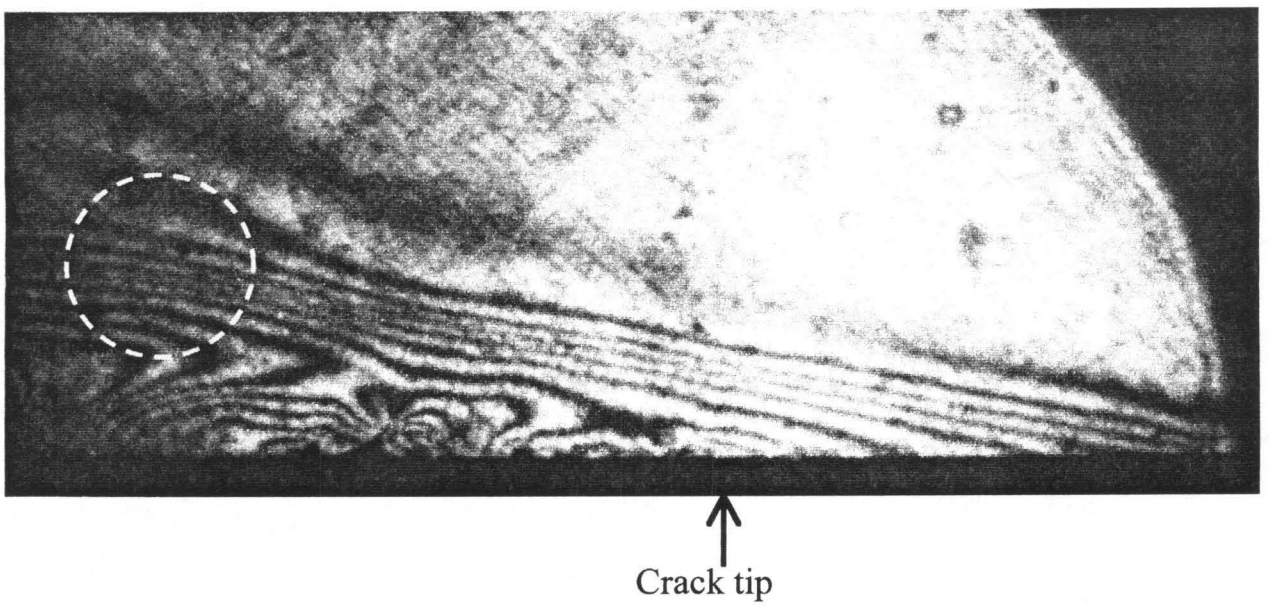

(a)

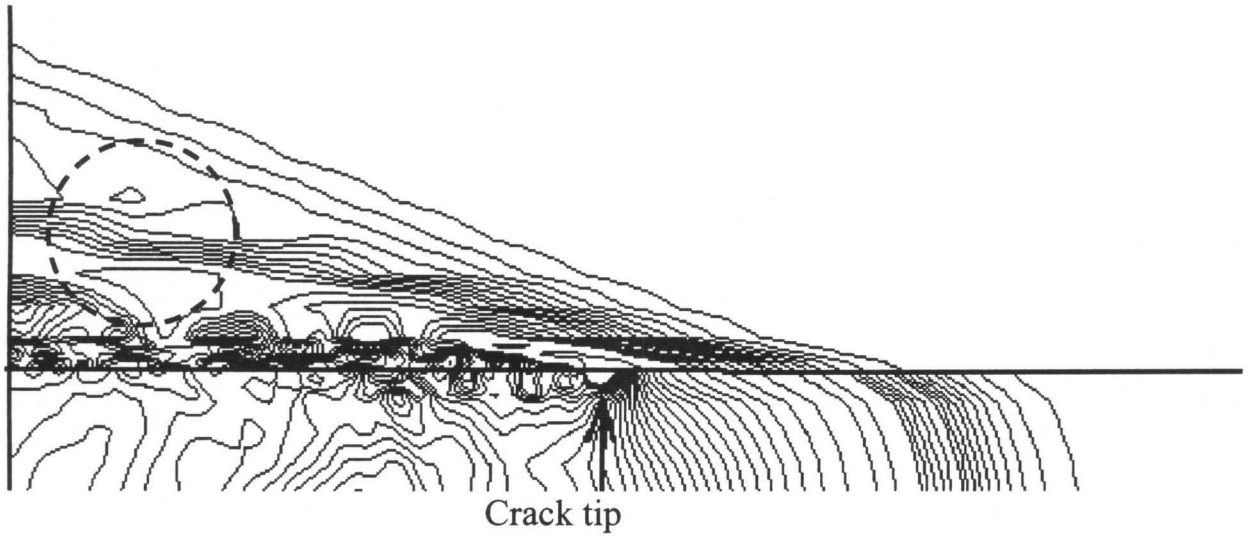

(b)

Figure 13